**The Dissertation Committee for Scott A. Owens Certifies that this is the approved version of the following dissertation:**

# Advanced Analysis of Structured Packing via Computational Fluid Dynamics Simulation

**Committee:**

R. Bruce Eldridge, Co-Supervisor

Roger T. Bonnecaze, Co-Supervisor

Venkat Ganesan

Mitch Loescher

Gary T. Rochelle

Frank Seibert

# Advanced Analysis of Structured Packing via Computational Fluid Dynamics Simulation

**by**

**Scott A. Owens, B.S.E.; M.S.E**

**Dissertation**

Presented to the Faculty of the Graduate School of

The University of Texas at Austin

in Partial Fulfillment

of the Requirements

for the Degree of

**Doctor of Philosophy**

**The University of Texas at Austin**

**December 2010**

# Dedication

This work is dedicated to my family:  immediate, extended, and friends who feel like family.  You've each walked this long road with me and I am immeasurably grateful for the love and support I received along the way.

# Acknowledgements

As with anything worth doing, this project was enabled by the efforts of many intelligent, talented, and dedicated people. I have no doubt this project would have never been completed without the army of people who graciously gave so freely of their time and experience. While no amount of gratitude can ever repay the effort they expended on my behalf, I humbly offer my thanks.

My advisor, Dr. Bruce Eldridge, had the vision to believe this project was a possibility and the eloquence to convince industry to sponsor the work. Luckily for me, he also had the patience to allow me to, often stumblingly, to find my own path as I waded through a sea of simulation and experimental difficulties. Bruce has also served as a mentor for leadership as he guided me through my TA duties while teaching me to accommodate the learning styles of others while assisting them to reach their own goals. His dogged determination and, again, patience were also instrumental in my search for, and eventual securing of, employment.

Dr. Frank Seibert has been a vital resource in this research as well. He is a limitless font of information on distillation, extraction, and the chemical industry as a whole. His knowledge is made all the more valuable by his constant willingness to patiently explain even the most basic concepts to me time and time again. Dr. Seibert

will be my first call if I ever need information about a particular separation or hints on how to pull in monster trout.

When they were not keeping a multi-million dollar research facility running, the SRP staff has kept my project from running off the rails. Susan Tedter, Steve Briggs, Susan Micho, Steve Orwick, and Robert Montgomery have each helped me master the details than are often so deviling. Micah Perry, SRP's resident Renaissance man, has served as safety officer, process expert, photography, whipping boy, brute muscle, and a trusted friend on this project.

A significant portion of the apparatuses used in this project were built from scratch, rebuilt from spare parts, or jury-rigged from who knows what. In this regard, I was constantly amazed and even carried by the skill and determination of the ChE machine shop. Jim and Butch never shied away from even the trickiest builds I brought to them. In fact, they often suggested improvements to the design or materials even when this complicated their own work. Impossible materials, tight tolerances, and short deadlines were all overcome by this duo. They are truly a treasure trove to the department.

As with everything else in this world, the project would never have even begun without underwriting. Thanks go to the Process Science and Technology Center member companies, my sponsoring company Chemical Research and Licensing, and my committee member Mitch Loescher in particular for having faith in the validity of this project and my ability to successfully advance it. The practical advice and context provided along the way also served to keep the project focused making strides in advancements in lieu of perfecting the small details.

The ambitious scope of this project was entirely enabled by the Texas Advanced Computing Center. Having access to one of the world's top ten fastest and most

powerful computing clusters is a game changing resource in and of itself. Being able to speak face to face with those who designed, constructed, and maintain that resource multiplies what can be accomplished with it. Dr. Karl Schulz is to be especially commended. Supercomputing, geometry generation, meshing, CFD simulation, and interpretation of the eventual results were all made possible, in large part, to his guidance. That he could explain these concepts to me so clearly speaks volumes as to the mastery of the subjects.

Sulzer ChemTech is a leader in the design and manufacture of column internals. They were gracious enough to supply all of the packing used in this study while Mark Pilling kindly answered many questions as to its construction, installation, and use. The participation of both was greatly appreciated.

Grad school is one of those experiences that must be lived to be truly understood and I was blessed with many colleagues with which to rejoice and commiserate. To: Grant Offord, Dan Miller, Adam Stephens, David Van Wagener, Katrina Czenkusch, Jorge Plaza, Peter Frailie, Stephanie Freeman, and Fred Closmann Jennie Osburn, and Kate Williams as well as my group mates Ryan Morrison, and Bob – It has been a pleasure to share this experience with you all. I would also be remiss if I did not thank the undergrads who toiled so hard for me: Michael and Kenny, thank and best of luck in the future.

Of course, I am also immeasurably grateful to those friends back home who have kept me grounded throughout this whirlwind. Many thanks to Gina, Sam, Angel, Amanda, Douglas, Tank and Kristen.

Last, but far from least, I must thank my family. The preparation for this achievement began many years ago with your endless love and careful nurturing.

# Advanced Analysis of Structured Packing Using Computational Fluid Dynamics Simulations

Publication No._____

Scott A. Owens, PhD

The University of Texas at Austin, 2010

Supervisors: R. Bruce Eldridge, Roger Bonnecaze

This research explored the use of CFD simulations to study single phase flows through structured packing. Flow rates were chosen to approximate those used in the vapor phase of industrial distillation columns. The results were evaluated against experimental results obtained with the same packing model and packed height. Several novel methods were employed to quickly obtain high validity results.

A high-fidelity, digital copy of an actual packing element was created in seven hours through CT scanning. The meshing strategy employed adaptive, polyhedral meshing algorithms which resulted in high quality volume meshes with 80 percent less mesh elements than would be required with traditional tetrahedral meshing. Meshing and computation were performed on the TACC clusters. This permitted meshing with up to 57 million volume cells in less than 30 hours while simulations employing a realizable k-ε model converged in approximately two days using up to 544 processors.

Nitrogen simulation predictions were found to be, on average, 7 percent below experimental measurements with water simulations showing considerably more error

(~40%). The error is likely attributable a discrepancy between the simulation and experimental geometries. This discrepancy is due to an oversight in sample preparation and not a flaw in the CT scanning process of geometry creation.

The volume of data generated in CFD simulation was found to be very valuable for understanding and benchmarking packing performance. Streamlines and contour plots were used to analyze the variation in performance both locally and throughout the packing stack. Significant variation was observed in flow pattern, velocity distribution, and pressure profiles throughout the column. However, the joint regions were found to be most adverse to column energy efficiency.

# Table of Contents

# List of Tables

# List of Figures

# Chapter 1: Introduction

## SUMMARY OF WORK

This research explored the use of computational fluid dynamics simulations for the purposes of understanding, evaluating and improving structured packing as it relates to the energy efficiency of distillation. A high fidelity computational geometry was generated by importing the results of an X-ray CT scan of a common structured packing. Grid generation was performed automatically using adaptive mesh generation software with user specified minimum and maximum grid spacing as well as cell growth rate. Simulations were conducted with single phase flow imposed axially through the structured packing and against gravity. Flow rates were chosen such that the flow velocities studied would match those commonly observed in the vapor phase of industrial distillation columns. Pressure drop across the packing was monitored during the iterative computations and its rate of change used to judge convergence.

An experimental campaign was carried out to obtain data for the purposes of validating simulation predictions. The experiments utilized an analogous range of flow velocities and a geometry nearly identical to that studied via CFD simulation. Flow rate was manipulated as an independent variable and its variation used to judge the stability of the system. Once the system was judged to be stable, pressure loss across the packing was measured over a set interval of time and then averaged to obtain the steady state pressure drop for that flow rate. The experiments were randomized and repeated two times to obtain three independent measurements of pressure loss at each flow rate. This procedure was carried out first with a single phase vapor flow and then repeated with a single phase liquid flow. Dimensionless pressure loss was compared between the two fluids to evaluate the accuracy of using similarity theory to generalize experimental

results to multiple fluids and phases. Additional experiments were conducted to evaluate the effects of rotating successive packing elements; a common practice in industry. Whole and half elements of the same packing design were used to form two equivalent packed heights and their pressure performance was compared.

The simulation predictions were directly compared to the experimental pressure drop to evaluate the ability of computer simulations to accurately capture the macroscopic effects of turbulence throughout the range of common distillation vapor flow rates. The effect of grid density and turbulence model were also investigated. Furthermore, the wealth of data provided by the simulations allowed a very thorough analysis of flow through structured packing. Streamlines were used to identify regions and features which are likely detrimental to energy efficiency and phase contacting. Velocity and pressure contour plots were used to determine how effectively structured packing distributed the continuous phase and how the observed distribution might affect performance. The simulations also allowed an analysis of the pressure profile along the column axis. This information was used to determine regions within the structured packing which contributed disproportionately to pressure drop.

## MOTIVATION

The oil refining industry revolves around dividing the components of crude oil into a wide range of fuels and chemical feed stocks while the chemical processing industry hinges on the purification of post reaction chemical mixtures. In both cases distillation is the most common unit operation employed to achieve the necessary chemical separation. This fact is borne out by the over 40,000 distillation columns in the United States which combined require more than $5.06 \times 10^{18}$ J ($4.8 \times 10^{15}$ BTU) annually.[1] That translates to over 40 percent of the energy used in refining and continuous chemical production being consumed by distillation columns.[1]

Distillation is so common it is even employed to recover potable water on board spacecraft.[2] This popularity is well deserved. The capital costs of distillation scale with capacity to the 0.6 leading to expansive economies of scale.[2] Columns also boast an expected service lifetime of approximately thirty years. These traits have made distillation the yardstick against which other separation processes are measured.

Due to the extensive use of distillation columns and their long lifespan, even modest improvements in design or operation would result in significant cost savings when propagated throughout the refining and chemical production industries. Most distillation columns are powered by steam produced in boilers burning fossil fuels. Reducing the consumption of these expensive fuels would yield immediate cost savings. These improvements would have the added benefit of curbing $CO_2$ emissions at a time when much attention is being paid to greenhouse gasses.

Distillation performance has long been limited by a lack of comprehensive and robust models of the fluid flow physics which dominate column energy efficiency. The complexity of the two-phase flow field coupled with a dearth of methods to directly observe it have precluded a thorough understanding of the flow phenomena and, in turn, the development of design and operation principles rooted in fluid flow theory. Instead, current distillation design and operation employs a handful of correlative relationships.[3-5] These equations typically rely on thermodynamics data obtained from wetted wall columns to describe the VLE. This information is used to regress lumped terms to describe the combined effect of fluid motion and column internal designs on mass transfer. The use of combined parameters results in a model which is often unable to accurately predict the effect of changes in the chemical systems or flow rates. Consequently, these models do not accurately predict column performance over a wide

operating range.[5-7] Combining the effects of fluid flow and geometry also prevents any attempt to independently optimize these aspects of column design.

Both an inability to accurately represent the intricate geometries and the mathematical complexity of macroscopic flow-field simulations have long been a hurdle to the verification and application of theory based design equations. However, the near petaflop speed, parallel-computing clusters recently developed and deployed at national labs and top universities are increasingly making such simulations possible. These systems enable simultaneous calculations distributed across a large number of processors to solve complex systems of equations on a relatively short time-scale. This increase in available computing power has spurred the development of powerful commercial fluid simulation software. The versatile codes employed in these packages are capable of importing an array of geometry source files, robust mesh generation, multi-phase simulations, and are increasingly accurate over a wide range of flow regimes.

The combination of high performance computing clusters and powerful fluid simulation software has already been employed in the aerospace, automotive, and marine industries to enhance performance, decrease design costs, and accelerate the adoption of new design principles. These tools offer similar opportunity for improving distillation design and performance. Fluid simulation yields a volume and variety of data not available via traditional experimentation. Ready access to both local and macroscopic variables would allow for a rigorous analysis of the flow field in distillation columns. Such an analysis would enable distillation design and operation equations rooted in theory and not tied to experimental data. These equations promise to be more accurate than existing empirical correlations and more robust over the range distillation operation.

## DISTILLATION

Distillation is the separation of chemical species using relative volatility to achieve purification.[3] Under ideal circumstances, vapor and liquid are brought into contact and allowed to come to thermodynamic equilibrium. In industry, this is performed in vertical columns which employ serial vapor-liquid contacting to create high purity product streams. Industrial separations necessarily employ continuous, high throughput applications. This prohibits static contacting and true equilibrium is rarely achieved. A surfeit of contacting media is installed to offset the inefficiencies.

A liquid phase is allowed to drain down the column via gravity while a vapor phase is forced upward resulting in serial, counter-current contacting which enriches the liquid and vapor phases in the high and low boiling components respectively. Figure 1 shows the theoretical construct of such contacting. A liquid ($L_{j-1}$) and vapor ($V_{j-1}$) flow are contacted in region j. Prior to contacting, each fluid is at a different thermodynamic state primarily dictated by temperature, composition, and enthalpy. Maximum mass transfer occurs when the streams leave the region at thermodynamic equilibrium; denoted by the j subscript. Equilibrium is rarely achieved in practice and it is common to assign fractional efficiencies to a contacting region based on percentage of maximum mass transfer achieved. These contacting regions can be employed in a discrete (see Trays below) or continuous manner (see Random Packing and Structured Packing below).

This process is typically run continuously. In this configuration, new material is continually fed to the column (F in figure 2) and can be liquid, vapor, or mixed phase as dictated by the demands of the separation or process train. An internal vapor stream is generated by boiling a portion of the liquid which reaches the base of the column (V in figure 2). That which is not boiled constitutes the bottom product stream (B in figure 2) and is typically removed as a liquid. Similarly, a portion of the vapor phase reaching the

top of the column is condensed and re-introduced as a liquid feed (L in figure 2). The remainder is removed from the column as a product stream (T in figure 2) and can be either liquid or vapor.

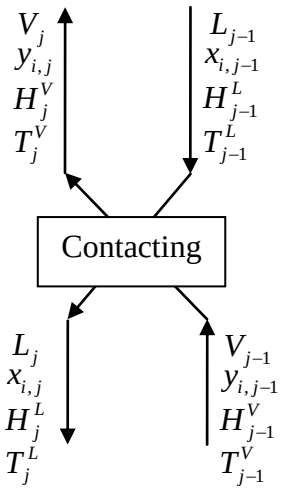


Figure 1: A theoretical depiction of vapor-liquid contacting.

The energy transfer required by distillation occurs in two heat exchangers, the reboiler and condenser (R and C in figure 2). Each heat exchanger must effect a phase change. While the condenser must remove a significant amount of heat, it is typically fed by cooling water, an inexpensive and readily available commodity in most industrial settings. Therefore, the reboiler, which is fed by steam generated from fossil fuel combustion, contributes most significantly to the operating cost of a distillation column.

The degree of purification obtained in a column is a function of the contact area between the liquid and vapor phases whereas the energy efficiency is determined by how much energy is dissipated in the contacting process. The theoretical maximum energy efficiency would be obtained by liquid flowing down the column wall with vapor flowing up the center. This design, known as an open-tube fractionator, would result in negligible mass transfer. Therefore, a wide variety of column internals have been developed to

promote the creation of interfacial area while minimizing wasted energy. As a rule, capital cost and efficiency increase along with increasing column internal complexity. Modern designs increase contact area by subdividing one or both phases and then diverting the flow path or paths so that the streams must pass in close proximity. This process increases interfacial area at the cost of increased pressure loss. More steam must be fed to the reboiler in order to compensate for loss. This increases the pressure at the base of the column thereby forcing the vapor through the column internals. Unfortunately, this also increases the cost of operating the column. For this reason, the internal design employed depends on the trade-off between capital costs, operating costs, and the required product purity. Three designs – trays, random packing, and structured packing – are used extensively in the chemical production and oil refining industries.

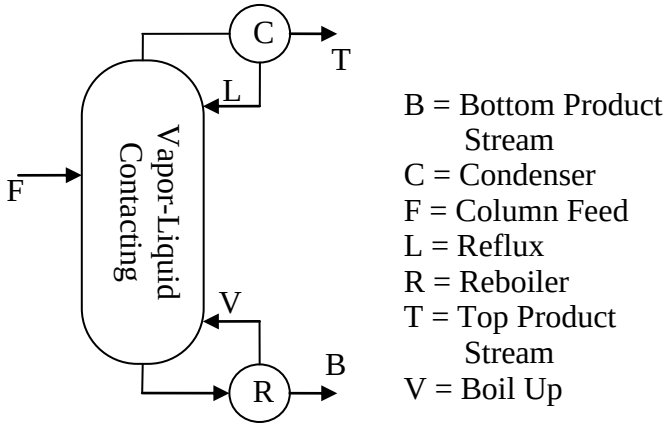


Figure 2: A schematic representation of a distillation column and associated equipment.

**Trays**

Columns employing trays (shown schematically in figure 3 at left) capture the liquid phase at the top of the column and direct it to one side of the column. The liquid

drains down a vertical channel (detail “a” at left in figure 3) on one side of the column. This channel is referred to as the downcomer. The downcomer empties the liquid onto a horizontal plate, also known as a tray. A portion of the tray is perforated (detail “b” in figure 3 at left). These perforations allow the vapor phase (detail “c” in figure 3 at left) to rise from below and bubble through the liquid (detail “d” in figure 3 at left). Some trays utilize floating “valves” which cover the perforations. These valves are forced open by the vapor flow. Because the available area is proportional to the vapor rate, these trays can tolerate a wide range of vapor flows. The surface area of the bubbles constitutes the mass transfer area between the phases. A weir (detail “e” in figure 3 at left) located at the end of the tray can be height adjusted to manipulate the liquid inventory. The liquid accumulates until it flows over the weir into the next downcomer and the process is repeated. The available contact area is the sum of the bubble surface area on all the trays. A picture of an extraction tray (no weir) is show in figure 3 at right.

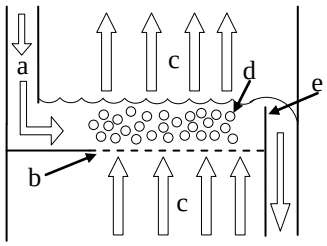


a = Continuous Liquid Phase
b = Bulk Vapor Phase
c = Vapor Bubbles Dispersed in Liquid Phase
d = Perforated Plate to promote contacting
e = Weir

Figure 3: A contacting tray is shown schematically at left with an actual tray shown at right. Photo courtesy of Micah Perry at SRP.

Trays are inexpensive to purchase, easy to modify, and can be tailored a wide variety of liquid and gas rates. However, trays incur a high energy penalty. Each tray imposes a pressure drop roughly equal to the liquid height on the tray. Increasing the liquid height can give increased contacting but necessarily increases the pressure drop. Also, a significant amount of froth is generated when the bubbles break the surface of the liquid. Trays must be spaced well apart to avoid entraining these droplets. This leaves the majority of the volume in a trayed column open and not contributing to area creation.

**Random Packing**

Random packing refers to individual packing elements with characteristic dimensions typically ranging from 25 – 60 mm.[4] Random packings can be made of metal, plastic, or ceramic and are fashioned into complicated geometries meant to distribute and contact the vapor and liquid phases. A common random packing design, 25.4 mm Pall rings, is shown in figure 4 at left. In industry, distillation columns are filled with these individual elements to create a continuous stationary phase as shown at right in figure 4. The liquid phase is introduced from multiple, evenly spaced points above the packing. The vapor phase is introduced below the packing and forced through the void volume. The liquid flows down over the surface of the packing; often transitioning between individual packing pieces by running or dripping through open air. Both the film flow along the surface and the surface of the free falling rivulets and droplets contribute to mass transfer area.

Because columns are filled with random packing, interfacial area is continuously available along the height of the column. This is an improvement over trays which only facilitate mass transfer at discrete heights. Most random packings occupy between 5 and 15% of the column volume.[4] This leaves most of the volume open and the gas flow relatively unimpeded while promoting vapor-liquid contacting. Pressure drop

encountered in random packed columns is typically less than one third that encountered in trayed columns.[2]

Figure 4: Individual random packing elements are shown at left with bulk random packing shown *in situ* at right. Photo courtesy of Micah Perry at SRP.

While the performance of random packing is an improvement upon that of trays in most instances, it is not without its own shortcomings. A significant amount of material is required to fill even 5% of an industrial column and the material must be formed into intricate shapes to promote vapor-liquid contacting and distribution. These traits increase the capital costs associated with random packing. By design, random packing creates many intricate flow paths. The open area of these paths and the available surface area of the packing are proportional to the size of packing selected. Small packings create a large area for the liquid but greatly restrict the vapor phase flow path resulting in a high pressure drop. High vapor phase flow rates also run the risk of fluidizing the free falling liquid drops and flooding the column. Low liquid rates also run the risk of channeling where the vapor and liquid phases pass through the column without contacting each other. For these reasons, random packing enforces a more narrow range of liquid and vapor rates than trays.

**Structured Packing**

Structured packing consists of corrugated sheets of steel, plastic, or ceramic which are oriented vertically and layered so that adjacent sheets have opposite angles of corrugation relative to the vertical. An example of such packing is shown in figure 5. The elements used in industry are typically between 0.254 and 0.305 m in height. When packing is placed in a column, each element is rotated so that the sheets run perpendicular to the element immediately below. The intersection of adjacent packing elements is referred to as the joint. Wiper bands ring each packing element and occlude the area between the sheet edges and the wall. These bands are meant to act as gaskets which prevent vapor and liquid from flowing along the wall and bypassing the packing. Some structured packing uses sheets which have been perforated prior to construction of the packing element. These perforations are meant to allow the vapor to equalize pressure across the sheets.

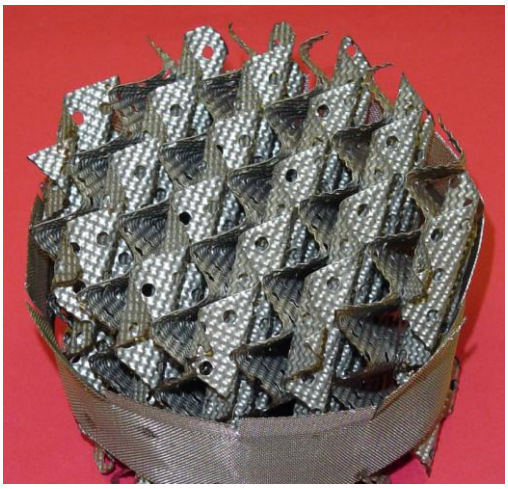

Figure 5: Structured packing (pictured) excels at producing area while imposing minimal energy penalties.

Liquid and vapor are introduced in the same manner as random packing. However, the flow patterns created are much different. The liquid forms a film and flows down the surface of the packing. As liquid flow rate is increased, the film covers a greater percentage of the surface of the packing. Once the packing is entirely wet, increasing the liquid flow rate serves to create a thicker liquid film. In this way the packing area represents a cap on the mass transfer area. Some packing models utilize surface treatments which are purported to create rippling along the surface of the liquid film. This would allow the interfacial area to increase marginally above that of the packing surface. The practice of rotating each successive element results in frequent liquid redistribution. The rotation causes each sheet in a packing element to contact all of the sheets below it. Therefore, the flowing along the surface of one sheet will be distributed amongst all the sheets in the next packing element. In this way a portion of the liquid from each sheet is collected individual sheets in the next packing element. The fluids mix and even out small disparities in concentration.

Structured packings, with volume fractions typically below 5% and sometimes below 2%, present the vapor phase with more open and uniform flow paths than random packing.[4] Each sheet has multiple parallel channels with equal cross sections which direct the vapor up the column while the liquid flows down the periphery of the channel. Just as with the liquid, the vapor is divided by the joints and redistributed as it passes through the next packing element.

Structured packing is generally considered superior to both trays and random packing. Like random packing, structured packings create area throughout the height of the column. The high void fraction and uniform vapor flow paths result in much lower pressure drop while the redistribution of liquid and vapor allow for good contacting throughout a much wider range of flow rates. In fact, structured packing typically gives a

pressure drop per efficiency number an order of magnitude lower than comparable trayed towers.[2] Initial costs are among the few shortcomings of structured packing. The use of durable materials, application of surface treatments, and the need to pin the sheets together all add to the purchase price. Installing structured packing often requires teams to perform a confined space entry into distillation columns and place each level of packing by hand. For these reasons, structured packing is often chosen in high volume processes, difficult separations, or those which recover especially valuable components. The combination of low pressure drop, high capacity, and high efficiency mean the operational savings will quickly repay the high initial costs.[4]

## COMPUTATIONAL FLUID DYNAMICS (CFD)

### Industrial Applications

Computational Fluid Dynamics (CFD) simulations allow engineers to conduct thorough performance analyses of potential designs before the first physical prototype is ever fabricated. This process is referred to as Computer Aided Design and has become instrumental in many fields. It is now commonplace in the automotive industry to evaluate the drag contribution of individual components. The shape and placement of fairing, spoilers, and even side-view mirrors can be optimized independently or assembled into a hollow auto body to gauge the fuel efficiency of theoretical cars. Drag plays a similar, if magnified, role in the marine industry. The high drag encountered by boat hulls means that small improvements can drastically reduce fuel costs. This is why designs for everything from pleasure craft to super tankers are subject to intense scrutiny in CFD. Perhaps no field has benefited as greatly from CFD as the aerospace industry. Obviously, the ability to model the tradeoff between lift and drag is of critical importance in airframe design. However, aircraft design has also benefited from the ability to

estimate the stresses experienced during flight. This allows designs which are fully vetted in all flight conditions and reduces the need for excessive safety factors. Similar advantages in design and operational improvements stand to be realized from the application of CFD in the chemical and oil industries.

Reactors, heat exchangers, separators and many other processes operate at the mercy of fluid flow phenomena. This has made the study of moving fluids, or fluid dynamics, an integral part of chemical engineering. Fluid dynamics can be divided into the study of laminar and turbulent flows. Most flows encountered in industrial processes exhibit turbulent behaviour.[8, 9] Turbulent flows are characterized by increases in pressure drop being roughly squared that of the velocity increases as well as the presence of cross current eddies.[10] Each eddy in the flow possesses a set amount of mechanical energy. The potential of the bulk fluid flow provides energy for the largest eddies. These eddies break into smaller eddies which in turn given smaller eddies still. This process occurs without appreciable energy loss to heat.[10] Heat is only generated when the smallest eddies are destroyed by viscous dissipation.[10]

The process of eddy creation, energy transfer between eddies, and eddy destruction is chaotic. This makes directly solving for the flow field prohibitively difficult. Instead, researchers have turned to the use of numerical approximation and powerful parallel computing clusters to study turbulent flows. This procedure is commonly referred to as Computational Fluid Dynamics (CFD). The use of numerical methods permits the continuous governing equations to be approximately calculated at predetermined points in space while use of many thousands of processors allows for the simultaneous calculation of flow throughout the geometry and expedient convergence of iterative solutions. In these ways, CFD allows the study complicated flows in a far more efficient and effective manner than can be achieved using traditional experimentation.

**Turbulence Modeling**

Fluid dynamics are described by the Navier-Stokes and continuity equations. For a viscous, incompressible fluid with constant physical properties these equations are given by

$$\frac{\partial u_i}{\partial t} + u_j \frac{\partial u_i}{\partial x_j} = -\frac{\partial p}{\partial x_i} + \nu \nabla^2 u_i \qquad \text{Equation 1}$$

$$\text{and } \frac{\partial u_i}{\partial x_i} = 0; \qquad \text{Equation 2}$$

where $u_i$ is the velocity vector, $p$ is the modified pressure, and $\nu$ is the kinematic viscosity.[9] Because the turbulent eddies are much larger than the mean free path of the fluid molecules, the Navier-Stokes and continuity equations are applicable to turbulent flows.[8] However, the chaotic nature of eddy creation and dissipation bars direct calculation of the values in equation 1 and equation 2. As noted in McCabe *et al.*, local velocities must sum to yield the bulk flow which causes the fluctuating components drop out when averaged over a time period of at least a few seconds.[10] This allows the flow values to be decomposed into mean (denoted by an overbar) and fluctuating parts (denoted by a prime). For the velocity terms, this would be written as $u_i = \bar{u} + u'$.[8-10] This can be combined with the assumptions outlined in Speziale to yield the Reynolds Averaged Navier-Stokes (RANS) equation

$$\frac{\partial \bar{u}_i}{\partial t} + \bar{u}_j \frac{\partial \bar{u}_i}{\partial x_j} = -\frac{\partial \bar{p}}{\partial x_i} + \nu \nabla^2 \bar{u}_i - \frac{\partial \tau_{ij}}{\partial x_i}, \qquad \text{Equation 3}$$

$$\text{where } \tau_{ij} = \bar{u}_i' \bar{u}_j', \qquad \text{Equation 4}$$

and the mean continuity equation

$$\frac{\partial u_i}{\partial x_i} = 0 .^{9} \qquad \text{Equation 5}$$

Equation 4 is referred to as the Reynolds-stress tensor and contains six unknown flow variables.[9] These added terms prevent equation 3, equation 4, and equation 5 from forming a closed system. The need to form a closed system is broadly referred to as the "closure problem" and represents one of the primary hurdles of turbulence modeling.[8] The preferred closure method is to relate the Reynolds-stress terms to bulk fluid properties. In practice, the concept of a dynamic turbulence viscosity is most commonly used.[11]

The Linear Eddy models utilizes the concept of a dynamic turbulent viscosity to relate the Reynolds-stress terms to the average velocity gradient.[11] Under this model, closure requires defining both a turbulent length and time scale. Many methods exist for this purpose with the main difference being the number of transport equations used to define these variables. As a general rule, two equation models are considered a satisfying compromise between accuracy and ease of calculation.[9, 11]

The k-ε model is the most popular two-equation closure method and is often used as a standard by which new or improved models are measured.[9, 11, 12] In this model, independent equations are modeled to obtain the turbulent kinetic energy (k) and the rate of turbulent energy dissipation (ε).[9, 11-13] These two terms and their ratio are then used as the basis for calculating other parameters. Several other two-equation models, such as the k-ω or k-l, exist. Each model possesses its own strengths and weaknesses based on

the characteristics of the specific flow and geometry to be modeled.[12] For this reason it is often advised to test the solution's sensitivity to a number of turbulence models.

The underlying assumptions to the Linear Eddy model breakdown in the event of complex strain fields.[11] This situation may arise due to swirling flows or the present of body forces such as buoyancy or those arising from excessive geometric complexity.[11] In these instances, the more complicated Reynolds-Stress Model (RSM) or Second Moment Closure is often employed. This model forgoes the use of turbulent viscosity to relate parameters and instead utilizes six modeled transport equations to directly calculate the Reynolds-Stress tensor as well as an equation to calculate ε which serves as a basis for the turbulent length scale. This model has been shown to be very accurate under even the most complicated flows. However, that accuracy comes at the cost of computational complexity. The time required to solve the RSM is often many times that of the simpler two equation models. Therefore the RSM is typically applied only when other models fail to provide a satisfactory accuracy.

Turbulence modeling has received a tremendous amount of attention in recent years due, in part, to the prevalence of powerful computers capable of quickly performing the complicated calculations. This has given rise to an abundance of distinct turbulence models as well as many customized or improved versions of the traditional models including those previously mentioned. The discussion presented above is not meant to educate the reader but instead provide a brief summary of terminology and context for the work described below. Interested readers are referred to "Turbulence Modeling for CFD" by David Wilcox for a more informative and rigorous discussion of the topic.[14]

**Discrete Solutions**

The governing equations describe fluid behaviors that are continuous in both time and space and consequently their solutions require detailed information about the flow

itself. However, researchers often need to investigate flows about which little information is available. The lack of *a priori* knowledge precludes obtaining a rigorous solution in these instances. For this reason the governing equations have been adapted to allow approximate solutions to be obtained from sparse data.

It is infeasible and unnecessary to exactly solve all of the equations used in turbulence models continuously throughout complicated industrial flows. It is often sufficient to calculate the approximate change in flow across manageable subdivisions. This has led to the use of numerical methods to modify the governing equations so that they can be applied to discrete volumes. As an example consider the real function *f(x)*. Given the value at a point ($x_j$), the function's behavior near that point ($x = x_{j+1}$) can be described by a Taylor Series expansion about x:

$$f\left(x_{j+1}\right) = f\left(x_j\right) + \frac{f'\left(x_j\right)}{1!}\left(x_{j+1} - x_j\right) + \ldots .^{15} \qquad \text{Equation 6}$$

Truncating after the second term and solving for $f'\left(x_j\right)$ yields

$$f'\left(x_j\right) = \frac{f\left(x_{j+1}\right) - f\left(x_j\right)}{\left(x_{j+1} - x_j\right)}, \qquad \text{Equation 7}$$

which gives a finite difference approximation to the first derivative of *f* in terms of the function values. This would be known as a second order, forward difference scheme for calculating the first derivative. These schemes can be made much more accurate, and complex, by truncating at much higher terms and combining expansions for many points within the region of interest.

The use of finite difference schemes imparts many advantages to fluid dynamics modeling. The greatest advantage is the ability to iterate towards an accurate representation of the flow field. The governing equations enforce a relationship between velocity, pressure, and fluid properties. This allows trial solutions to the velocity field to be solved using a trial-and-error methodology. A velocity distribution is assumed and used to calculate the derivative terms. These terms are in turn used in the governing equations to calculate an improved solution to the flow field. This procedure is repeated until the velocity terms approach an asymptotic solution.

The selection of specific points within the geometry volume, called gridding or meshing, serves multiple purposes. Iterating to arrive at a solution requires the same points be used to advance the solution. Perhaps more important is the effect the selection of these points has on the required computing memory and the final solution accuracy. Because the numerical methods employed are meant to represent continuous phenomena, selecting points more spaced closely together will typically result in a more realistic portrayal of the phenomena being studied and yield a more accurate final solution. Example meshes are shown in figure 6.

Unfortunately, closely spaced points also increase the memory needed to store iterations and the overall number of calculations needed per iteration. The conflicting needs of accuracy and expeditious simulation have lead to the use of non-uniform grid dimensions. A highly refined mesh is used near geometry features which are likely to create sharp gradients in the flow field. The mesh points are spaced further apart as the mesh grows into areas where the flow is expected to change more gradually.

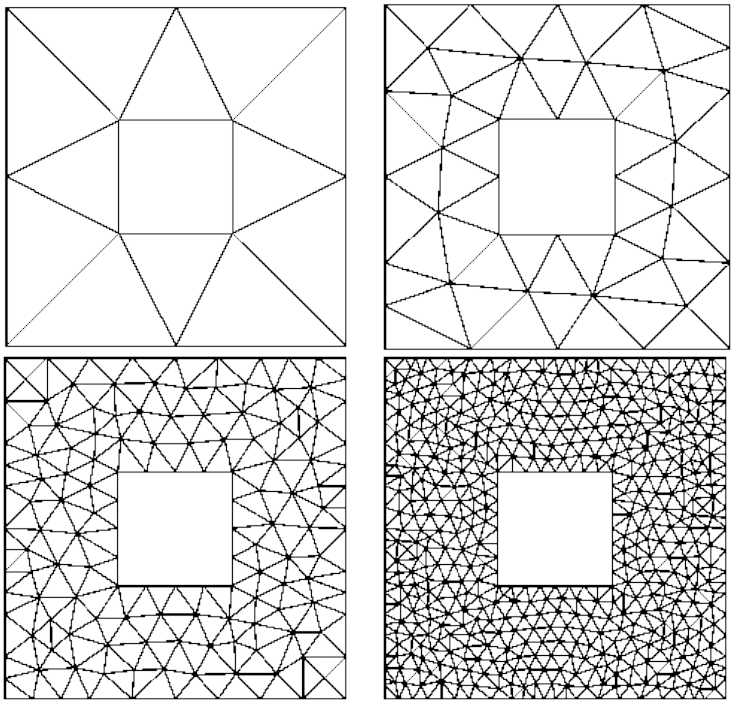

Figure 6: Successively finer triangular meshes shown on a two dimensional square with a square hole in the center.

Differencing schemes and meshing are similar to turbulence models in that many different methods have been developed and the success of each method is highly dependent on the specific geometry and flow being studied. The texts by Durran and by Thompson *et al.* are recommended for further discussion of these topics.[16, 17]

**High Performance Computing (HPC)**

The advent of ubiquitous parallel computing has greatly increased the capabilities of fluid researchers. Modern fluid simulations employ closure models which require many equations be solved in order to calculate the flow field at a given point. These equations must be solved every iteration at each point throughout the geometry. High performance computing clusters utilize a large number of processing nodes to perform the requisite calculations in parallel which permits faster iteration.

There is, however, a limitation to the performance gain from additional processors.[12] As the number of nodes increase each node calculates a smaller portion of the total flow field. This means the nodes must request information about adjacent flow characteristics from other processors. As the number of nodes increases so does the lag time associated with node-to-node communication.[12] This is defined as scaling and the performance of adding nodes is typically evaluated as the ratio of increased computational speed to increase in compute nodes.

# Chapter 2: Literature Review

## EXPERIMENTAL ANALYSES OF DISTILLATION

The ability to accurately design distillation columns and predict existing column performance is of paramount importance to the chemical processing and oil refining industries. Two models have come into common usage for this purpose: the SRP model (a.k.a. Rocha-Bravo-Fair) and the Delft model (a.k.a. Olujic).

The SRP model represents packing as a series of parallel, inclined wetted wall columns.[18] Packing specific parameters are expressed as the characteristic cross-section and a diameter equal to the side length of a corrugation channel. The formulation does not explicitly account for the effects of proprietary designs or surface treatment; however, these can be accounted for via regression of the equation coefficients from experimental data

The Delft model approximates packing as a series of saw tooth flow channels.[18] The hydraulic diameter is set equal to the width of intersecting corrugation channels. This model assumes total wetting and calculates holdup by combining the packing area and an average liquid film thickness. This model has been shown to consistently predict lower holdup than the SRP model which employs an implicit equation for holdup using film thickness and contact angle.

Green *et al.* employed X-ray computed tomography to image an operating air-water contactor.[19] The scanning system consisted of a 6 MeV source paired with a 1 m linear array of 1,024 scintillation detectors with 1.5 mm apertures. Scans were taken at both 2 and 6 MeV. The acrylic contacting column had an ID of 0.146 m and was packed with a 0.406 m height of stainless Mellapak structured packing. Both half and whole elements were imaged. Liquid rates ranging from 5.4 to 48.9 $m^3/(m^2\ h)$ were studied in

combination with a vapor F-factors range of 0.33 - 1.83 $Pa^{0.5}$. The authors studied liquid hold up and demonstrated that X-ray CT could be used to independently obtain this data and could also be used to validate commonly used models. CT images were also able to obtain specific details about liquid distribution. In particular, liquid hold up was found to vary as a function of column height. The hold-up was noticeable higher immediately above the packing joints. This type of information cannot be obtained using the traditional method for determining liquid hold up and available area. However, the non-uniform performance identified in this work is a logical starting place for optimizing the performance of existing packing designs.

In 2008, Tsai *et al.* studied the effects of surface tension and specific packing area ($a_p$) on effective area.[6] Effective areas ($a_e$) were measured in Mellapak 250Y ($a_p$ = 250 $m^2/m^3$) and 500Y ($a_p$ = 500 $m^2/m^3$) using low (35 mN/m) and high (72 mN/m) surface tensions liquids across a range of flow rates. The measured areas were normalized by the specific packing area and reported as fractional areas ($a_f=a_e/a_p$). Mellapak 250Y showed fractional areas near unity (complete wetting) for both high and low surface tension liquids at all flow rates. Conversely, Mellapak 500Y did not display complete wetting in either instance. Under high surface tension liquid flow, fractional areas increased from 0.35 to 0.6 with increasing liquid load. The same experiment with low surface tension liquid gave fractional areas from 0.5 to 0.8. The differing behavior in response to surface tension was thought to be a factor of liquid pooling and bridging in the narrower crimp of Mellapak 500Y.

The authors also compared the fractional areas observed in Mellapak 250Y with those predicted by popular models. The results of that comparison are shown in figure 7 and figure 8. The Olujic model, which most accurately predicted the numerical values of fractional areas, failed to predict the area creation observed with increasing liquid loads.

Interestingly the Bravo-Fair model, which most closely approximated area response to liquid load, was developed for random packing.[20] No model accurately predicted both the observed values and the effect of liquid load on area creation. This underscored the need for a robust model which was developed by Tsai *et al.*[5]

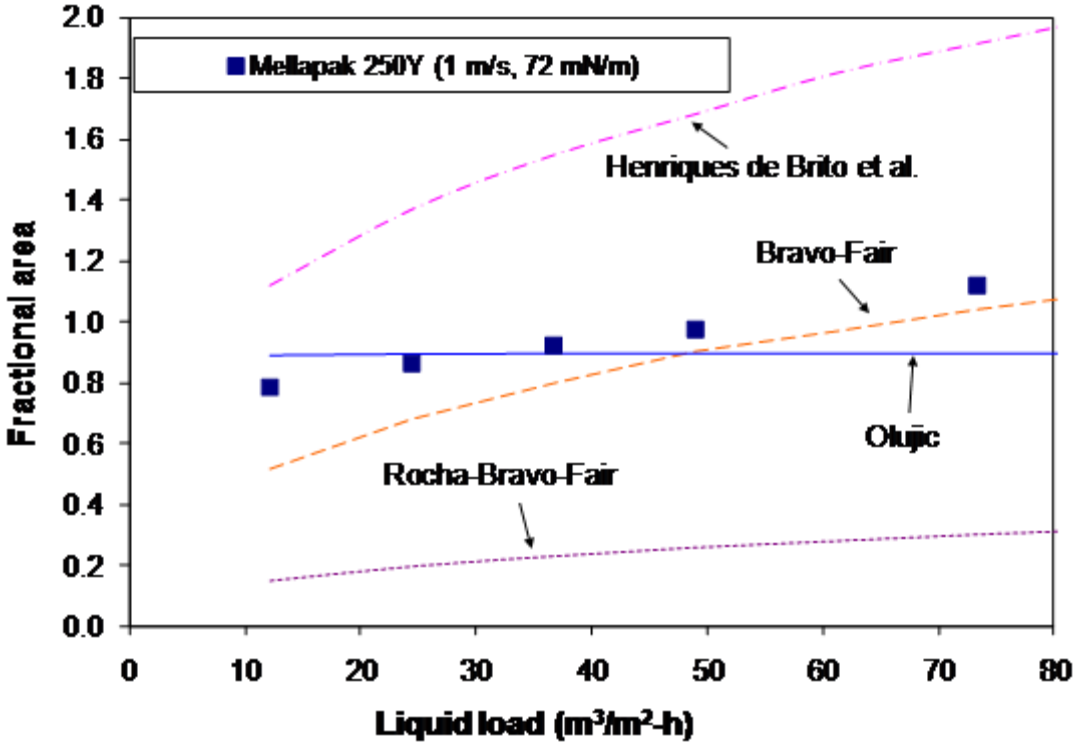


Figure 7: Comparison of Mellapak 250Y ($a_p$ = 250 $m^2/m^3$) baseline data with existing models at air velocity of 1 m/s.[6]

X-ray radiography was employed by Owens *et al.* to study the continuous phase flow field through structured packing.[21] Neutrally buoyant, X-ray opaque particles were entrained in water flowing through three half elements of Mellapak N250Y in a 0.146 m ID column. The flow rates were chosen such that the Reynolds numbers studied ($N_{Re, Sup}$ = 5,000 – 22,000) were equal to the range typically found in the vapor phase of industrial distillation columns. X-ray scans were performed at a 30 Hz frequency for 3 seconds.

The authors recorded both instantaneous velocities, recorded in each frame, and macroscopic streamlines which were created by summing sequential frames. The local velocities were show to vary as much as four times higher than the calculated superficial velocities. This was likely caused by the flow disruption recorded near the packing joints. While flow within the mid packing region was predominately smooth and uniform, flow at the joint exhibited recirculation and stagnation zones. This work further confirms that structured packing performance is not uniform throughout the packing but instead exhibits a high degree of variation. The chaotic and disruptive flow observed the joint was theorized to be a limiting factor in terms of column throughput and energy efficiency.

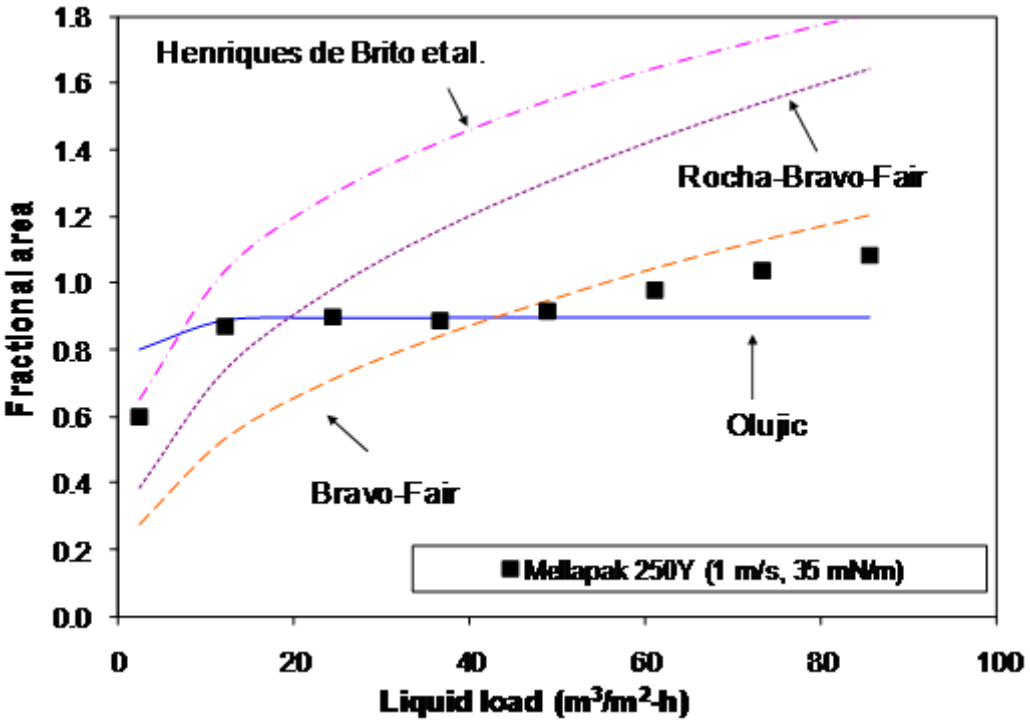


Figure 8: Comparison of Mellapak 250Y ($a_p$ = 250 $m^2/m^3$) low surface tension data with existing models at air velocity of 1 m/s.[6]

## CFD STUDIES OF PACKED COLUMNS

This project is mean serve as a first step in analyzing and documenting the parameters which affect the accuracy of CFD simulations of bulk phase flow through realistic representations of structured packing. The long term goal of this research is to facilitate direct simulation of the physics occurring in two-phase flow through structured packing. Up to this point, simplifications have been required to model structured packing and no studies have attempted to model the transition between adjacent packing elements. This is undoubtedly due to the gargantuan computational requirements required for accurate gridding of large volumes of structured packing. Moreover, the computation time can be prohibitive without the aid of massively parallel computing facilities. The University of Texas facilities present a unique opportunity for cutting edge CFD simulation. UT is home to both a world class X-ray CT facility and one of the world's largest and fastest high performance computing clusters. These resources enable CFD research on a scale and time frame which cannot be achieved at other institutions.

The earliest efforts at 3D CFD simulation of structured packing sought to reduce the computational needs of simulation by modeling constitutive volume elements of structured packing separately.[22-27] Petre *et al.* modeled single phase vapor flow through four representative volumes in three different packing designs.[22] This research referred to the volume elements as Representative Elementary Units (REU). The REUs are shown in figure 9. Simulations were carried out at Reynolds numbers ranging from creeping flow to fully turbulent regimes. Pressure losses for each REU were obtained directly from CFD simulation. In order to obtain macro-scale pressure drop, the researchers were required to empirically determine the relative number of REU's in each type of packing as well as the manner in which adjacent REU's interacted. With this information, the researcher's derived expressions which predicted the macro-scale dry

pressure drop based on the pressure drop of individual REU's. The CFD predictions proved to be more accurate than the models published by: Meier et al., Rocha et al., Brunnazi and Paglianti, and Olujic.[28-32]

The REU method of simulating single-phase flow in structured packing was extended by Larachi *et al.* to evaluate the energy efficiency gains of the recent "high efficiency" packing designs.[23] The researchers simulated the pressure drop of REU's characteristic of both Montz B1-250.45 and the higher capacity version, Montz B1-250.45+B1V. The higher efficiency design is modified so that the channel corrugations angles become vertical at packing-packing interfaces. The simulations showed the energy efficiency of the vertical channel REU's to be 30% higher than REU's which transitioned between 45 degree channels. However, the simulations also showed that this was a minor contribution to the macro-scale pressure loss.

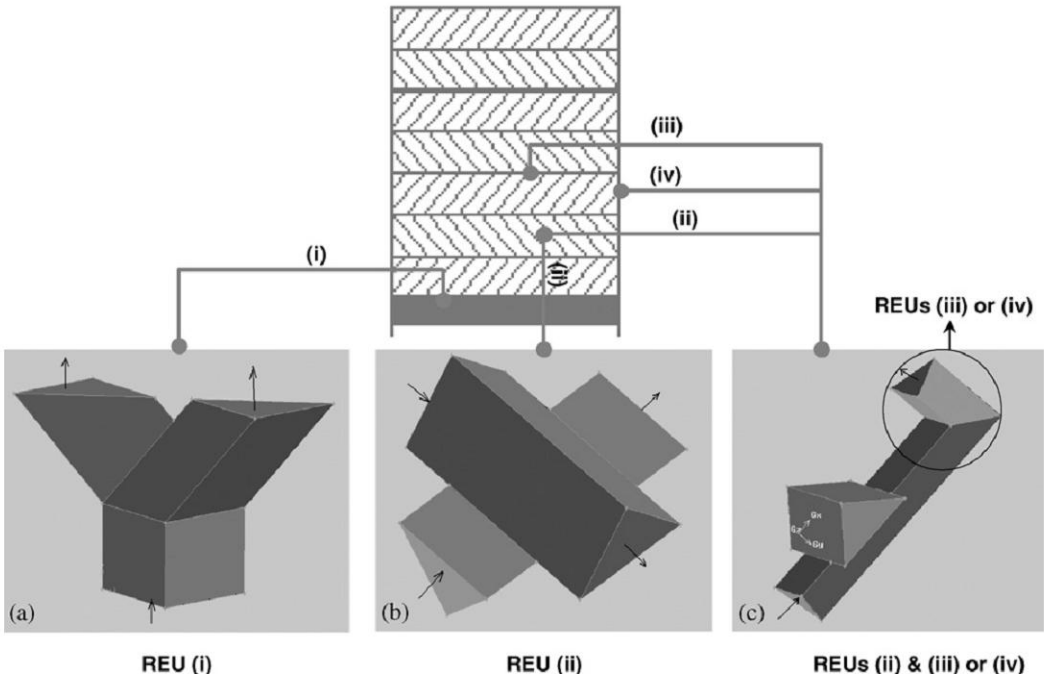


Figure 9 - The REU's employed by Petre *et al.*[22]

Ataki *et al.* performed liquid only CFD simulations using a representative geometry to determine the effect of liquid viscosity on wetted area [24]. The research focused on Rombopak 4M which is composed of strips of metal overlaying each other to form a repeating pattern of X shaped intersections. Ataki *et al.* used a single X section as a geometry. Liquid was introduced at the tip of each upper leg and a pressure outlet boundary condition on all sides of the lower legs. Any volume not filled with flowing liquid was filled with static gas. FLUENT's Volume of Fluid (VOF) package was used to simulate the liquid flow and track the vapor-liquid interface. The researchers compared the CFD predicted effects of liquid velocity and viscosity to those predicted by correlation and observed in experimentation. The CFD predictions were shown to be more accurate over a wider range of fluid properties and flow rates than the Billet-Schultes, Shi-Mersmann, SRP, Delft, and Onda models.

Raynal *et al.* employed elementary geometry simulations to study irrigated pressure drop.[25] This research considered three geometries. The first was a three dimensional representation of two intersecting channels. This geometry was shown to over-estimate dry pressure drop. The researchers concluded the geometry was too simplistic for quantitative measurements but theorized similar packing designs could be evaluated on a qualitative basis by simulating only those REU's which differed. A second geometry consisting of the space between two sheets of packing 200 mm wide by 100 mm tall was used to calculate specific pressure drop. Pressure measurements were made at two heights in the interior (23 mm and 78.55 mm) of the packing. This eliminated end effects which contributed to the inaccuracy of the first geometry. The third geometry was a two-dimensional cross section of the second geometry. The cross section was taken perpendicular to the packing sheets. The VOF package was used to calculate liquid thickness under two phase co-current flow. This thickness was then

extrapolated to a volumetric liquid hold up. The results were compared to liquid hold up measured by gamma ray tomography. The two-dimensional simulation was found to under predict hold up by approximately 20%. However, the simulation more accurately predicted liquid loading than did calculation of hold up by transport phenomena theory.

Szukzeqska *et al.* employed a two-dimensional CFD model to study liquid behavior under two phase counter current flow [26]. Two geometries were studied: a vertical, flat plate and a vertical, corrugated plate. The corrugations were made to approximate those found in the commercial packing Mellapak 250Y by Sulzer ChemTech. Each plate had an identical plate positioned 12 mm from the first. Liquid was introduced from the top of one plate while gas flow was introduced at the base of the other. Pressure outlet boundary conditions were present at the top and bottom of the plates. The research simulated water flows of 50, 90, and 100 $m^3/m^2*h$ and toluene flow of 10, 15, 30, 50 $m^3/m^2*h$. Both the simulation and experiment failed to achieve total water coverage of either plate. The water formed streams in both cases. By contrast, the toluene achieve complete wetting in both simulation and experiment. The simulation predicted that the effective area of toluene would surpass the area of the packing due to wave formation.

In 2007, Raynal *et al.* employed a multi-scale approach which incorporated CFD to model gas-liquid flow through a column equipped with structured packing [27]. First, liquid-wall and gas-liquid interactions were modeled using the VOF package in a two-dimensional approximation of Mellapak 250Y. This simulation was used to obtain approximate liquid hold up and interfacial velocities. Next, meso-scale simulations were conducted with a subset of packing which corresponded to a channel intersection plus half of the channels on each side. This geometry was considered to be periodic in the z and y directions. Gas only simulations were performed in this geometry with the velocity

predictions modified to account for the reduced volume predicted by liquid hold up found in the first simulation. Irrigated pressure drop was simulated by imposing a moving wall boundary condition to approximate liquid flow. Lastly, a column sized geometry was created. CFD simulations were carried out on this scale by approximating the packing as a porous medium. The liquid hold up and pressure drop found previously were used to fine tune the porous media properties.

Mahr *et al.* approximated structured packing as a porous media [33, 34]. With this approximation, a macroscopic column (0.288 m diameter x 0.84 m high, packed with four elements) can be modeled using the elementary cell model. The researchers introduced liquid feed from a point source immediately above the top most packing and simulated the radial spreading throughout the packing elements. Experimental validation of the predicted spreading was accomplished through the use of X-ray radiography to monitor liquid distribution in a two-dimensional section of packing. The elementary cell model was found to accurately predict liquid spreading over macroscopic scales.

In the preceding research, simulations were conducted with approximations to the actual geometry. The results show that CFD can be used in lieu of experimentation to develop predictive models of contactor performance. However, this method of simulation is inherently dependent upon empirical fitting and therefore cannot provide a rigorous analysis of column performance or be used for computer aided design of next generation contacting media. Modeling of constitutive geometry elements restricts study to small scale, local phenomena. Because the subsets are modeled independently, any analysis of distribution, hold up, or wetted area is precluded. The need to model the subsets independently also introduces error as adjacent geometries display complex interaction which cannot be account for *a priori*. As in the research of Mahr and Mewes, geometry approximations can be used to predict column scale performance. However,

the approximations require extensive fitting and are only valid for the specified packing design. In order to analyze the complex interactions of column scale variables and local transport phenomena, simulations must use accurate geometries modeled in their entirety.

Ferrua *et al*. used particle image velocimetry (PIV) to record the flow through a geometry containing packed spheres similar to horticulture packing for forced air cooling.[35] Particles were released through a narrow slit to constrain the possible starting points for measured streamlines. These results were used to validate the streamline predictions of CFD simulations. The CFD geometry employed non-contacting spheres with a diameter 99 percent of the sphere used to obtain experimental results. Results between experimental and simulated data showed an $r^2$ value of 0.89.

Jafari *et al*. studied flow through a randomly packed bed of hard spheres.[36] A smooth cylinder geometry and a rough cylinder geometry were used with velocity inlet and pressure outlet conditions. The pressure drop calculations matched data from the literature quite well. Interestingly, they developed an expression for dispersivity to be used in conjunction with their CFD program. Results to calculate permeability were compared to correlations (Kozeny-Carman's). The maximum error for pressure drop was less than 10 percent. Porosity results were close to the Kozeny-Carman's correlation at porosities below 0.6. Calculated dispersivities were in agreement with experimental results.

A coupled discrete element method (DEM) and CFD approach was employed by Bai *et al.* to study pressure drop of through packed bed reactors which have low tube-to-particle diameter ratios ($D/d < 4$).[37] DEM was used to create a simplified representation of spherical and cylindrical catalysts in a packed bed and CFD was used to model flow through the bed. The individual particles were shrunk to 0.5-2% of their diameter after "packing" to avoid particle-to-particle contact which complicates CFD meshing. This

created a discrepancy between the modeled and actual void fraction that would be observed with these particles. The authors remedied this by multiplying all CFD predicted press drop by a "pressure correction factor." This allowed the results to be compared with experimental results taken from a lab scale packed bed (~150 particles) and an industrial scale packed bed (~1500 particles). The authors used the standard k-ε model, the realizable k-ε model, RNG k-ε model, the Spalart-Allmaras model, the standard and SST k-ω models, and the Reynolds Stress Model(RSM) to model the flow. All turbulence models used under predicted the pressure drop both before and after correction for void fraction. The Spalart-Allmaras model displayed the most error and the RSM model proved to be most accurate. While the RSM models were most accurate, the runtime for these models was nearly three times longer than the remaining models and the accuracy only improved by 3%. The k-ε and k-ω were roughly equivalent in their accuracy. Each model proved to be within 10% of the measured value prior to void fraction correction. It was concluded the RNG k-ε model was most appropriate to this type of simulation.

Fernandes *et al.* compared the performance of CFD simulations to experimental studies involving ambient air and supercritical $CO_2$, separately, under both laminar and turbulent conditions.[38] Turbulent simulations employed the Realizable k-ε turbulence model. Empirical parameters were determined to account for the drag and permeability associated with the porous gauze packing. The first geometry simplified the SULZER EX Gauze packing to two contacting corrugated sheets. Velocity inlet (bottom) and pressure outlet (top) conditions were specified. Average deviation of pressure for the supercritical $CO_2$ flows was 15%. The second geometry approximated a single packing element, shown in figure 10, with an OD of 24 mm. This packing element model was able to predict dry pressure drop with an average deviation of 6%. Each geometry

employed a tetrahedral mesh with a 0.31 mm minimum element size. Hexahedral meshing was attempted by abandoned due to unavoidable low mesh qualities.

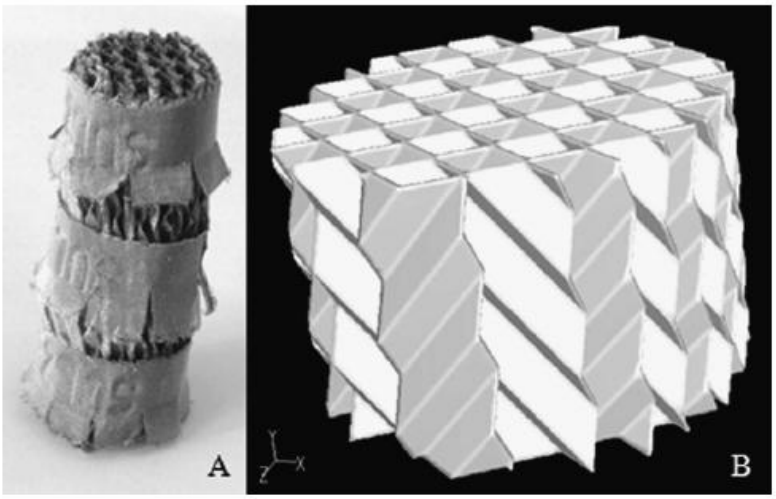


Figure 10: The packing and CFD geometry used in Fernandes *et al* (2008).[38]

The 2008 Fernandes study was extended to address liquid film-flow.[39] A Euler-Euler approach was combined with the volume-of-fluid (VOF) multiphase model. Two models were employed. Two-dimensional liquid film flow down a corrugated surface was modeled first to obtain approximations of film thickness. This information was then employed to generate a three-dimensional geometry with periodic liquid in- and outflow boundary conditions (figure 11). Simulation predictions were found to accurately capture the trends of pressure drop as a function of flow rate.

Relative errors for the pressure drop calculations were 20.3% for dry and 23% for irrigated. The authors hypothesized these errors were due to uneven gas and liquid distribution, lack of flow channeling and lack of liquid back mixing predicted by the model. HETP calculations had a relative error of 9.15%. The errors were attributed to assuming uniform distributions in the liquid and vapor phases.

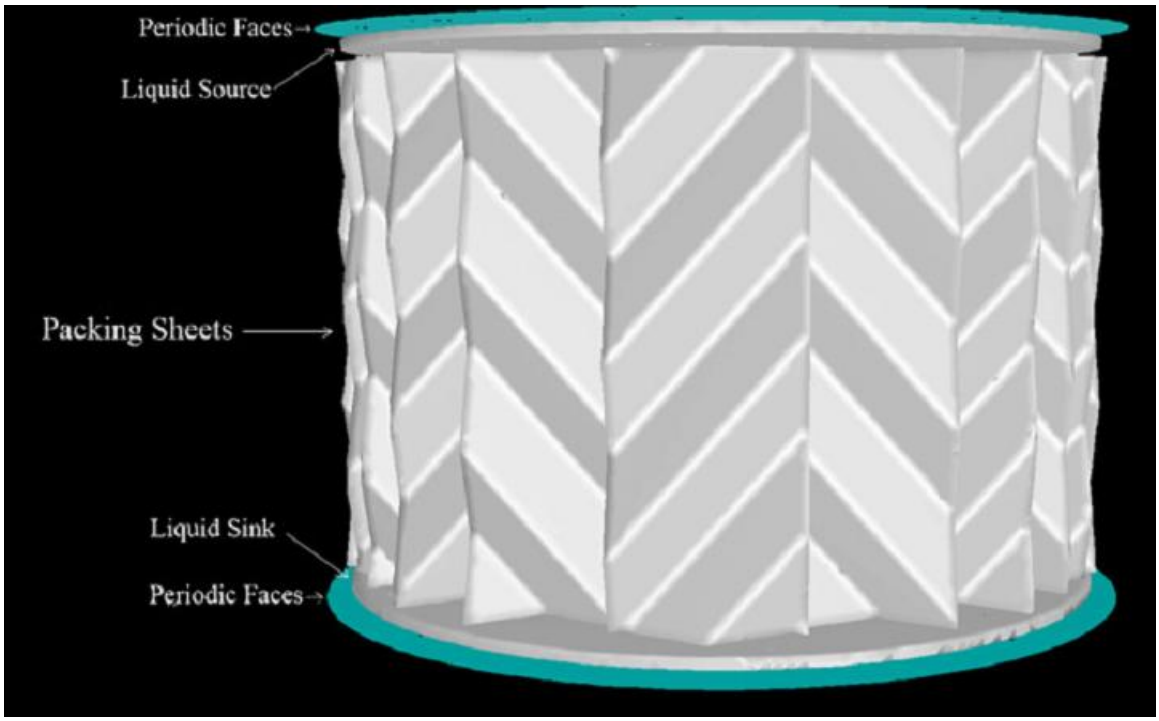


Figure 11: The packing element geometry employed in Fernandes *et al* (2009).[39]

# Chapter 3: Simulation Method

This work simulated single phase flows against gravity through multiple structured packing elements. The core geometry was generated from a CT scan of a single half-height packing element. The full geometry was constructed in ICEM and a surface mesh exported in STL format. Meshing, computation, and post processing were performed in the Star-CCM+ software package. Separate single phase simulations were conducted with nitrogen and water as the continuous phase. The nitrogen flows employed represent the range of rates commonly encountered in the vapor phase of industrial distillation. Water simulations were carried out to test the validity of using similarity theory to generalize simulation results across multiple fluids.

## GEOMETRY

X-ray Computed Tomography (CT) scans were used to quickly obtain a high-fidelity electronic representation of structured packing. In X-ray CT, the transmittance of X-ray beams through an object are measured from many different projection angles as the object or emitter/detector pair is rotated (see figure 12). X-ray attenuation is roughly proportional to density. Therefore, each scan corresponds to the superposition of all the densities along the beam's path. The purpose of taking scans from multiple angles is to obtain many unique beam paths. This allows deconvolution algorithms to regress the density at each point. The result is typically displayed as a three dimensional density map of the scanned object. X-ray CT is a common non-destructive testing technique by virtue of being able to see inside objects without the need to physically alter the object.

A 450 kV, 1.3 mA unfiltered fan beam X-ray was paired with a 512-channel cadmium-tungstate solid-state linear array detector to perform all CT scans. A single beam captured one sample per view with an integration time of 20 ms, and each rotation

was repeated with a half-detector offset to double detector coverage, improving image resolution. Slice thicknesses were 0.3125 mm with an inter-slice spacing of 0.3 mm. 1,400 views (angular positions) were used for each slice. The source-to-object distance was 752 mm, resulting in a 159.24 maximum field of view.

Ring artifacts were removed using the IDL routine "RK_SinoRingProcSimul" developed at the University of Texas. Reconstruction utilized beam hardening coefficients [0, 0.6, 0.05, 0.05]. Reconstruction parameters were set so that air had mean value of 10,000 and other materials maximally filled the available 16-bit data space (i.e. 65,536 possible data values). The scan and post processing yielded 547 512x512 16-bit TIFF slice images. These images were converted to an STL file using VGStudioMax 2.0. The threshold was set at 19,026 with super-precise quality and no simplification.

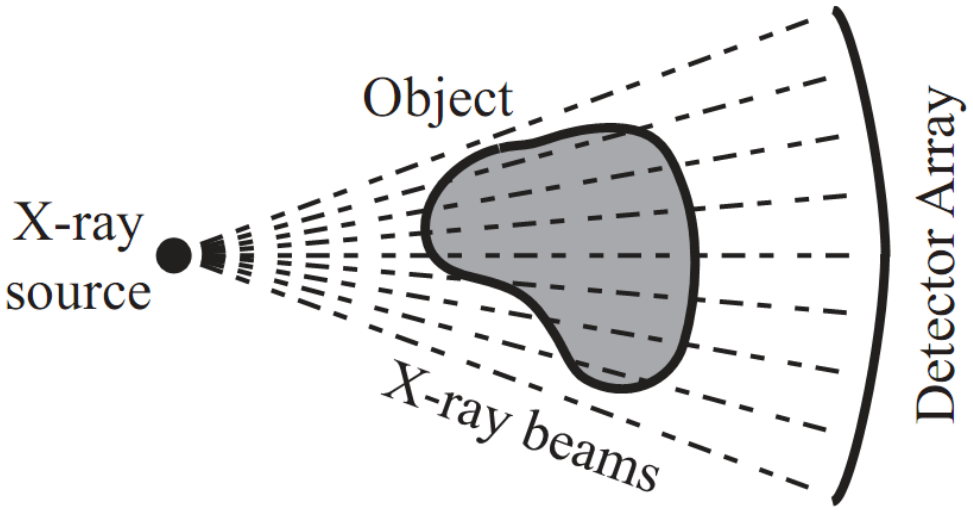


Figure 12: An overhead view of a fan beam and linear array X-ray detector.[40]

Two distinct geometries were generated by scanning Mellapak N250Y packing. The original intent of this project was to document the physics occurring at the packing

joint. To that end two packing half-elements were scanned while stacked in a 146.05 mm ID polycarbonate cylinder analogous to the experimental column. The scan captured a 154 mm vertical distance centered at the joint. The scan results are shown in figure 13.

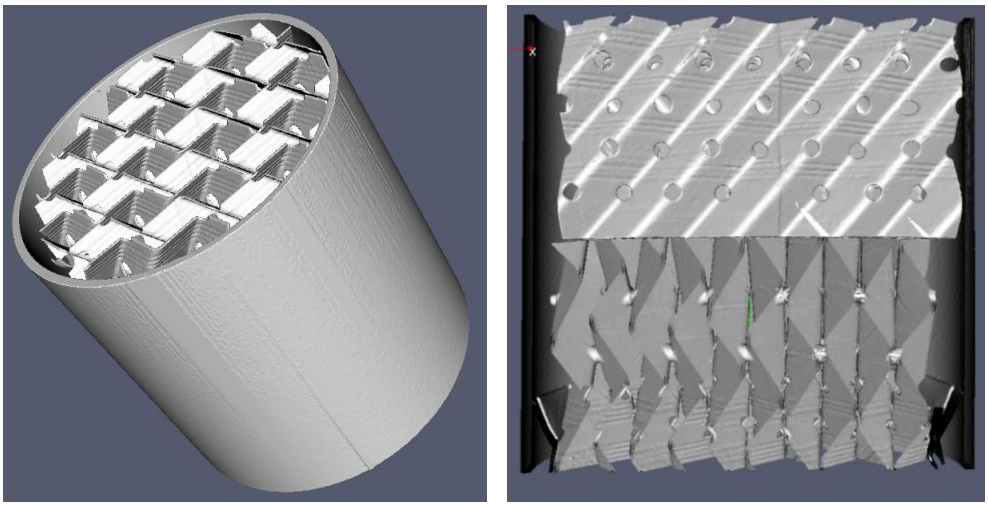

Figure 13 - The geometry resulting from a scan of the packing joint is shown in isometric (left) and bisected (right) views.

It is common to situate material inlet and outlet boundaries well removed from the start and end of flow obstructions. This creates a simplistic region prior to the geometry in which the velocity profile is allowed to build naturally and a similar region following the geometry where recirculation caused by flow separation can dissipate without affecting the simulation mass balance. This required that a cylindrical extension be mated to the column wall already present in the scanned geometry. The ANSYS geometry and meshing software package ICEM v11.0/12.0 was employed for the manipulation of volume elements and creation of boundaries. The STL file generated from the CT scans was imported directly into ICEM as a triangulated surface.

Unfortunately, the accuracy discrepancy between the scan data (16-bit) and the computer generated data (64-bit) prevented the construction of a water-tight hybrid

column wall. The lip of the scanned column was slightly out of round and ragged due to the effects of extruding and machining the plastic tube. This prevented a computer generated circular curve or surface from being fused to the column wall. As an alternative, a curve was extracted based on the angle of connectivity of adjacent triangles. At the rim of the scanned column, adjacent triangles with acute angles greater than 80 degrees necessarily describe boundary between the side of the column wall and the perpendicular edge created at the outer extents of scanning (see figure 14).

A closed curve was generated in ICEM based on the common edges of triangles with acute angles greater than 80 degrees. This curve was then duplicated at the desired inlet boundary and a surface generated between the two identical curves. The duplicated curve also formed the pressure outlet boundary condition. The higher accuracy of the computer generated elements meant that their position in space was specified more precisely than that of the scan generated points. This caused the geometry software to interpret the scan data as occupying a distinct point in space when compared to the computer generated data. This led to gaps between the imported and generated surfaces (shown in figure 15). The ICEM vendor was engaged to assist in solving this problem. However, no solution was found despite an extensive trial and error campaign. Additional computational resources were made available for geometry generation and simulation during this campaign. These two factors resulted in a decision to utilize a more complex geometry in order to bypass this error and increase the impact of the research.

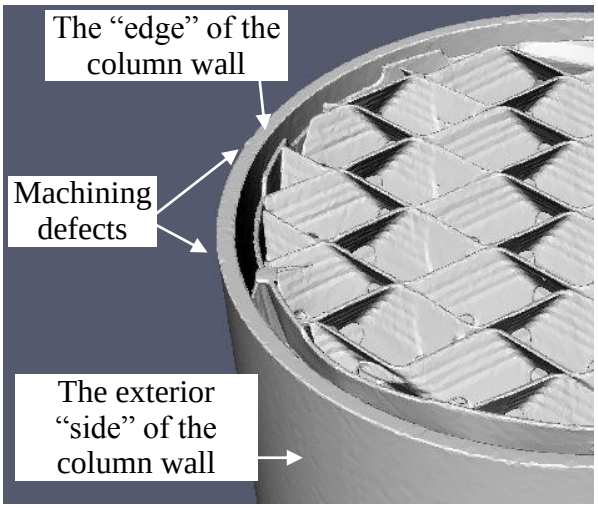


Figure 14 - A detail of the scan geometry delineating the portions of the column wall referred to in the text.

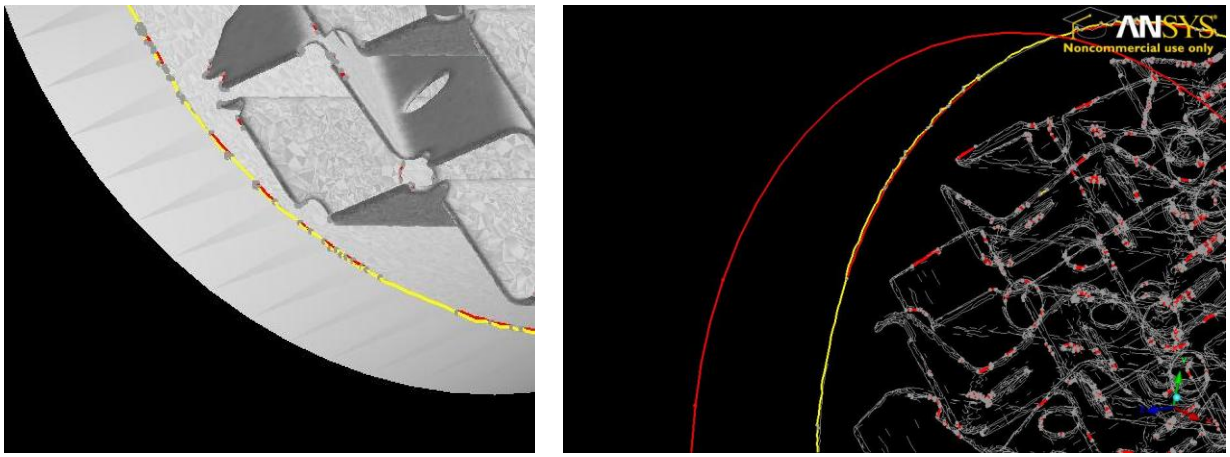


Figure 15 - This figure color codes the gaps (yellow) between the scan data (triangulated) and computer generated surface (smooth) in both solid (left) and wireframe geometries (right).

The expanded research goal was to model three distinct packing elements; capturing both the physics at the joint as well as the mid packing regions and the transitions between the two over the course of a packing stack. This would be more informative of actual column behavior and could be accomplished by importing the

results of scanning a single packing element. Therefore, the central 154.87 mm of a half-element of Mellapak N250Y was scanned in the same manner described previously without the polycarbonate column. Again, the STL file was imported into ICEM for manipulation. The scan intentionally ignored the first and last mm of packing to create a flat plane perpendicular to the packing axis. Figure 16 shows the results of the packing element scan and without a containing geometry.

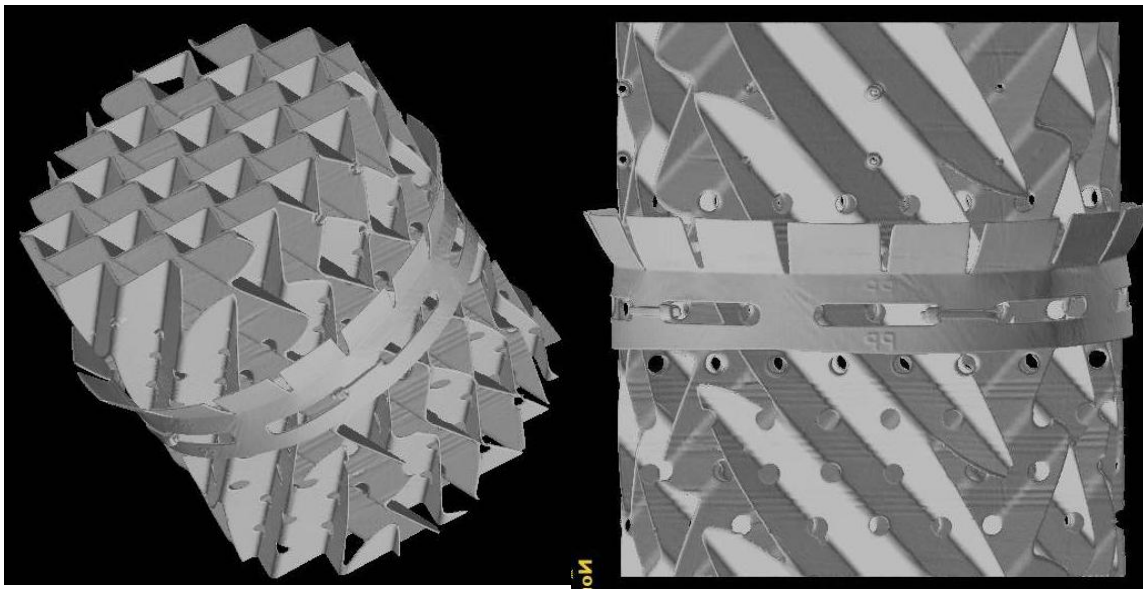

Figure 16 - Shown here is the geometry (isometric view at left, side view at right) generated by scanning a single half-element of Mellapak N250Y.

The imported scan data was copied, translated along the Z-axis, and rotated 90 degrees. This procedure was then repeated with the copied data to create three packing elements such that the second element is rotated 90 degrees and the third element is rotated 180 degrees relative to the first element. This is shown in figure 17. The base of each element was spaced 0.01 mm from the end of the previous element to prevent contact errors. This gap is also small enough that the intended mesh size will not resolve the space.

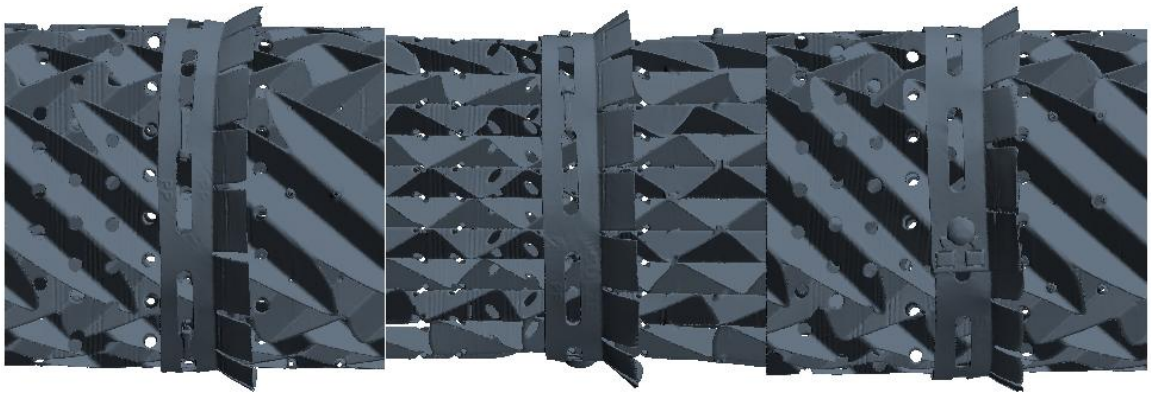

Figure 17: The packing stack consisted of three half elements of Mellapak N250Y.

In order generate a tight fitting column wall, the X and Y coordinates were polled at 14 points (listed in table 1) along the outer perimeter of the complete packing stack. A circular curve was then fit through these points. The curve was moved 190.5 mm below (down the Z-axis) the base of the lowest packing element. This curve was also copied to a point 113.406 mm above (up the Z-axis) the top of the last packing element. These circles were used to define surfaces within their respective boundary. These would be used as velocity in and pressure out boundaries. A third surface was generated between the two curves to serve as a column wall. The location of all geometry elements along the Z-axis is summarized in table 2.

Table 1: Fourteen points were used to define a circle in the XY plane just beyond the perimeter of the packing stack.

| | | | | | | | |
|---|---|---|---|---|---|---|---|
| X-coord (mm) | -72.251 | -59.422 | -34.817 | -12.111 | 34.064 | 53.658 | 72.348 |
| Y-coord (mm) | 5.928 | -33.753 | -57.390 | -77.581 | -68.351 | -37.303 | -11.800 |
| X-coord (mm) | 78.694 | 72.326 | 55.461 | 16.502 | -39.335 | -70.236 | -78.418 |
| Y-coord (mm) | 34.064 | 53.782 | 71.415 | 78.384 | 72.251 | 59.521 | 32.986 |

The geometry had to be saved in an open format readable by Star-CCM+. The STL file format was chosen for consistency. The geometry generated in ICEM is of the type B-Spline and had to be converted to a faceted geometry format. The faceted and triangulated STL geometries were then merged by converting to an unstructured mesh. This allowed the export of a single STL file representing the combined geometry.

Table 2: The location and spacing of relevant geometries.

| Geometry Element | Location on Z-Axis (mm) | |
|---|---|---|
| | Beginning | End |
| Velocity Inlet Plane | -12.523 | |
| 1st Packing Element | 177.8 | 332.667 |
| 2nd Packing Element | 332.677 | 487.544 |
| 3rd Packing Element | 487.554 | 642.421 |
| Pressure Outlet Plane | 755.827 | |

## MESHING

The combined geometry STL file was imported into Star-CCM+ for meshing. At this point, the geometry consists of multiple data generated by two methods and with differing accuracies as described above. The Star-CCM+ Surface Wrapper was employed in order to increase the global geometry quality. The function of the Surface Wrapper is often described as "shrink wrapping" the selected geometries. The Surface Wrapper improves a geometry by filling holes or gaps while eliminating duplicate data and internal features. The Surface Wrapper will also overwrite surface data to standardize the data format and accuracy across the whole geometry. Leak detection was

performed on both the flow volume and packing internal volumes after running the Surface Wrapper. All volumes were found to be water-tight and suitable for meshing.

The Surface Remesher, Tetrahedral Mesher, and Polyhedral Mesher routines were invoked serially to generate the final volume mesh. Because an STL file utilizes triangulated surfaces, a surface mesh was already present on the imported data. This mesh was, however, based on the desired file size rather than the effect it would have on simulation accuracy. The Surface Remesher was used to overwrite this low quality mesh with one expressly suited to CFD calculations. Most CFD studies generate a volume mesh by extrapolating a triangular surface mesh to form pyramids or tetrahedral volume elements. The downside to rigidly enforcing a four-sided volume element is that these volumes can become highly warped or skewed when describing the volume between or near highly angular surfaces. This has given rise to a new meshing method which employs many-sided or polyhedral volume elements. The polyhedral elements can be packed more efficiently into acute spaces without becoming misshapen. Another benefit is realized by merging adjacent tetrahedral volumes to form a single polyhedral volume. Merging adjacent pyramid shapes results in a minimal increase in edge length while reducing the mesh volume count by a factor of two or more. This allows polyhedral meshes to converge in fewer iterations than the tetrahedral equivalent without sacrificing accuracy. Polyhedral meshes also result in a much smaller file size.

The size and complexity of the constructed geometry prevent the use of a uniformly spaced mesh. Therefore, adaptive meshing was employed to generate a mesh with the requisite accuracy while minimizing the file size and computation time. This process allows the user to globally specify the acceptable range of parameters such as maximum or minimum mesh element size, cell growth rate, or minimum mesh quality. The software then autonomously generates a relatively simplistic mesh throughout the

geometry. Once a complete mesh is present, the software proceeds to step through the existing mesh and refine the grid spacing. The mesh is iteratively refined on the basis of the specified parameters as well as geometry complexity. A more detailed mesh is required to accurately capture complex flow fields. Therefore, the adaptive meshing algorithms will also refine the mesh based on the distance to walls or the local geometry density.

This study employed three meshes to evaluate the effect mesh density would have on the converged solution. The manipulated mesh variables consisted of the number of points to define a circle, the surface growth rate, growth factor, and the tetrahedral/polyhedral density. Requiring more points to define a circle increases the number of mesh vertices used to describe a given curve and results in a more accurate simulation of flow across or near curved surfaces. The surface growth rate controls the allowable edge length increase in adjacent surface triangles. A larger number will result in a more sudden transition from fine to coarse areas within the surface mesh. The tet/poly density parameter affects the global volume element density. That is to say the total number of volume elements scales roughly linearly with this number. The tet/poly growth factor functions in a similar manner to the surface growth rate with the obvious caveat that it applies only to volume elements.

The minimum edge length was not changed between the meshes but deserves mention as it is the only absolute parameter which was specified. The minimum edge length is an inviolate restriction on the enhancements made by an adaptive meshing program. This study employed a minimum edge length of 0.45 mm in all three meshes and used the default values for the remaining parameters in the first or coarse mesh. The medium and fine meshes changed these parameters such that they would have increased

resolution compared to the coarse mesh. The parameters used in this study are summarized for each mesh in

table 3 while all of the settings used are present in the Appendix: Mesh Settings.

Table 3: The mesh generation parameters for each mesh are listed here.

| Parameter | "Coarse" Mesh | "Medium" Mesh | "Fine" Mesh |
|---|---|---|---|
| # Pts/circle | 36 | 48 | 48 |
| Surf. Growth Rate | 1.3 | 1.2 | 1.1 |
| Minimum Edge (mm) | 4.5 | 4.5 | 4.5 |
| Tet/Poly Density | 1.0 | 1.0 | 1.05 |
| Tet/Poly Growth Factor | 1.0 | 0.98 | 0.97 |

Meshing was performed on the Texas Advanced Computing Center (TACC) high performance visualization cluster known as Spur. The coarse mesh was created on a standard visualization node. These nodes are equipped with 4-quad core AMD Opteron processors, 128 GB of RAM, and 1 Nvidia QuadroPlex 2100 S4 (4 FX 5600). The medium mesh required extra memory and was generated on the "visbig" node which is equipped with 8 dual-core AMD Opteron processors, 256 GB RAM, 2 NVIDIA QuadroPlex 1000 Model IV (2 FX 5600 each). These meshes were generated in less than the allotted 24 hr runtime. The fine mesh was also generated on the "visbig" node but required an extended runtime of 30 hrs.

**SIMULATION**

CFD simulations were conducted in Star-CCM+ on the TACC high performance computing cluster known as Ranger. Ranger contains 3,936 nodes each of which is equipped with 4-quad core AMD Opteron processors and 32 GB of PC2-5300 RAM.

Intra node communication is conducted on a HyperTransport, 6.4 GB bidirectional Infiniband switch. Simulations were conducted using 480 – 544 cores (30 -34 nodes).

Star-CCM+ supports the following turbulence models: Spalart-Allmaras, Reynolds Stress Model (RSM), K-Omega (k-ω), and K-Epsilon (k-ε). The Spalart-Allmaras model uses a single independent closure equation and was judged to be too simple for the detailed analysis desired in this research. The RSM occupies the other end of the spectrum using an independent equation to calculate each additional term in the RANS equations. This model is widely regarded as the most accurate commercially available turbulence model; however, it suffers from excessive computation time and is often used only as comparative point to evaluate other models. The k-ε and k-ω models each use two independent equations for closure and are very popular in the CFD field. A literature search showed that the k-ε model and its derivatives are more commonly employed of the two when studying chemical engineering flow applications.

Many improvements have been made to k-ε turbulence model since its original formulation. One much lauded improvement is the Realizable approximation. The Realizable k-ε model uses an improved equation to calculate the turbulent dissipation rate, ε.[12] The Realizable model also expresses the $C_\mu$ coefficient as a function of the mean flow in lieu of keeping it constant as in the standard k-ε.[12] The Realizable k-ε is typically expected to give results as accurate as or better than the standard application for most flows.

A second common improvement is the use of two-layer theory which allows the k-ε model to be applied in the viscous sublayer which negates the need for wall functions.[12] This is accomplished by modeling ε differently based on the distance from the wall. In the layer adjacent to the wall, turbulent viscosity ($\mu_f$) and ε are specified based on the distance from the wall. However, ε is computed from the transport equation

at points far removed from the wall. These values are blended in the intermediary region. Due to the complexity of the flow and the significant surface area exposed to the fluid, this research employed the two-layer, realizable k-ε model. A single flow simulation was repeated with the k-ω model and the RSM to judge the wisdom of this choice.

Initial simulation efforts modeled the nitrogen flow as a steady, incompressible flow with a segregated solver. A segregated solver calculates the velocity and pressure terms independently of one another. This allows for more ambitious iteration steps and quicker convergence. Unfortunately, this solution method proved unstable. Next a coupled solver was used to model the flow as constant density. This method proved very robust and arrived at a solution for all flows.

The lowest nitrogen and water flow simulations were initialized with a constant velocity and pressure profile. Subsequent simulations were initialized from the converged solution of a previous flow rate. In each iteration, the area-weighted-average-pressure was calculated in a plane 25.4 mm below the packing stack and in a second plane 25.4 mm above the packing stack. These values were used to calculated pressure loss across the stack which was in turn used to monitor convergence. All simulations were run until the pressure loss changed by less than 0.001 Pa between subsequent iterations.

Distillation vapor rates are commonly referred to in terms of the F-factor ($F_S$). This is defined as the product of the superficial, linear velocity and the square root of the vapor density;

$$F_S = u_G \left(\rho_G\right)^{1/2}. \qquad \text{Equation 8}$$

As a general rule, columns are prone to flooding if run above F-factors of 2.4 m/s*(Kg/m$^3$)$^{1/2}$.

Nitrogen simulations were conducted at $F_S$ = 0.610, 1.22, 1.83, 2.45, and 3.05 m/s*[Kg/m$^3$]$^{1/2}$. The entering flows were specified as a mass flow rate at the suggestion of the CFD vendor. This is in contrast with many CFD studies which specify the linear velocity flux through the inlet boundary. The use of a total mass flux enables the software package to adjust the local flux across the inlet boundary while maintain the same superficial flow rate. One advantage is the extra degree of freedom presented at the intersection of the inlet boundary and the no-slip boundary imposed at the column wall. The result is a more representative flow profile.

The water flow rates were selected to match the Reynolds numbers used in the nitrogen simulations. There is some debate as to the correct calculation of Reynolds number in structured packing. This research sought to avoid this debate by using nearly identical geometries. The overlap in geometries allows the velocity of the fluid of interest (water) to be calculated using only a ratio of the fluid properties and the velocity of the original fluid (nitrogen) because the characteristic diameter drops out (see equation 9 and equation 10). For simplicity sake, the column ID and fluid superficial velocity are used to calculate representative Reynolds numbers. This data is compiled in table 4. The physical properties for each fluid were taken from DIPPR and are shown in table 5.

$$N_{\mathrm{Re},H_2O} = N_{\mathrm{Re},N_2} \Rightarrow \left(\frac{Dv\rho}{\mu}\right)_{H_2O} = \left(\frac{Dv\rho}{\mu}\right)_{N_2} \qquad \text{Equation 9}$$

$$v_{H_2O} = \left(\frac{\rho}{\mu}\right)_{N_2}\left(\frac{\mu}{\rho}\right)_{H_2O} v_{N_2} \qquad \text{Equation 10}$$

Table 4: A summary of the simulated flow rates.

| Desired $N_2$ $F_S$ | $N_2$ mass flow | Reynolds Number | $H_2O$ |
|---|---|---|---|
| $m/s*(Kg/m^3)^{1/2}$ | (Kg/s) | (unitless) | (Kg/s) |
| 0.610 | 0.012941 | 5,901 | 0.72093 |
| 1.22 | 0.025608 | 11,802 | 1.4419 |
| 1.83 | 0.038411 | 17,702 | 2.1628 |
| 2.44 | 0.051215 | 23,603 | 2.8837 |
| 3.05 | 0.064019 | 29,504 | 3.6046 |

Table 5: The physical properties used in simulations.

| Property | Nitrogen | Water |
|---|---|---|
| Density ($kg/m^3$) | 1.14527 | 995.831 |
| Viscosity (Pa-s) | 1.78837e-5 | 9.7906e-4 |

## SCALING

A scaling analysis was performed to determine the point-of-diminishing returns with respect to the number of processors to use for parallel computations. This is necessary because increasing the total number of processors has two competing actions. The obvious effect is accelerated computation because each processor has fewer calculations to perform. However, CFD calculations are highly interdependent. Therefore, the processors must share the results of their computation to solve the flow field. As the number of processors increases, so does the time required for data to be disseminated throughout the processor cloud. Once a critical number of processors is

surpassed the need for data sharing will result in decreased computational speed per processor.

The typical method of measuring how a simulation scales is to compare the ratio of run times against the ratio of processors. For instance, if a simulation was ran with 50 processors and then reran with 100 processors, the expected speed up would be 100/50 = 2. This would be compared with the run time at 50 processors divided by the run time with 100processors. This would then be repeated with additional processors. Each time, the result would put in ratio to the base case. At some point, the observed speed up (base run divided by the run time with x processors) will plateau. This will denote a point beyond the optimal scaling.

This study used 10 nodes (160 processors) as a base case as this is the smallest number of nodes which would load the simulation. The simulation was run for 100 iterations with iteration elapsed time reporting activated. The first iteration includes non-computational tasks such as partitioning and was therefore ignored. The run time was calculated as the sum of the iteration time for iterations 2 – 100. This procedure was then repeated; each time with 5 additional nodes (80 processors). The results were interpreted as described above.

# Chapter 4: Experimental Methods

An experimental campaign was conducted in order to obtain data against which simulation predictions could be validated and to quantify the effect of packing joints on pressure loss. All experiments measured the pressure loss of single phase flow against gravity through plastic Sulzer brand packing with a specific area of 250 $m^2/m^3$ (commonly referred to by its model: Mellapak N250Y). An example of this packing is shown in figure 18. This packing had perforations, wiper bands and surface enhancement.

In total, this project studied three packing configurations and two fluids. In each experiment, the system was brought to a steady flow and the pressure loss recorded. Experimental order was randomized and each experiment included two duplicate runs at each flow rate. The average of each run was used for comparative analyses.

Figure 18: A whole (left) and half (right) element of Mellapak N250.

## EQUIPMENT

### Column

The column (shown in figure 20) was assembled from a cylindrical, aluminum base and two sections of 146.05 mm ID polycarbonate tube with flanges at each end. The flanges were used to connect the base to the tube and the tube sections to each other. In each connection, the upper flange was grooved to accept an O-ring. The base had eight holes drilled along its top rim to match the flange pattern on the tubes. Four of these holes (at 0, 90, 180, and 270 degrees) were threaded to accept 6.35 mm threaded rod. These rods ran the full height of the column, protruding beyond the uppermost flange. Nuts were tightened to this rod in a crossing pattern to generate uniform compressive force. The remaining holes were drilled smooth. Bolts, washers, and nuts were used in the smooth holes to secure the base to the flange at the bottom of the first tube section.

The base had a 33.4 mm (1" NPT) threaded process connection drilled perpendicular to its axis. This connection intersected a conical throat drilled along the central axis of the base (see figure 19). The throat was 76.2 mm in diameter at its top and 25.4 mm in diameter where it intersected the process connection. The flaring of this channel was meant to facilitate a more uniform flow distribution as the fluid entered the column.

The lower tube section was 764 mm tall and acted as a spacer in which the flow profile would develop prior to encountering the packing. The upper tube section was 966 mm tall. Pressure ports were installed in the upper section of tube at elevations of 127 mm, 699.3 mm, and 829.5 mm above the flanged tube connection (see figure 20, at left). At each elevation, four ports were spaced evenly around the column perimeter in a plane perpendicular to the column axis. A picture of the column, packed with two whole-

elements of Mellapak N250Y is show at right in figure 20. All three pressure measurement elevations are clearly visible in this figure.

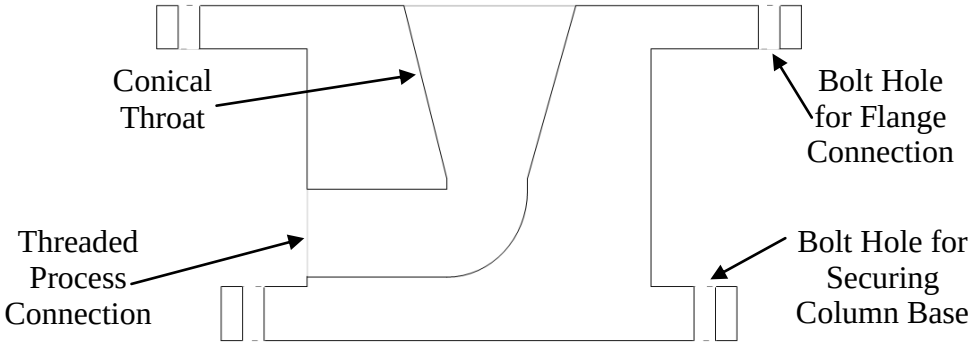


Figure 19: An aluminum base was used to connect to the piping and redirect flow into the column.

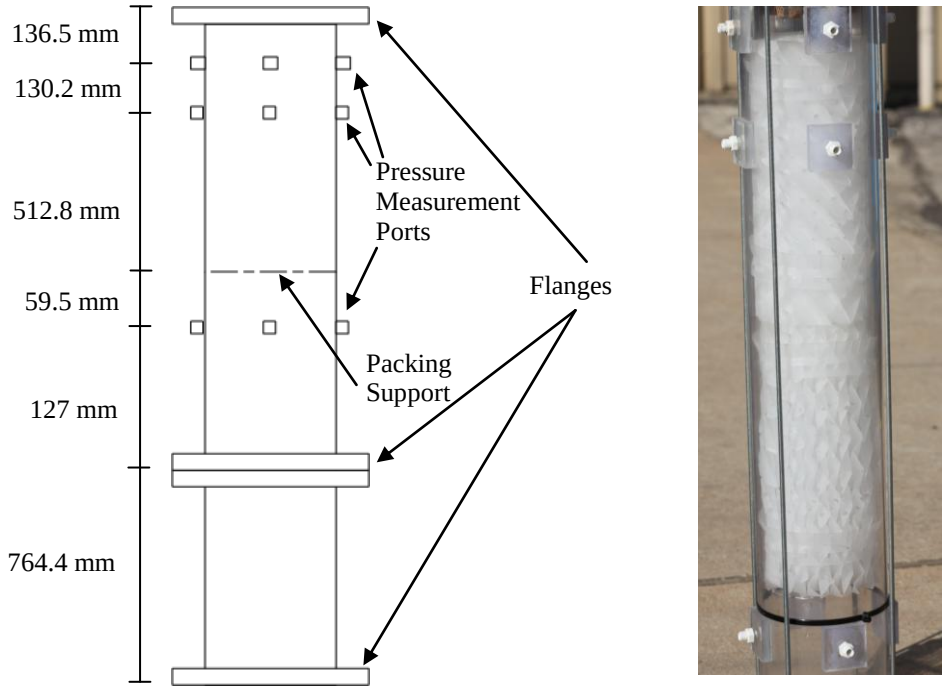


Figure 20: The column is shown schematically at left and in a picture at right.

A cap was used to permit recycled flow during water experiments. The cap was fashioned out of a solid polycarbonate cylinder 152.4 mm in diameter. A 15 degree cone was machined onto the underside of the cap. This acts to funnel the flow to the center of the cap where it enters a 25.4 mm hole. This hole turns 90 degrees and exits out the side of the cap. The exit is drilled and tapped to accept threaded piping 33.4 mm (1 inch NPT) in outside diameter.

**Packing Support**

The packing was supported 186.5 mm above the intersection of the polycarbonate tubes. The packing was initially placed on an aluminum grate (shown at left in figure 21) supported by legs which rested on a ring of plastic secured to the column wall just above the intersection of the polycarbonate tubes (see figure 20). This configuration contained many elements which were not present in the geometry used in the CFD simulations. This raised concerns that the additional drag created would introduce error when the comparing the experimental and simulation results. Therefore, the plastic ring and support grate were replaced with 1.59 mm wire.

Four holes were drilled and a single wire was fed from one side of the column, through the opposite wall, around the exterior of the wall, back into the column and out through the last hole (see figure 21). The wire was secured by compressing the tag ends to the column wall with vinyl strapping. This configuration provides minimal extraneous material to create drag or separation points to disrupt flow. All nitrogen experiments were repeated using this packing support. Unfortunately, the holes in the column wall could not be made water tight due to the increased operating pressure employed during water experiments. Therefore the experiments using water were not replicated with the wire packing support.

Figure 21: Two packing supports were used. A grate (left) and wires secured through the column wall (right).

**Flow Configurations**

Gas phase experiments were conducted with a single pass flow of building supplied nitrogen. All piping was flexible 38.1 mm (nominal 1.5 in) schedule 40 PVC. Nitrogen flow was fed to the system from wall mounted taps. A gate valve was installed at the tap and used to manually control flow. From there, the flow was split and fed through two mass flow meters in parallel to reduce pressure drop and allow study of higher flow rates. The flow was recombined after the meters and carried to the base of the column. Nitrogen flowed through the column and was then vented to the atmosphere. This configuration is diagramed at left in figure 22. The nitrogen temperature was monitored and found not to vary outside the range of 22.3 - 23.9 C. This roughly corresponds to room temperature and the thermal stability likely reflects a long residence in the nitrogen headers inside the climate controlled portion of the building.

The liquid phase experiments required a large volumetric flow rate in order to reach the desired Reynolds Number. Therefore a closed system was employed with a 2.24 kW variable speed pump. Early experiments revealed the large pumping power combined with a re-circulated system resulted in significant temperature swings as the flow rate changed. Therefore, the system was modified such that the pump output fed

directly to a heat exchanger. From the heat exchanger, the process fluid was split and fed to two mass flow meters. The flow was recombined after the meters and fed to the base of the column. After leaving the column, the fluid was fed to a vapor separation tank equipped with a vortex eliminator. Water was taken from the bottom of this tank and fed to the suction of the pump. This is diagramed at right in figure 22.

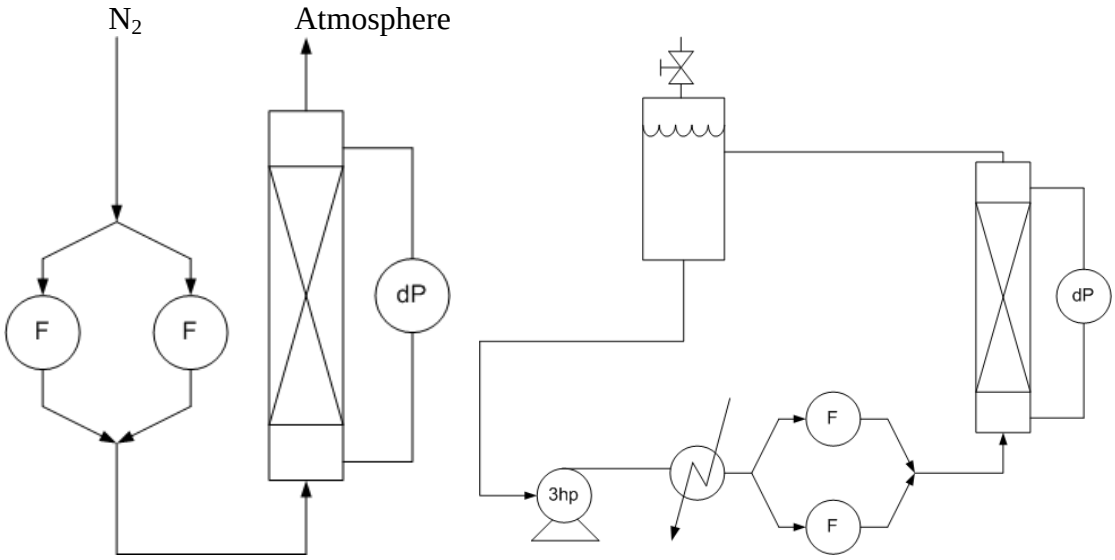


$N_2$ Flow Diagram $H_2O$ Flow Diagram

Figure 22: Experiments utilizing different fluids required the use of different piping.

**Instrumentation and Data Acquisition**

The process flow was run in parallel through two MicroMotion F50 flow meters. Both nitrogen and water pressure losses were initially measured using a Rosemount 3051 differential pressure transmitter. However, the pressure loss of nitrogen at low flows proved to be below the minimum accuracy of this sensor. Therefore, the nitrogen experiments were repeated with four MKS 226A differential pressure sensors measuring the pressure loss across the packing stack. This sensor permitted much more accurate

measurements but was not designed to measure liquid phase flows which prevent the water experiments from being repeated with these sensors.

The National Instruments USB-6008 data acquisition card was used for process monitoring. All instrumentation in this study used a 4-20 mA signal based on the scaled flow value (e.g. actual flow divided by max flow times 20 mA = signal current). The current signal is preferred because it is not sensitive to electromagnetic interference commonly found in industrial buildings. The current signal was converted to a 1-5VDC by placing a high accuracy (+/- 0.1%) 250Ω resistor in the current loop.

The flow meters utilized a "four-wire" configuration. This means the supplied power and the signal output are on different circuits. Therefore, the signal wires were connected directly to the AI terminals which were bridged with a resistor (see figure 23, at left). The pressure sensors were wired in a "two-wire" configuration in which the signal and power supply wiring are integrated. The situation was further complicated by the need to share a single power supply amongst four sensors in the nitrogen experiments. In order to accomplish this, the positive and negative power leads were run to separate terminal blocks. This permitted each ΔP transmitter to form its own independent power loop by bridging the terminal block. The positive connection on each sensor was wired directly to the positive terminal while the negative connection was wired to the negative terminal with a high-precision resistor in serial. A schematic is provided in figure 23. The Rosemount sensor was wired in the same manner.

A LabView VI was written to monitor and record both flow and differential pressure. The flow and pressure values were read and displayed immediately upon activating the VI. A run duration counter was also activated immediately. This counter could be reset by the user. This allowed the user to make adjustments and then reset the timer to judge the steadiness of the system. The system also allowed the user to specify

when to start recording this data to disk and activated a separate timer to indicate how long data was taken. The front panel and wiring diagram are provided in Appendix: LabView VI Details.

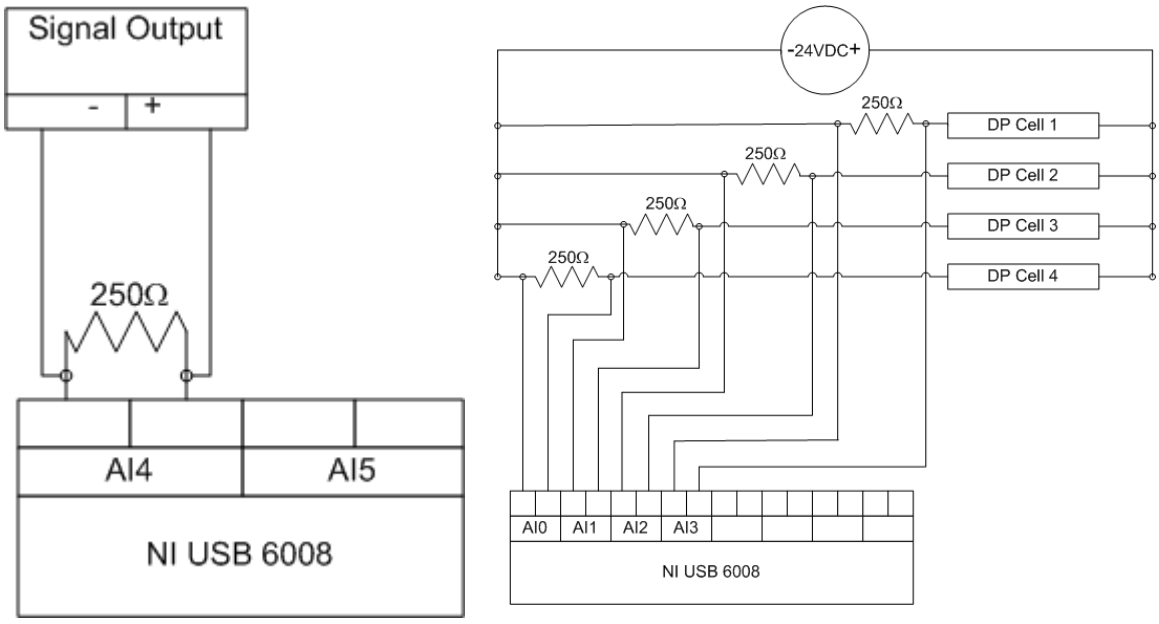


Figure 23: Differential pressure sensors were monitored and recorded using NI instrumentation and LabView software.

## PROCEDURE

### Nitrogen Experiments

Pressure loss measurements were taken across three packing stacks (three half-elements, four half-elements, and two whole-elements of Mellapak N250Y ) at nitrogen flows of $F_S$ = 0.610 - 3.36 m/s*$(Kg/m^3)^{1/2}$. The specific flows are compiled in table 6. Each experiment followed a randomized list of flow rates which included two duplicate runs.The lowest pressure ports were used as the "high" leg for all ΔP measurements. The middle pressure ports were used as the "low" leg when studying flow through three half-elements while the highest pressure ports were used as the "low" leg while measure

pressure drop through two whole-elements or four half-elements. Any ports not in use were capped.

Table 6: A summary of the nitrogen flows studied.

| Nitrogen | | | |
|---|---|---|---|
| F-factor | | Velocity | |
| $F_S$ | | u | |
| $m/s*(Kg/m^3)^{1/2}$ | $ft/s*(lb/ft^3)^{1/2}$ | m/s | f/s |
| 0.610 | 0.5 | 0.570 | 1.87 |
| 0.915 | 0.75 | 0.855 | 2.81 |
| 1.22 | 1 | 1.14 | 3.74 |
| 1.53 | 1.25 | 1.43 | 4.68 |
| 1.83 | 1.5 | 1.71 | 5.61 |
| 2.14 | 1.75 | 2.00 | 6.55 |
| 2.44 | 2 | 2.28 | 7.48 |
| 2.75 | 2.25 | 2.57 | 8.42 |
| 3.05 | 2.5 | 2.85 | 9.35 |
| 3.36 | 2.75 | 3.14 | 10.3 |

A 9.525 mm ball valve at the wall was used to control the flow rate of nitrogen through the system. Prior to any experiment, the data acquisition VI was initiated to allow the user to monitor both flow and pressure drop. The flow was brought to the desired flow and monitored. Data recording was initiated once the system was judged to be stable for a period of at least three minutes. Data was taken for three minutes and then the experiment was repeated at the next flow rate.

**Water Experiments**

Water experiments were performed at Reynolds numbers which were calculated from the flow rates employed in the nitrogen experiments. Per similarity theory, this

should yield equivalent results. The specific Reynolds numbers and flows are presented in table 7.

The system was filled from the building water supply through a three-way valve located at the base of the column. The valve at the top of the vapor separation tank was left open to purge vapor from the system. The purge and three-way valves were closed once the system was full of water. The system had to be purged of air before data could be obtained. This process was as follows. Flow was slowly initiated via a variable speed drive connected to the pump. The three-way valve was opened slightly to pressurize the system to between 193 and 200 kPa as measured by a pressure gauge installed in the column cap. The flow rate was slowly increased with the system at pressure. As the fluid circulated through the system, air bubbles were entrained in the flow and accumulated in the vapor separation tank. The valve at the top of this tank was opened occasionally throughout this process to allow the accumulated vapor to escape. The three-way valve was opened as needed to maintain the elevated pressure. Once the system was at maximum flow and no more vapor bubbles were observed, the experiment could proceed. Experiments were taken with the system at a pressure of 193 to 200 kPa to avoid pulling a vacuum in the pump suction line.

Flow rate was manipulated by means of a variable speed drive connected to the pump. Once at the desired flow rate, the system was observed until the flow rate, fluid temperature, and pressure drop were observed to be steady for at least three minutes. Data was then recorded for three minutes and the procedure repeated at the next flow rate.

Table 7: Water flow rates were chosen such that the Reynolds number would match the nitrogen experiments.

| Nitrogen | | | Water | | |
|---|---|---|---|---|---|
| Velocity | | Reynolds # | Velocity | | |
| $F_S$ | u | $N_{Re}$ | u | q | m-dot |
| $m/s*(Kg/m^3)^{1/2}$ | m/s | unitless | m/s | $m^3/s$ | kg/s |
| 0.610 | 0.570 | 5,901 | 0.0365 | 7.24E-04 | 0.721 |
| 0.915 | 0.855 | 8,851 | 0.0548 | 1.09E-03 | 1.081 |
| 1.220 | 1.140 | 11,802 | 0.0730 | 1.45E-03 | 1.442 |
| 1.525 | 1.425 | 14,752 | 0.0913 | 1.81E-03 | 1.802 |
| 1.830 | 1.710 | 17,702 | 0.1095 | 2.17E-03 | 2.163 |
| 2.135 | 1.995 | 20,653 | 0.1278 | 2.53E-03 | 2.523 |
| 2.440 | 2.280 | 23,603 | 0.1461 | 2.90E-03 | 2.884 |
| 2.745 | 2.565 | 26,554 | 0.1643 | 3.26E-03 | 3.244 |
| 3.050 | 2.850 | 29,504 | 0.1826 | 3.62E-03 | 3.605 |
| 3.355 | 3.135 | 32,454 | 0.2008 | 3.98E-03 | 3.965 |

# Chapter 5: Results and Discussion

## GEOMETRY

The CT geometry was scanned in just over five hours while reconstruction took approximately two hours. The resulting STL file contained 5,439,254 triangles which occupied 251 MB when written with binary encoding. The ICEM created geometry proved to be water tight and easily imported into third party programs when exported as an STL file. The process of scanning, modifying, and exporting the geometry in a format readable by the CFD meshing program proved more expedient than and economically superior to quotes obtained for CAD generation of the same geometry.

An error was observed in the geometry. As can be seen in figure 24, the wiper bands are designed to exceed the column diameter. This compresses the wiper band as the packing is inserted into the column. The compression of the wiper bands ensures constant pressure between the wiper band and column wall resulting in an obstruction of the annular area. Due to the inability to obtain a representative and water tight geometry using the scans of packing elements *in situ*, the second scan was performed without a containing column. This means the scanned packing had a larger diameter than that of the experimental column. The difference was calculated to be approximately 12.8 mm.

The error was not detected until after a majority of the simulation campaign was completed. This prevented correction of the error. The larger diameter of the simulation geometry results in both an increased void fraction and a larger annular area relative to the experimental geometry. Increased void fraction should result in decreased pressure drop while the larger annular area might encourage the fluid to bypass the packing and flow along the wall; referred to as wall flow.

As mentioned above, this error is unfortunate and is expected to result in an inaccurately low simulated pressure drop. However, it does serve to illustrate the flexibility of CFD simulations in general. Simply put, the error is that the diameter in the simulation geometry is larger than the geometry of the experimental column but the volume of packing used in each is the same. Therefore the simulation has a higher void fraction than the experiment. This can also be expressed in terms of areas. The simulated annular area is larger than the annular area in the experimental trials, but the cross-sectional area occupied by packing is the same (discussed below in Nitrogen Simulation). Therefore, the ratio of annular-to-packed areas is unequal between simulation and experiment. Such differences are often thought to lead to inaccuracies when models created from data taken on lab scale equipment are applied to much larger industrial columns.

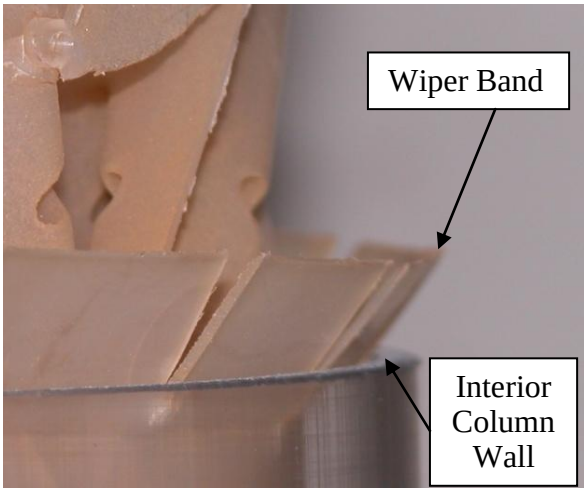


Figure 24: The wiper bands are made to exceed the column diameter.

Lab scale columns are typically less than 500 mm in diameter. Packing designed for these columns typically have a gap of 6 - 8 mm between the edge of the packing and the column wall; resulting in a packed to packed-to-annular area ratio of 0.024 for a

pairing of the largest diameter (500 mm) and smallest gap (6 mm). This contrasts strongly with industrial columns which can exceed 3,000 mm in diameter with a typical wall gap of less than 12 mm. Pairing a very small industrial column (1,500 mm) with a large wall gap (12 mm) yields an annular-to-packed area ratio of 0.016. This "best case" industrial ratio is nearly 40 percent smaller than the best case lab column ratio.

Such discrepancies make scale up of lab generated models inaccurate and typically require the determination of empirical parameters to fit the model to specific sized industrial columns. However, CFD is not limited by the wall gap provided by the packing manufacturer. The error described above could have been avoided had the packing been scanned without a wiper band installed. A wiper band could then have been generated once the packing was imported into the geometry generation program. This gives the researcher complete control over the thickness and degree to which the wiper band seals with the column wall.

**MESHING**

The meshing methods outlined above resulted in meshes with 35, 50, and 57 million polyhedral cells. In each instance, the conversion to a polyhedral mesh resulted in an 80 percent or greater reduction in cell count relative to the corresponding tetrahedral mesh. The data also suggested mesh size reduction was slightly more efficient in larger meshes. The polyhedral meshes resulted in file sizes between 18 and 30 GB. By contrast, the estimated file size for similar tetrahedral meshes would be between 200 and 340 GB using the common assumption of 1 GB per 1 million tetrahedral cells. These data are compiled in table 8.

The increased cell count of the tetrahedral meshes would significantly increase the computational complexity and, therefore, the time required to reach a converged solution. Similarly, the file size corresponds to a minimum amount of RAM required to

open a file. Ranger, like many HPC clusters, assigns available RAM relative to the number of processing cores requested. Therefore, the much larger tetrahedral meshes would necessitate significantly more processors to perform the needed calculations.

The accuracy of a given mesh can only truly be measured by comparing results of simulations which employ that mesh against those taken from analogous experimentation. However, the relative suitability of varying meshes can be evaluated by analyzing certain quality metrics; such as face validity and volume change. Face validity is an area weighted measure of the degree to which central cell-face normal vectors run parallel and away from their attached cell centroid.[12] Examples of good and bad face validity are shown in figure 25. Face validity below 0.5 indicates negative volume cells. A preponderance of these cells infers a poor quality mesh, either locally or globally.

Table 8: Summary of the various mesh characteristics.

| Parameter | "Coarse" Mesh | "Medium" Mesh | "Fine" Mesh |
|---|---|---|---|
| Tets | 2.00E+08 | | 3.38E+08 |
| Tet Wall Time (hr) | 4.81 | | 8.19 |
| Tet Mem (Gb) | 24.00 | | 49.30 |
| Polys | 3.49E+07 | 5.04E+07 | 5.74E+07 |
| Poly Wall Time (hr) | | | 19.04 |
| Poly Mem | | | 79163.13 |
| File Size (Gb) | 18.3 | 19.2 | 27.1 |
| Reduction in Cell Count | 82.5% | | 83.0% |

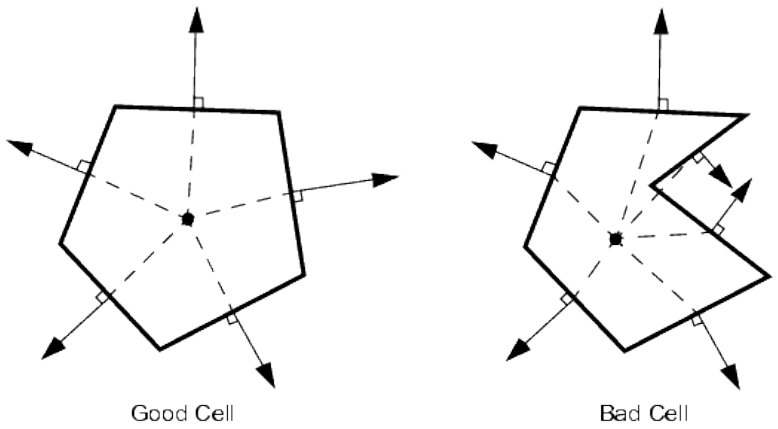


Figure 25: Examples cells with good and bad face validity.[12]

A cell's volume change refers to the ratio of a cell's volume to that of its largest neighbor.[12] A cell which has a volume equal to or greater than 1.0 will have a volume which is that is equal to or greater than all its neighboring cells. Very small volume change values correspond to sudden changes in cell volume. This is indicative of flat or sliver cells. Cells with a volume change below $1x10^{-5}$ denote poorly represented regions and can be the source of inaccuracy or create instability in the solver. The preferable values for both face validity and volume change are those approaching one.

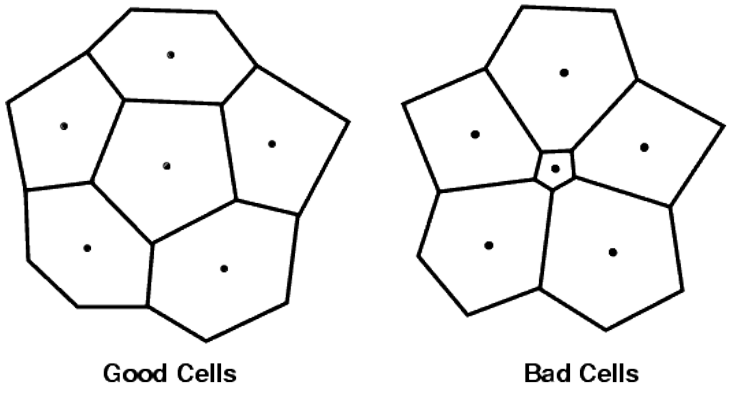


Figure 26: Examples of acceptable and unacceptable volume change.[12]

All three meshes report uniformly high face validity metrics with no mesh having any cells with face validity below 0.8448. The medium mesh could be judged to have the highest quality faces as no face had a quality below 0.957 and only a very small percentage of the faces fell below 1.0. The coarse mesh is the lowest quality when judged by the percentage of faces with a quality below 1.0. The fine mesh was responsible for the lowest face quality; however, it also had the lowest percentage of face qualities below 1.0. This is summarized in table 9.

The increase in the percentage of faces with quality equal to 1.0 corresponds to increased cell density and decreased cell growth rate. This enforces a smoother transition from fine to coarse cells in the volume and results in a higher packing efficiency. The higher efficiency reduces both the need for misshapen cells to bridge gaps between cells with disparate sizes and large cells being situated near complicated surfaces.

Table 9: The face quality statistics for each mesh.

| | "Coarse" Mesh | "Medium" Mesh | "Fine" Mesh |
|---|---|---|---|
| Face Validity | (# of cells) | | |
| validity = 1.00 | 34,860,691 | 50,360,527 | 57,392,387 |
| 1.0 > validity => 0.95 | 892 | 785 | 381 |
| 0.95 > validity => 0.90 | 34 | - | 4 |
| 0.90 > validity => 0.80 | 1 | - | 2 |
| 0.80 > validity => 0.70 | - | - | - |
| Minimum | 0.8772 | 0.9571 | 0.8448 |

The fine mesh performed much better as judged by the volume change metric having both the highest percentage of its cells in the highest quality range and having the highest minimum volume change. Once again the coarse mesh had the highest percentage of cells outside the top quality range but was not responsible for the lowest

volume change of the three. The medium mesh had the lowest volume change and was the only mesh to have a cell volume change below $1x10^{-5}$. Cells below this threshold are normally indicative of poor mesh regions. However, a lone cell with this poor quality is likely to be trivial and was therefore ignored. An increased number of smoothing and improvement iterations could possibly have corrected this cell.

Table 10: The volume change metrics for each mesh.

| | "Coarse" Mesh | "Medium" Mesh | "Fine" Mesh |
|---|---|---|---|
| Volume Change | (# of cells) | | |
| 1e-01 <= ΔV <= 1e+00 | 34,172,904 | 49,813,616 | 57,017,289 |
| 1e-02 <= ΔV < 1e-01 | 670,003 | 534,947 | 364,410 |
| 1e-03 <= ΔV < 1e-02 | 18,504 | 12,579 | 10,981 |
| 1e-04 <= ΔV < 1e-03 | 196 | 154 | 86 |
| 1e-05 <= ΔV < 1e-04 | 11 | 15 | 8 |
| 1e-06 <= ΔV < 1e-05 | - | 1 | - |
| 1e-05 <= ΔV < 1e-04 | - | - | - |
| Minimum | 1.22E-05 | 3.17E-06 | 2.15E-05 |

Figure 27 shows the packing geometry *sans* wall bisected by the XY plane with the front portion removed. In this figure, Z increases to the right. Figure 28 shows the mesh elements which lie in the plane used to perform the cut in figure 27. Samples of the coarse (figure 28, top), medium (figure 28, middle) and fine (figure 28, bottom) meshes. While this is not a complete picture of the meshed volume, it is reasonably assumed to be a representative sample.

The coarse mesh (figure 28, top), is modestly refined around the in- and outflow boundaries. The mesh grows quickly and large elements can be seen in the open region prior to and immediately downstream of the packing stack. The mesh transitions very abruptly to a highly refined mesh near the beginning (190 mm) and end (655 mm) of the

packing. The mesh is noticeably non-uniform throughout the packing stack. The mesh is relatively coarse in the intervals 267 - 345 mm and 423 – 500 mm. These increases in mesh size likely correspond to areas with higher local void fraction in which the high cell growth rate permits a rapid increase in cell size over a small distance.

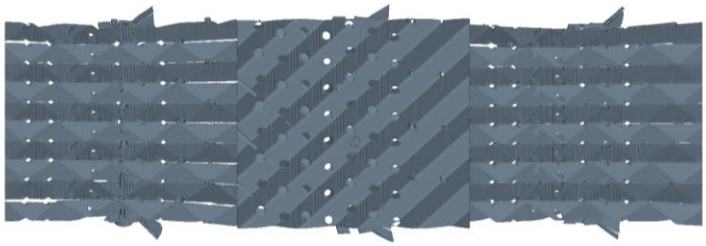

Figure 27: The packing geometry is shown with the front section cut-away by the XY plane and along the central (Z-axis).

The medium mesh (figure 28, middle) is similar to the coarse mesh in the open volumes prior to and following the packing but is much more refined within the packing volume and near the wall adjacent to the packing. The mesh is visibly more densely packed in the first half of the packing elements (e.g. 190 – 267 mm, 345 – 423 mm, and 500 – 578 mm). The mesh still coarsens throughout the second half of each packing element as we seen in the coarse mesh. The resulting mesh is still more highly refined than the coarse mesh in these areas. For these reasons, it would be appropriate to think of the medium mesh as being more refined than the coarse mesh within the packing volume and largely equivalent elsewhere.

The fine mesh (figure 28, bottom) is much more refined throughout than either the coarse or medium mesh. There is negligible coarsening as it transitions between the in- or outflow boundaries and the open volume. The volume within the structured packing seems almost uniformly meshed with very few pockets slightly coarser meshing near the end of each packing element. The annular volume between the packing and column wall

is also described by a much finer mesh than in the previous meshes. This mesh could be viewed as an upper limit on the resolution of a mesh with 0.45 mm minimum element sides.

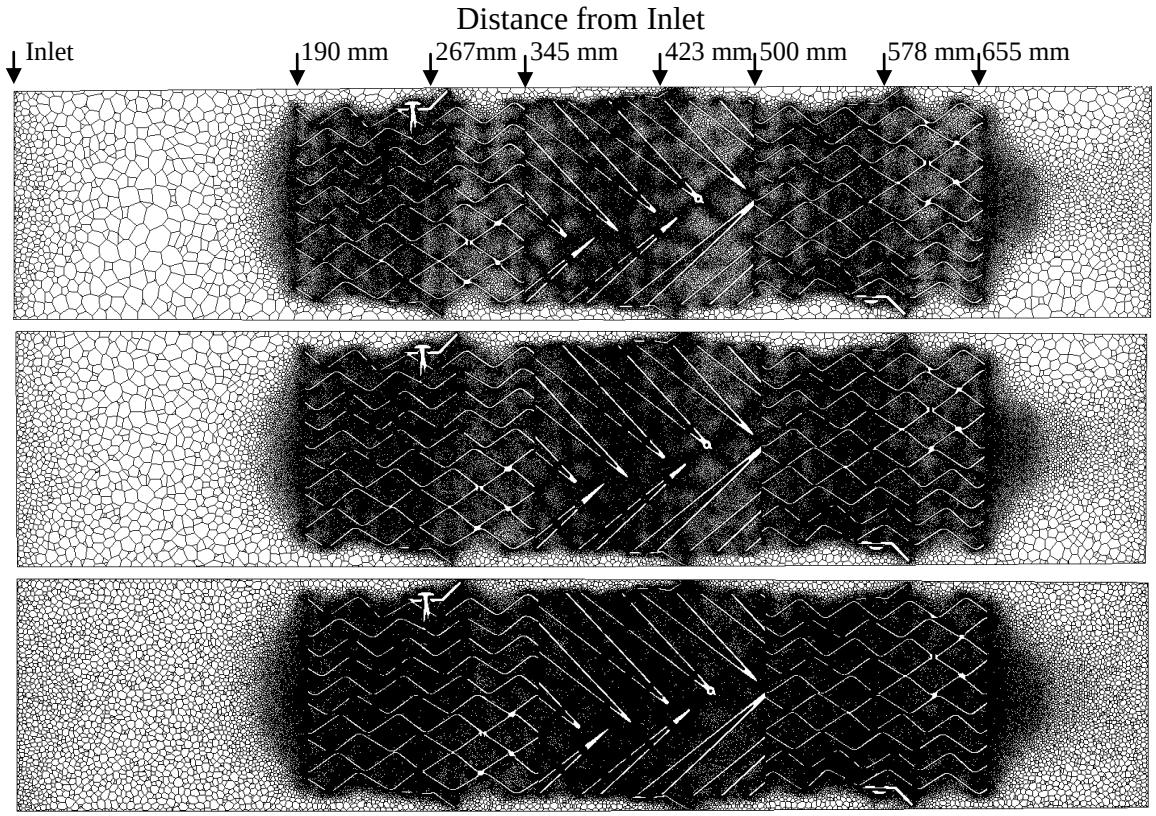


Figure 28: Coarse (top), medium (middle), and fine (bottom) meshes were created to assess the effect of mesh resolution on final solution.

## SCALING

A scaling analysis is critical to any research which utilizes computing clusters. This analysis determines the point of diminishing returns; beyond which increasing the number of processors does not proportionally increase the computation speed. A scaling analysis was performed with the mesh containing 57 million polyhedral elements. Typically, a scaling analysis will begin with a single process or compute node and ratio

all increases to this base case. Unfortunately, the large file size meant the simulation could not be loaded into the available ram on less than 10 nodes (160 processing cores). Therefore, 160 processors were used as a base case and all other results were expressed in ratio to this case.

Increases in processor count typically result in near proportional increases in simulation speed up until the point of diminishing returns. While the average behavior did follow this trend, this scaling analysis revealed two positive deviations at ratios of 2 and 2.8. In the first case, 320 processing cores give a ratio of 2 relative to the base. However, the gains in processing speed prove to be just higher than two times the base case. The second deviation occurs at a ratio of 2.8 or 448 processing cores. This ratio gives a boost in performance resulting in a speed enhancement more than three times that of the base case. Each point beyond this ratio yields significantly decreased speed up returns. Therefore, this mesh would be optimally simulated with 448 processors.

There are issues which might justify running at a point other than the optimal number of processors. Prior to the beginning of CFD calculations, a computing cluster must partition the geometry file so that each processing core "owns" a piece of the simulation. This can be very time consuming with the large mesh files used in this study. Because the total run time per job is limited on the TACC system, it was sometimes necessary to run with an excess of processors in order to complete the job in a single submission instead of requiring multiple job submissions, queues, and partitioning which would decrease computational efficiency.

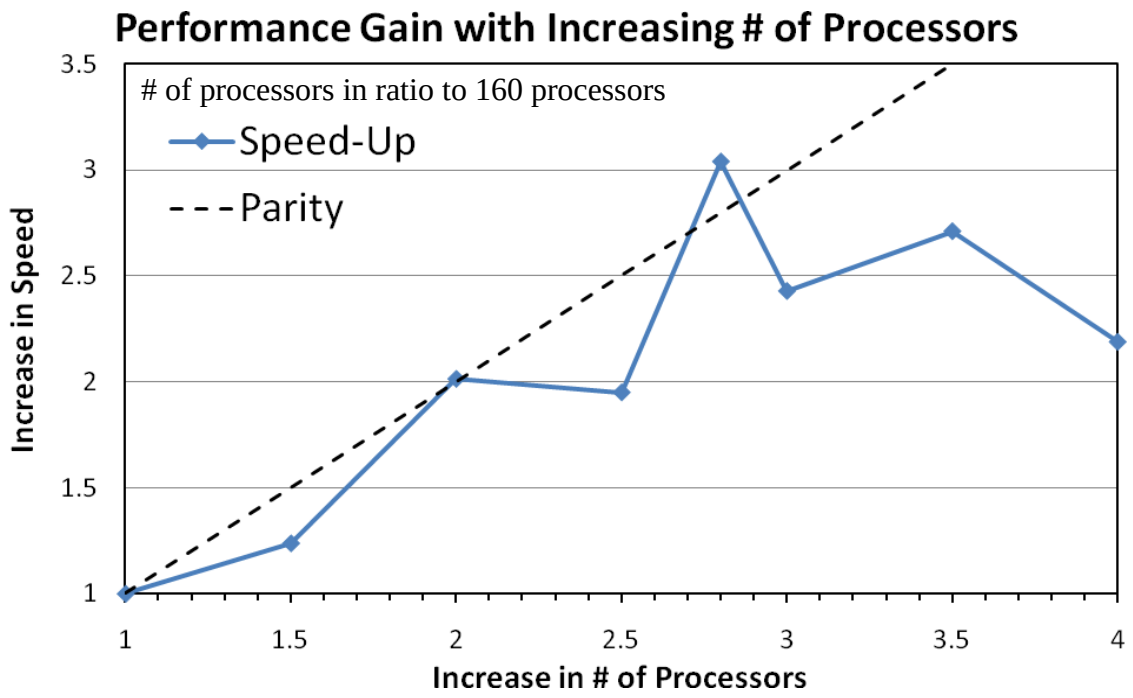


Figure 29: A scaling analysis found 448 processors to be the most efficient use of available hardware.

### GRID SENSITIVITY

A final step in evaluating mesh performance is to conduct simulations with each mesh in order to assess how the mesh resolution affects convergence. Steady state simulations were conducted with each mesh using a coupled solver and two-layer, Realizable k-ε turbulence modeling. Transient simulations were also conducted with the fine mesh in order to test for the presence of any time-variant phenomena which the steady simulations could not capture. These results are presented in figure 30.

All three mesh files converge to the same predicted pressure loss across the packing stack. This is somewhat surprising as the use of subdivided volumes necessarily results in an averaging of the flow phenomena across the chosen volumes. This averaging usually results in small errors which accumulate across the mesh volume.

Therefore, it is expected that more highly refined meshes will yield more accurate answers. This accuracy comes at the expense of computational time as the increased number of cells in fine meshes requires more computations.

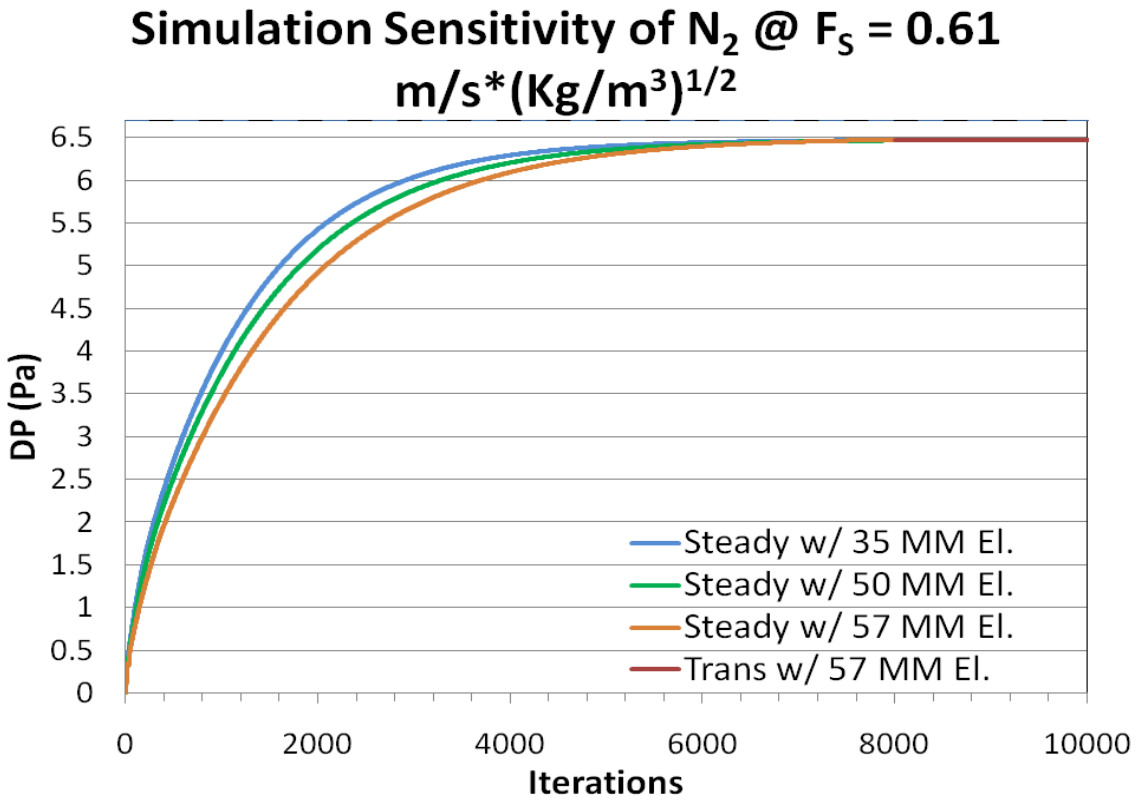


Figure 30: Nitrogen simulations of $F_S$ = 0.61 m/s*(Kg/m$^3$)$^{1/2}$ performed with each mesh file converged to the same value.

The equivalent solutions of the coarse and fine mesh are a pleasant surprise. The smallest mesh typically converged in 2,000 – 4,000 fewer iterations than the largest mesh. This means that analyses for macroscopic variables, like pressure drop, can be calculated very quickly with relatively coarse meshes without sacrificing accuracy. More localized values such as streamlines and velocity vectors might require the higher spatial

accuracy of a more refined mesh. The desire to study such values is the rationale behind using the highly refined mesh throughout this study.

Steady state simulations employ a number of approximations to obtain approximate, time averaged solutions. One such approximation is the use of "local time-steps" which are dynamically adjusted to obtain essentially invariant behavior.[12] Obviously, the use of steady simulations is inappropriate to flows which have periodic boundary conditions or otherwise changing flows. However, unsteady phenomena are sometimes present in steadily imposed flows. An excellent example is the vortex shedding which occurs in flow around a sphere above a critical Reynolds number. The possibility of such behavior requires that a transient simulation be conducted even when a steady flow is expected.

To this end, a transient simulation was performed with the fine mesh using the same turbulence settings as in the steady simulations. Default transient settings were employed for this first approximation analysis. As can be seen in figure 30, the transient simulation did not deviate from the results obtained from the steady simulations. This suggests there are no large scale transient phenomena and that steady simulations should be sufficient to obtain a gross understanding of the prevailing physics in the continuous phase of structured packing. This should not be taken to mean that no transient phenomena occur or that transient simulations would not be useful in analyzing structured packing. There may well be offsetting time-variant phenomena which do not affect macroscopic pressure performance but might prove instrumental in improving local pressure dissipation or, in the long run, mass transfer.

Investigating this possibility would require a great deal of trial and error in order to optimize the transient constants and choice of time step. The goal of this work was to obtain a macroscopic picture of flow through structured packing which is at cross

purposes to the identification and modeling of transient phenomena which do not seem to affect overall pressure performance. Therefore, time-variant investigations were not pursued further.

The mesh evaluations described above were performed using simulation of nitrogen at a relatively low flow rate. An expedited test using only steady simulations with the coarse and fine meshes was performed at a higher flow rate (2.44 $m/s*[Kg/m^3]^{1/2}$) with water as the fluid (see figure 31). Once again, both simulations converged to the same value. This is strongly suggestive that relatively coarse adaptive meshing can be used to study the overall performance of bulk phase flow through structured packing.

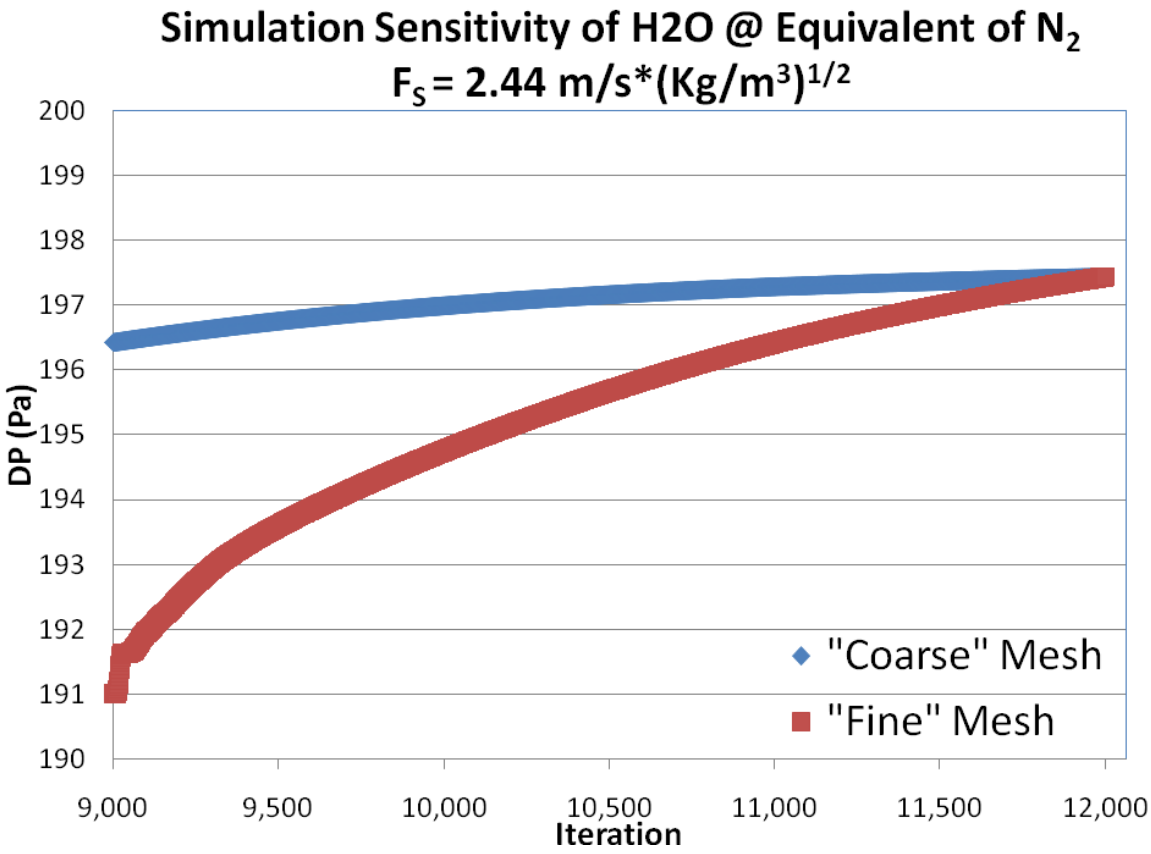


Figure 31: Water simulations of flow at $F_S$ = 2.44 m/s*(Kg/m$^3$)$^{1/2}$ performed with the coarse and fine meshes converged to the same value.

## TURBULENCE MODELING

The evaluation and selection of appropriate turbulence models is also of great importance when conducting CFD simulations. Therefore, the performance of the k-ε model, k-ω model, and RSM are compared in figure 32. The solution was initialized by assuming a uniform velocity field and then solved with a steady state, two-layer, realizable k-ε turbulence model. As can be seen in the figure, computations were allowed to run until well past a steady solution. The k-ε model converged at a value approximately 9 percent below the experimentally predicted value. This solution was then used as the starting point for the k-ω model. The predicted pressure drop began

falling immediately upon switching the turbulence model. The simulation was stopped after the predicted pressure drop fell 4 percent below the already inaccurately low prediction of the k-ε model. This procedure was then repeated with the RSM.

As shown in figure 32, the predicted pressure drop spiked sharply. The simulation crashed after only 96 additional iterations. The RSM is a very complex calculation with many more constants than the two-equation models previously mentioned. Therefore, the RSM was restarted from the converged k-ε solution without the effect of gravity and with the energy equation turned off under the belief that a simpler calculation might prove more stable. Surprisingly, the RSM crashed after only 10 iterations with these parameters removed (not shown).

As mentioned, the RSM is a very complicated model. The observed instability is likely a result of attempts to use the default parameters to simulate flow through a very complicated geometry. Clearly, the default parameters are not suitable for simulation of flow through the studied structured packing. However, finding the correct combination of so many parameters is likely to be a time-consuming undertaking. By comparison, the robust nature of the two-equation models means they will nearly always converge. The parameters can then be fine tuned to improve the accuracy. As will be shown below, the k-ε model proved to be highly accurate. Therefore, the RSM can only marginally improve the results and it was decided that the effort would be better spent analyzing the results of simulations conducted with the two-equation model.

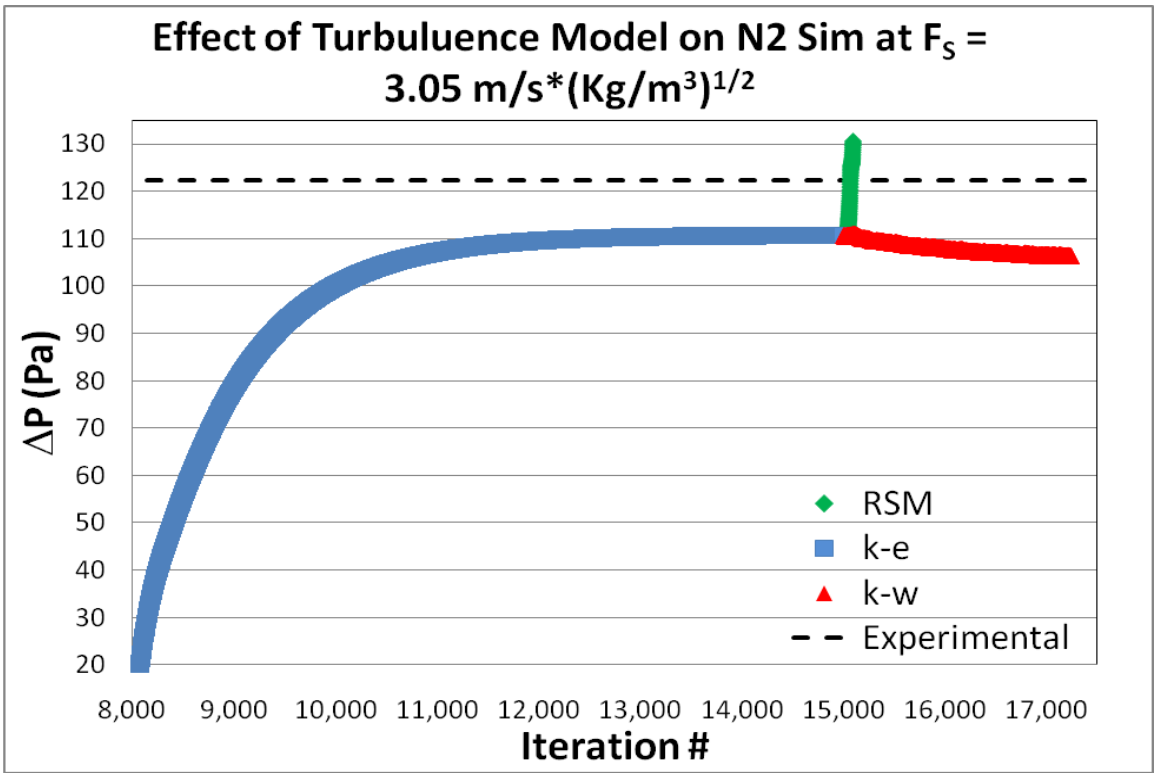


Figure 32: A comparison of the performance of different turbulence models.

## NITROGEN SIMULATION

The bulk of the simulations were carried out with the two-layer, Realizable k-ε model. As shown in figure 33, the simulation predictions compare favorably with experimental results. On average, the simulations predict a pressure drop 7.5 percent below the measured value. Accuracy is highest at the lowest flow rate which predicted a pressure loss only 3.7 percent lower than experimental results. Error increases with increasing flow. When correlations are extrapolated to an $F_S$ of 3.66 m/s*(Kg/m$^3$)$^{1/2}$, the simulation correlation predicts pressure loss which is 10.3 percent lower than the experimental correlation.

As was noted above, the inaccurate column diameter used in the simulations is likely contributing to the under prediction of pressure loss by CFD simulation. However,

the fact that the wiper bands do represent a periodic barrier to wall flow means that the bypass flow is limited to regions between the wiper bands. The high accuracy can be attributed to the wiper bands somewhat negating the effects of the increased annular area. It is not unreasonable to assume that repeated simulation with an accurate column diameter would prove even more accurate.

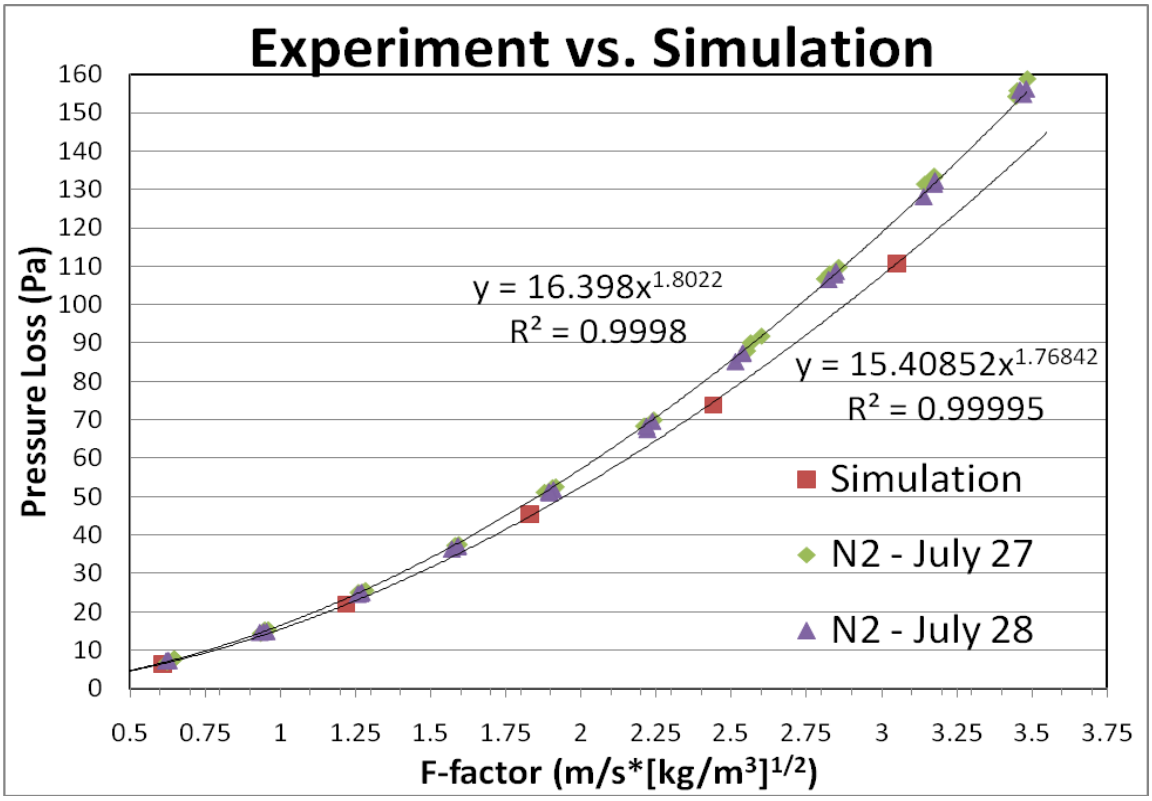


Figure 33: A comparison of experimental and simulation predictions of pressure drop.

Among the goals of this project is the increased acceptance and application of CFD simulations for analysis and design of distillation contacting media. Therefore, the experimental and simulation results were compared to the Stichlmair model for calculating dry pressure loss through structured packing. The Stichlmair model calculates dry pressure loss as a function of void fraction, Reynolds number, fluid

density, and packing specific constants. The specific formulation is given in equation 11 - equation 14 below and the Mellapak N250Y specific parameters are provided in table 11.

$$d_p = \frac{6(1-\varepsilon)}{a} \quad \text{Equation 11}$$

$$\mathrm{Re}_g = \frac{d_p V_g \rho_g}{\mu_g} \quad \text{Equation 12}$$

$$f_o = \frac{C_1}{\mathrm{Re}_g} + \frac{C_2}{\mathrm{Re}_g^{1/2}} + C_3 \quad \text{Equation 13}$$

$$\Delta P_{Dry} = \frac{3}{4} f_o \left(\frac{1-\varepsilon}{\varepsilon^{4.65}}\right) \rho_g \left(\frac{Z}{d_P}\right) V_g^2 \quad \text{Equation 14}$$

Table 11: The Stichlmair parameters for "plastic Mellapak 250Y" structured packing.[29]

| | |
|---|---|
| a ($m^2/m^3$) | 250 |
| ε | 0.85 |
| $C_1$ | 1 |
| $C_2$ | 3 |
| $C_3$ | 0.35 |

The given Stichlmair parameters list the void fraction (ε) of at 85 percent. This contradicts previous research which used X-ray CT to measure the void fraction of Mellapak N250Y in a 146 mm column and found it to be 91.6 percent.[21] However, even that value is inaccurate to describe Mellapak N250Y in a column with the simulation diameter of 159 mm. As a correction, the packing volume was calculated from Owens *et al.* and used as the occupied volume in the simulation geometry. Combining this with the

simulation diameter allowed the calculation of the simulation void fraction. This value was calculated to be 92.9 percent. The measured and simulated pressure drops are presented alongside the Stichlmair predictions in figure 34. The error relative to experiment is shown figure 35 for both the simulation and Stichlmair predictions.

Overall, the simulation is more accurate than either the uncorrected ($\varepsilon = 0.85$) and both corrected ($\varepsilon = 0.916$, $\varepsilon = 0.929$) Stichlmair models which give an average error of 15.6, 12.7 and 16.2 percent, respectively. With the exception of one point, the simulation predictions show less error than either the uncorrected or corrected Stichlmair models. The simulation also more accurately conveys the nature of the response to increasing flow rates. It is interesting to note that the uncorrected Stichlmair model actually outperforms both corrected models.

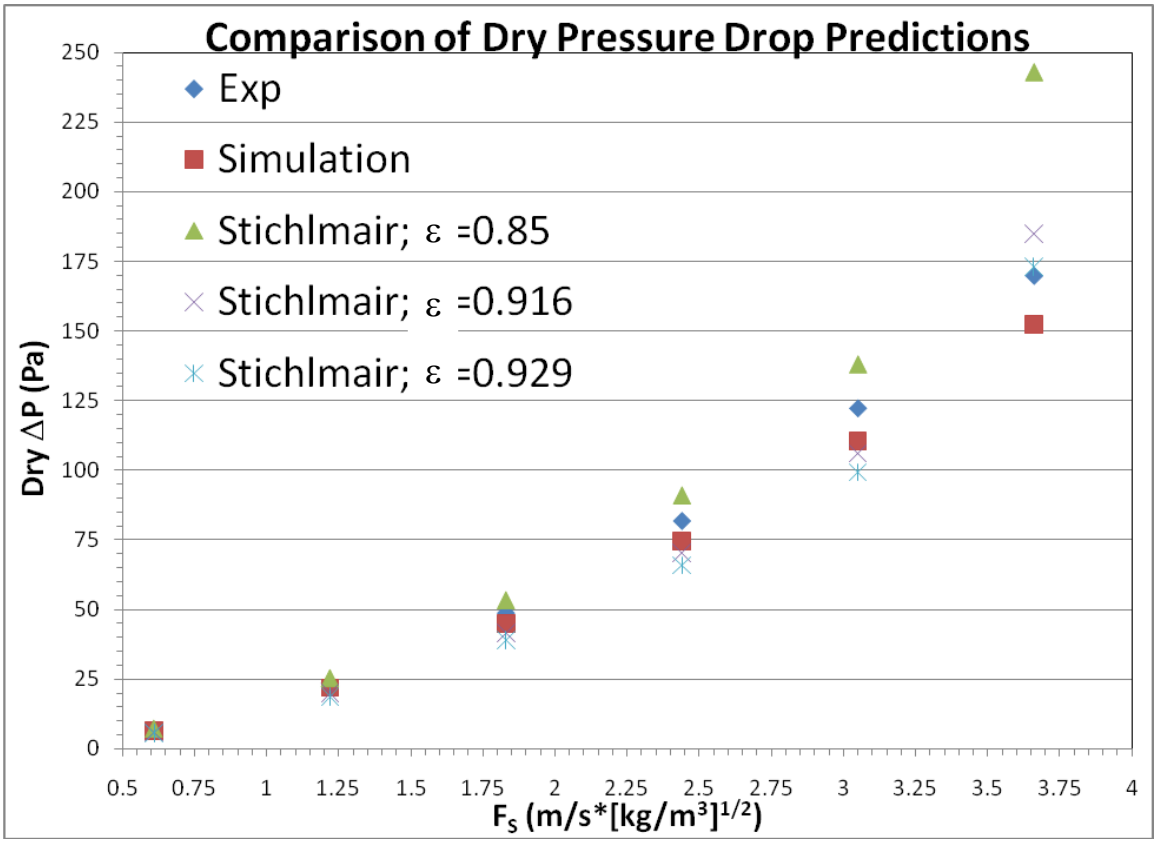


Figure 34: Dry pressure drop prediction comparison.

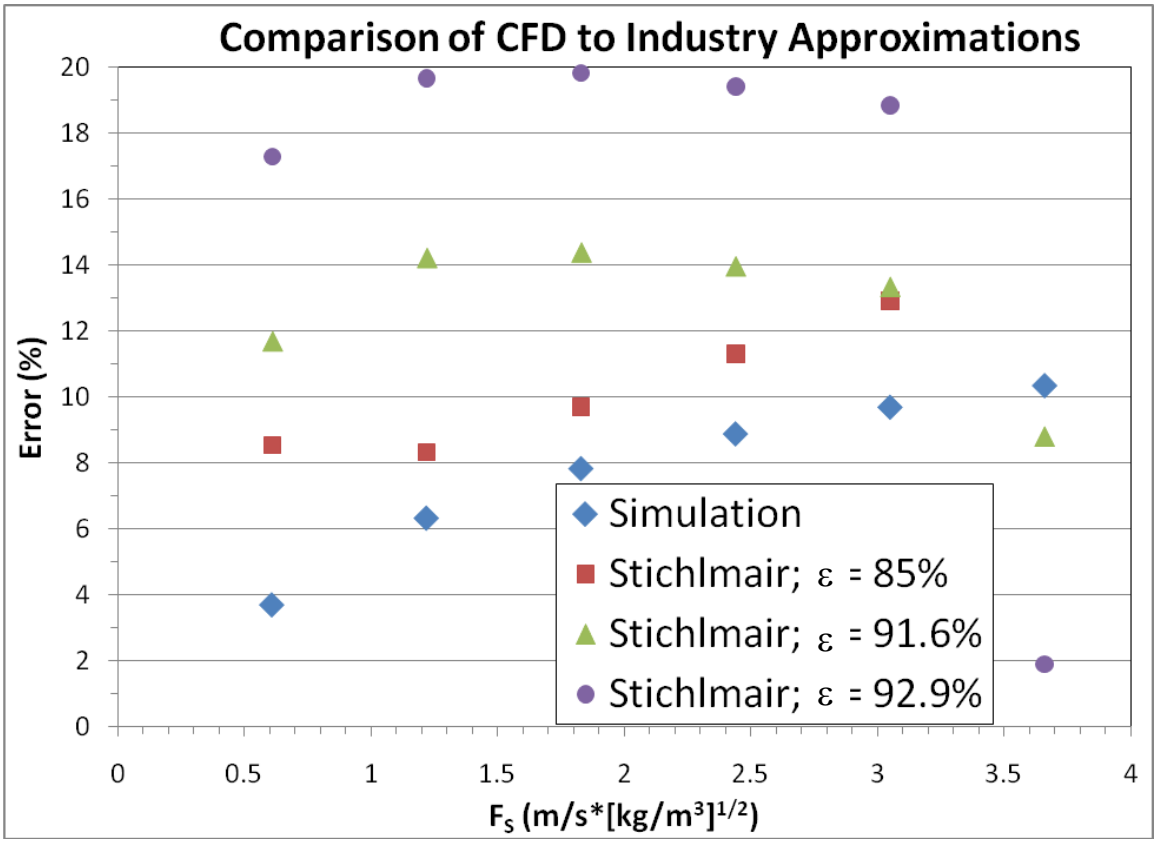


Figure 35: The error of various Dry ΔP predictions.

## DIAGNOSTIC ANALYSIS

The immense volume of data generated by CFD simulation is one of the many benefits of this method of study over traditional experimentation. Each quantity present in the RANS is available at each point in the volume and surface meshes. These values are given to a high precision without the need for expensive, complicated, or intrusive instrumentation. Moreover, the geometry of study does not need to be modified to include data gathering devices.

Consider figure 36 as an example. This figure shows the minimum and maximum Z-magnitude velocities in planes perpendicular to the column axis at distances of 12.7, 25.4, and 38.1 mm up and downstream of the beginning of the packing, each packing

joint, and the end of the packing stack as well as planes at the center of the wiper bands in each element. This enables a very thorough analysis of how the velocity distribution reacts as it travels through each subset of the packing volume.

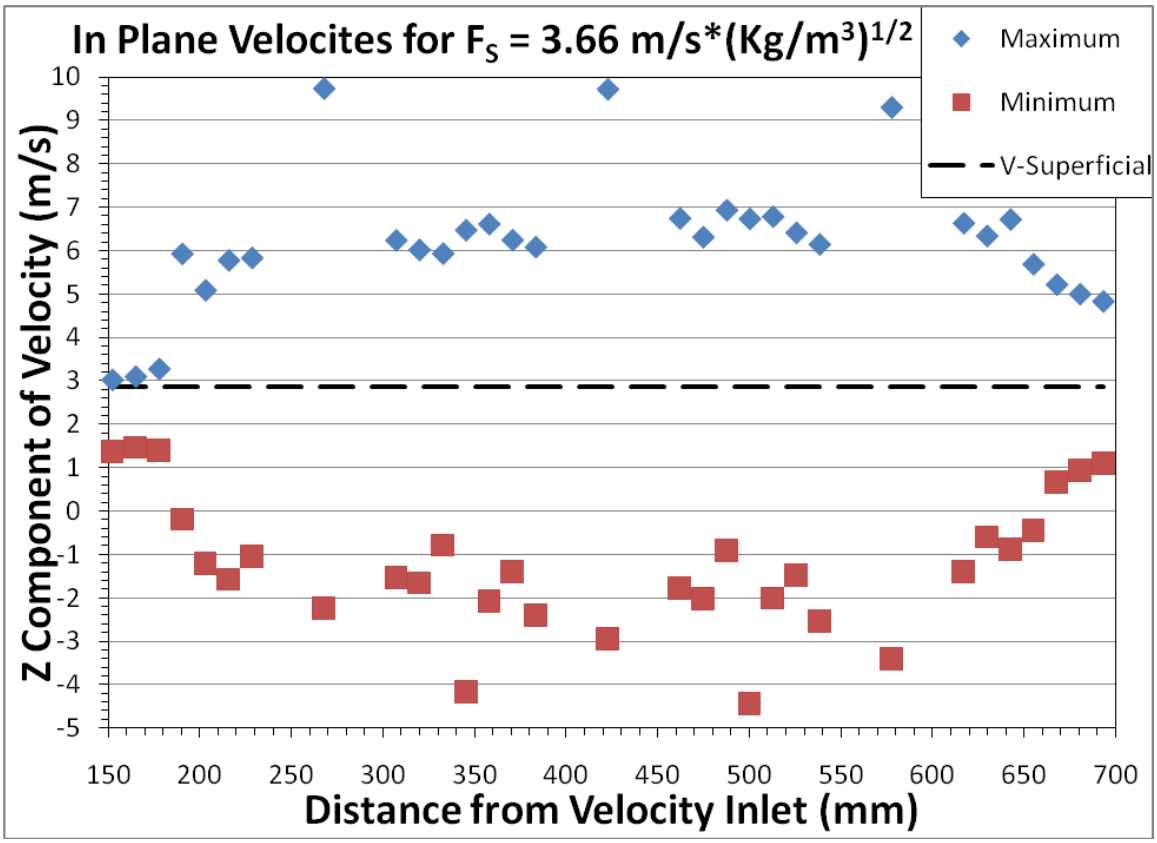


Figure 36: In plane velocities calculated from the highest nitrogen flow rate. Wiper bands are located at 268, 423, and 578 mm from the inlet, joints are at 345 and 500 mm and the packing begins and ends at 190 mm and 655 mm respectively.

Prior to entering the packing (150 – 190 mm), the velocity distribution is very narrow and the minimum velocity is positive. Negative velocities are observed immediately after entering the packing. The maximum velocity necessarily increases as the average velocity at any elevation must equal the superficial velocity. The wiper bands occlude the annular area and reduce the available cross-sectional area (CSA). The

reduced CSA requires that the linear velocity increase. This effect can be seen 268, 423, and 578 mm. The joints produce the opposite response. The magnitude of negative flow jumps dramatically at each joint (345 and 500 mm). Negative flows are no longer observed once the flow leaves the packing (655 mm); however, the velocity distribution is still larger than prior to entering the packing.

This general procedure was repeated for the area-weighted-average (AWA) pressure in the same planes, with the exception of the wiper bands. This data is present in figure 37. The AWA pressure information proves informative as to how and where pressure is lost in within the packing. Minimal pressure drop is observed prior to entering the packing. Due to increased surface area and skin drag, the pressure begins to drop rapidly but smoothly as the flow progresses through the packing. In fact, the pressure drop appears linear with progression along the length of the column for most of the packing. This linear relationship holds true above and below the packing joint, but fails across the joint itself.

Taking the highest flow rate as an example, if a line were drawn through the three points above the joint and projected beyond the joint it would predict a pressure higher than observed. This shows that the joint causes a step down in pressure as flow proceeds past it. In quantitative terms, the 12.4 mm above and below each joint accounts for 10 percent of the packing length. However, this region contributes 12.6 percent of the pressure loss in the highest flow simulation.

The joint's disproportionately high contribution to pressure drop was also observed experimentally. The pressure loss as a function of flow rate was measured through 610 mm of packed height using first half elements (3 joints per 610 mm height) and then whole elements (1 joint per 610 mm height). The addition of two joints resulted in noticeably higher pressure loss. This result is shown in figure 38.

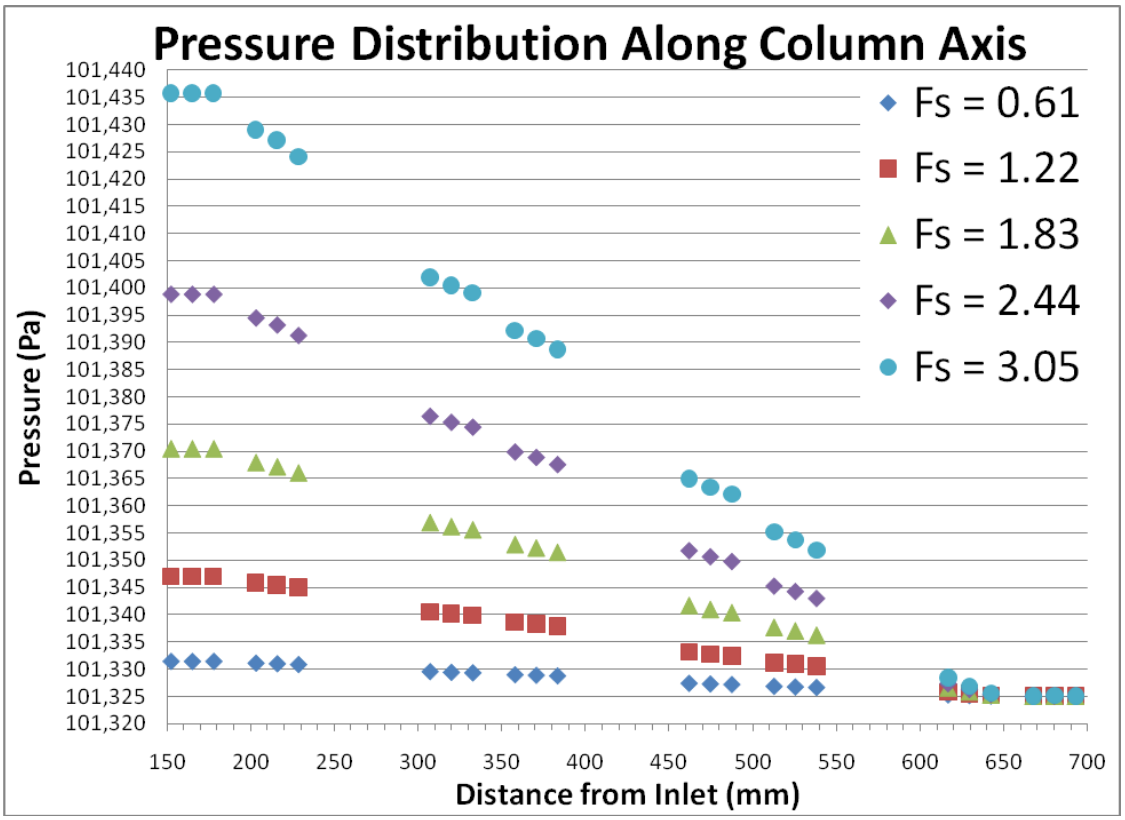


Figure 37: In plane area-weighted-average pressure calcualted at various heights. Wiper bands are located at 268, 423, and 578 mm from the inlet, joints are at 345 and 500 mm and the packing begins and ends at 190 mm and 655 mm respectively.

While it might be argued that the additional pressure demonstrated in figure 37 and figure 38 is negligible, these results must be viewed in the context of the distillation industry. These results specifically address single phase flow whereas distillation is a two-phase operation. Research conducted by Green *et al.* documented increased liquid hold up at and just above the joints in a two-phase contacting column using Mellapak M250Y.[19] This increase in liquid volume will consequently reduce the CSA available for gas phase flow and will exacerbate the poor pressure performance at the joint discussed above. These results can be further combined with work by Owens *et al.* which observed large scale recirculation and stagnation in bulk phase flows at the packing joint. All of

these observations suggest that the joints contribute disproportionately to pressure loss and promote back mixing or fluid stagnation which is counterproductive to mass transfer.

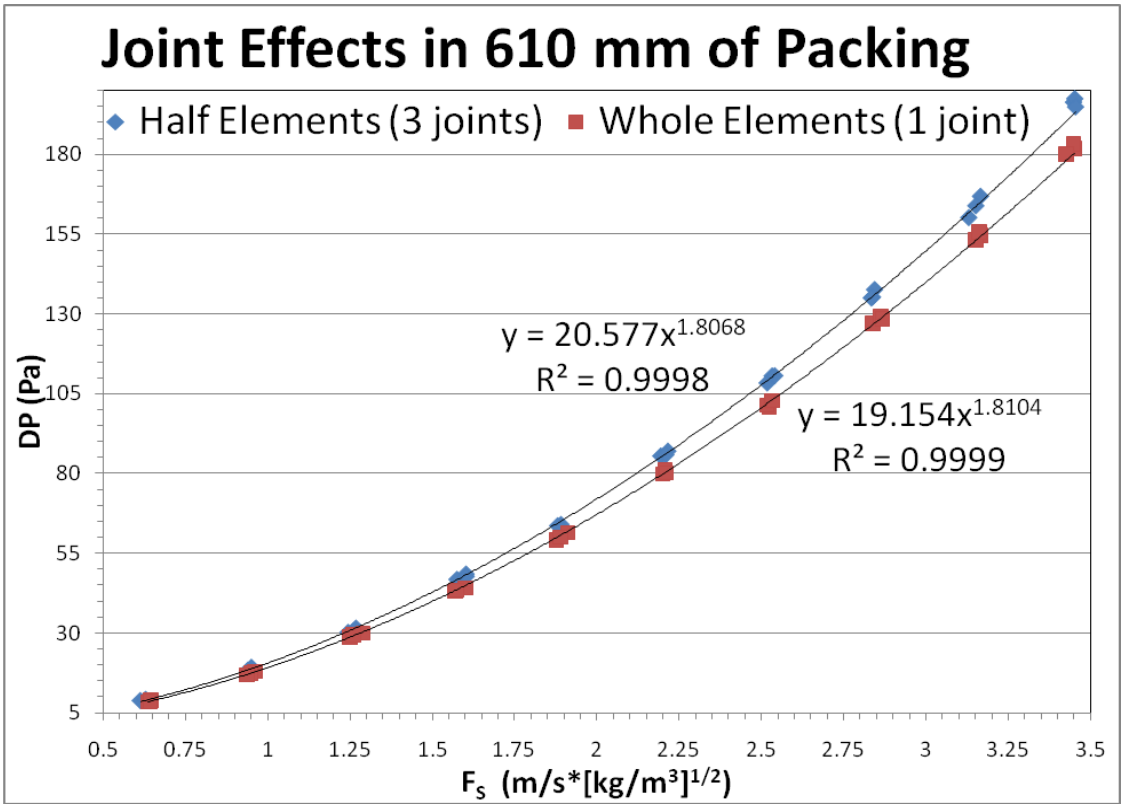


Figure 38: The effect of joints on pressure loss.

CFD simulations also enable researchers to visualize the path fluid takes via the use of streamlines. An example is shown in figure 39. The streamlines are colored by velocity magnitude. Several regions blue regions with sparse streamlines are visible. In most of these regions the streamlines turn and point down the column. This denotes negative flow (in the direction of gravity). Two areas are highlighted and shown in detail.

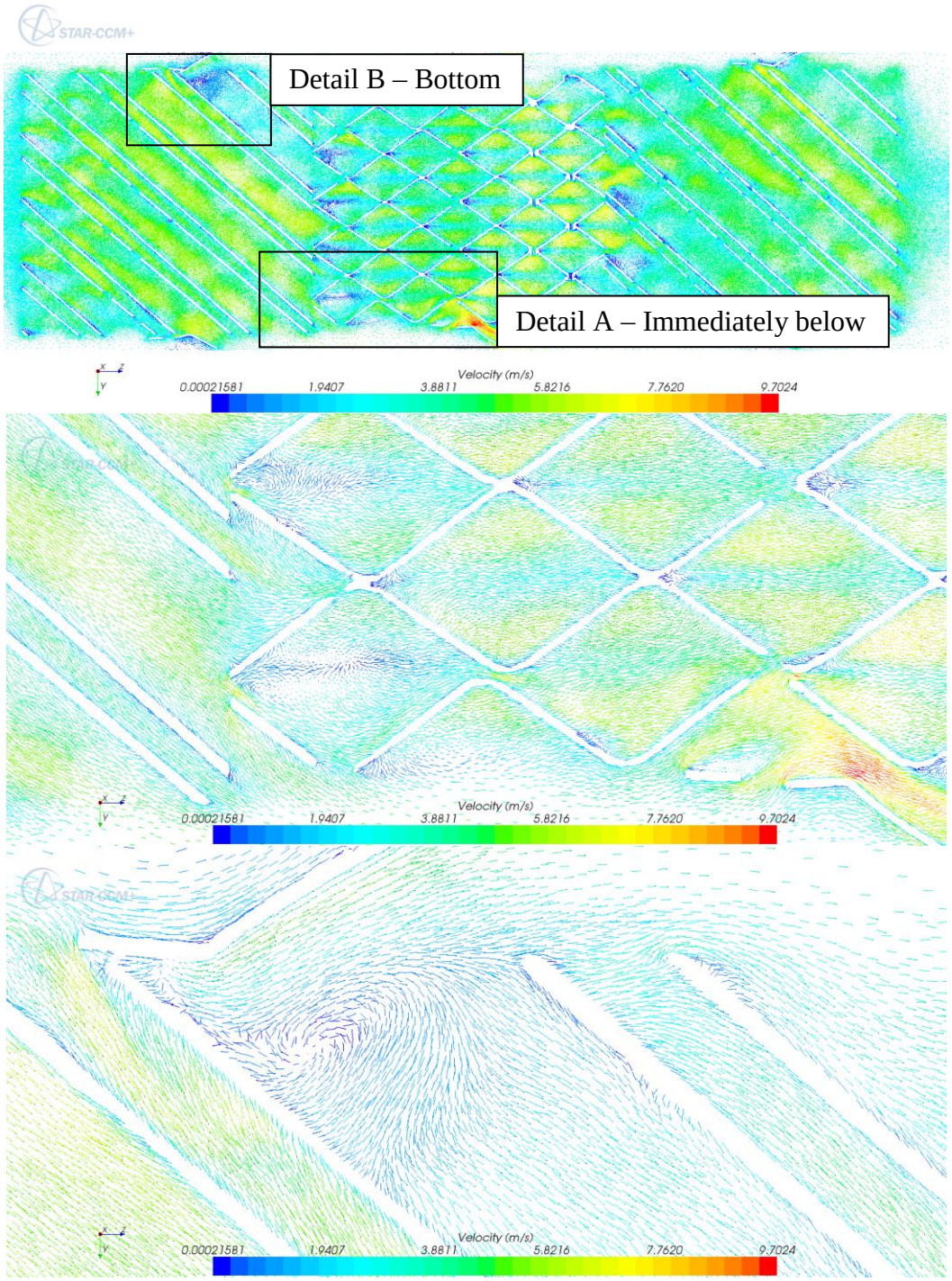


Figure 39: Streamlines are shown in a bisected plane through the packing and in details for clarity.

Detail A depicts a region at and just downstream from the first joint. Two recirculation zones are visible in between adjacent packing sheets. These zones likely stem from separation points created by flow from the lower element over the edge of a channel at the base of the second packing element. The second detail (B) shows flow near the wiper band of the first packing element. No separation point is clearly visible. It is possible that the separation point is not contained in the excerpted plane but the recirculation zone flows into it. However, it is also likely that the complexity of the flow near the wiper band is creating a recirculation zone to dissipate the energy created by wall flow and adjacent channels colliding. The prediction of recirculation zones is in agreement with prior work performed by Owens *et al*.[21] These predictions also confirm that the recirculation occurs over a sustained interval of time as they were resolved by steady state simulations.

Contour plots were also used to investigate the local variation in column performance. Two contour plots are show in figure 40. The figure at left depicts the z-component velocity 13 mm above the middle joint under an imposed flow of .61 $m/s*(Kg/m^3)^{1/2}$. This plot vividly illustrates the non-uniform velocities found throughout the structured packing volume. A large distribution of velocities would result in highly variable residence times for different flow paths through the structured packing. This variation would hinder column performance as some flow paths would have to little contact time and area to accomplish the requisite mass transfer while some flow paths could reach equilibrium which eliminates the mass transfer driving force and limits overall mass transfer. This same figure also shows that there are many instances of negative flow in between and near to the packing surface. Negative flow corresponds to back mixing. This behavior would actually result in product being reduced in purity.

The figure at right shows the z-component velocity 38 mm beyond the end of the packing stack for a flow of 3.66 m/s*(Kg/m$^3$)$^{1/2}$. A wide velocity distribution is still plainly evident well beyond the end of the packing stack. Large positive deviations from the superficial velocity are present at the column wall while lower velocities are present near the center of the column. This flow pattern would encourage liquid to flow towards the center of the column and could result in channeling.

It is also worth noting that the velocity distribution directly corresponds to the pressure distribution. This means the pressure also varies around the perimeter of the column. Pressure readings could be strongly affected by choice of pressure sensor placement.

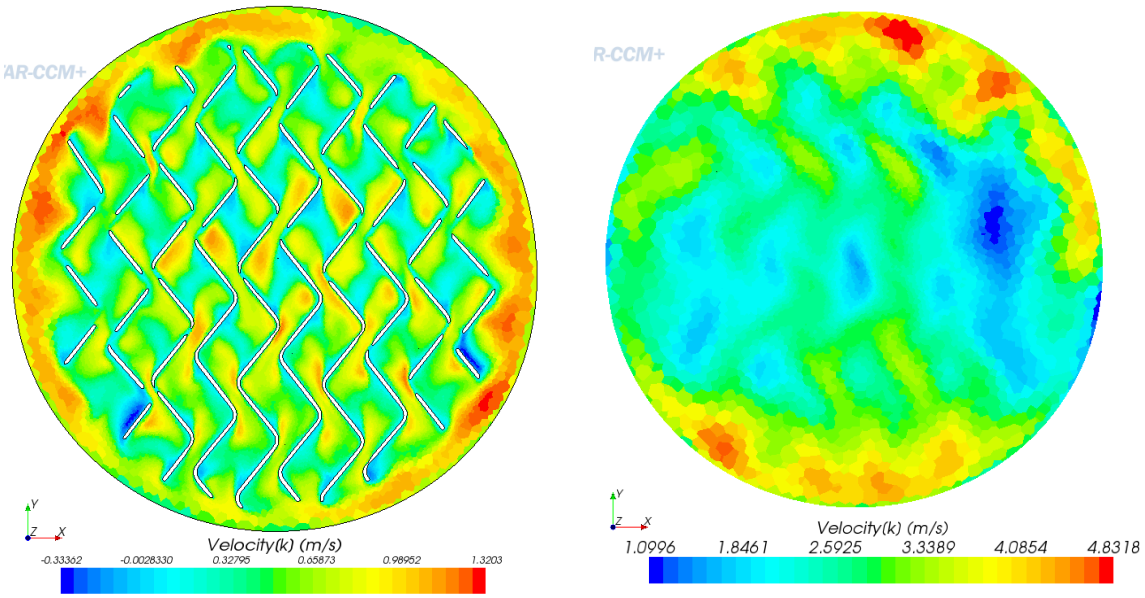


Figure 40: Contour plots of z-component velocity are shown at an elevation 13 mm above the second joint for a flow of 0.61 m/s*(Kg/m$^3$)$^{1/2}$ (left) and 38 mm beyond the final packing element for a flow of 3.66 m/s*(Kg/m$^3$)$^{1/2}$.

## WATER SIMULATION

Simulation and experimental campaigns were also conducted using water as the bulk phase in the hopes of evaluating the use of similarity theory to generalize results across multiple fluids and phases. The simulation and experimental results are shown in figure 41. The simulation drastically under predicts the pressure loss of water flow when compared to the water phase experimental results. The increased error of the water simulations when compared to the nitrogen simulations suggests there is some aspect of the water experiments which are not being adequately captured in the simulations and, furthermore, that this is not present in the nitrogen experiments.

Unfortunately, there are several possible causes for this discrepancy. As noted in the Experimental Method section, a grate was used as packing support in the initial experiments. This grate was replaced in the nitrogen experiments but could not be eliminated from the water experimental procedure. This grate represents a constriction of the column diameter, increased surface drag, and the creation of separation points which would dissipate pressure. This would be expected to result in a higher experimental pressure drop relative to the simulation which does not have the additional flow disruption.

The larger diameter of the simulation geometry is another probable cause of error. The volume occupied by the packing is the same in both the experiment and the simulation. However, the larger diameter of the simulation geometry results in a larger void fraction. Pressure drop is varies inversely with pressure drop and therefore it is expected that the higher void fraction geometry of the simulation would result in lower pressure drop than the experiment. The uncertainty as to the relative magnitude of the geometrical inaccuracies underscores the need for rigorous attention to detail when constructing CFD geometry.

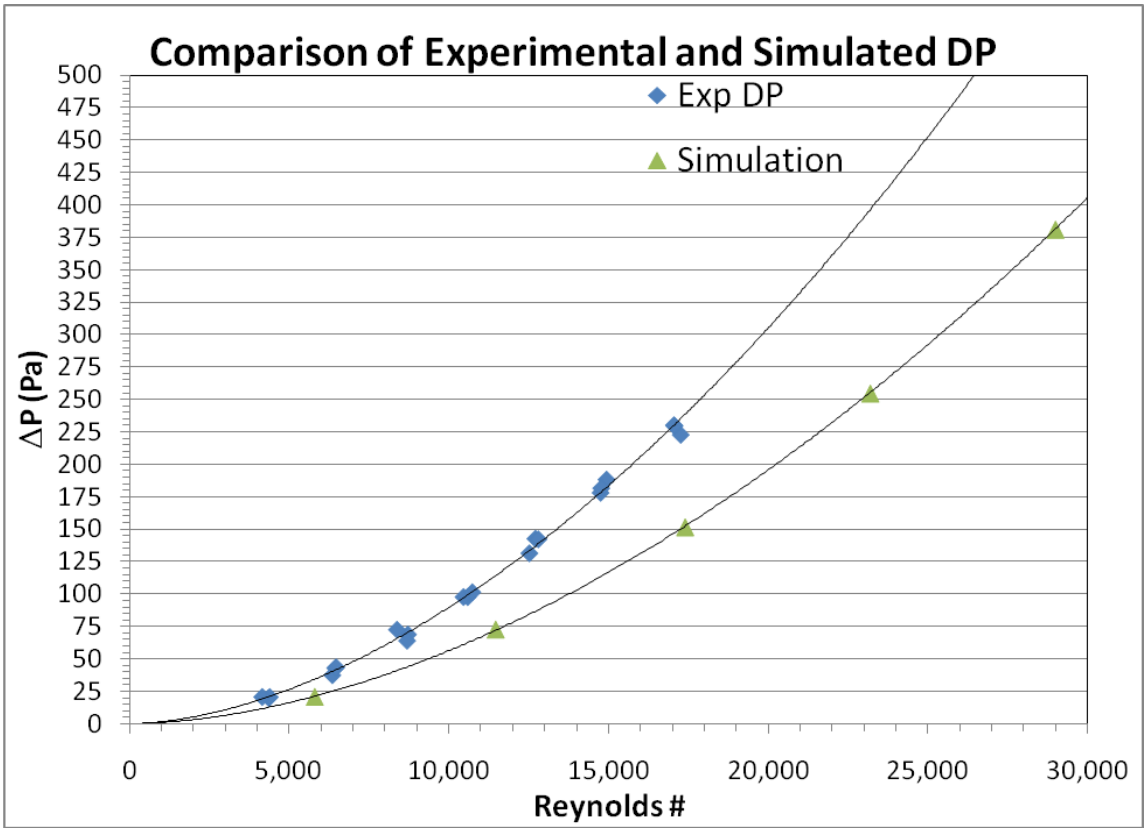


Figure 41: Comparison of the water experiments and simulation.

The need to recycle the water throughout the experimental system is another aspect which is not captured by the simulation method. The pump dissipated waste heat into to the water. The relatively small heat exchanger employed in the experiments did not entirely eliminate variation in the process fluid (water) temperature. Instead, the water was allowed to reach a thermal steady-state before data was recorded. Therefore, the viscosity and density were slightly different at each flow rate. By contrast, the simulation employed a single fluid temperature for all runs.

All simulation and experimental data were compared in non-dimensional terms to compensate for the varying fluid properties. The results of this comparison are shown in figure 42. The non-dimensional data collapses to a single trend and shows strong

agreement between both simulation and experimental results irrespective of fluid phase. This suggests that variation in fluid properties could well be the source of the error when the water experiments and simulation are compared using only pressure drop and F-factor. The effects of density are not accounted for in a balanced manner while the viscosity is ignored completely. Repeated simulation using a higher fluid temperature might result in better agreement with the experimental results. The agreement of the non-dimensional data suggests similarity theory can be used to generalize results so long as identical geometries are employed.

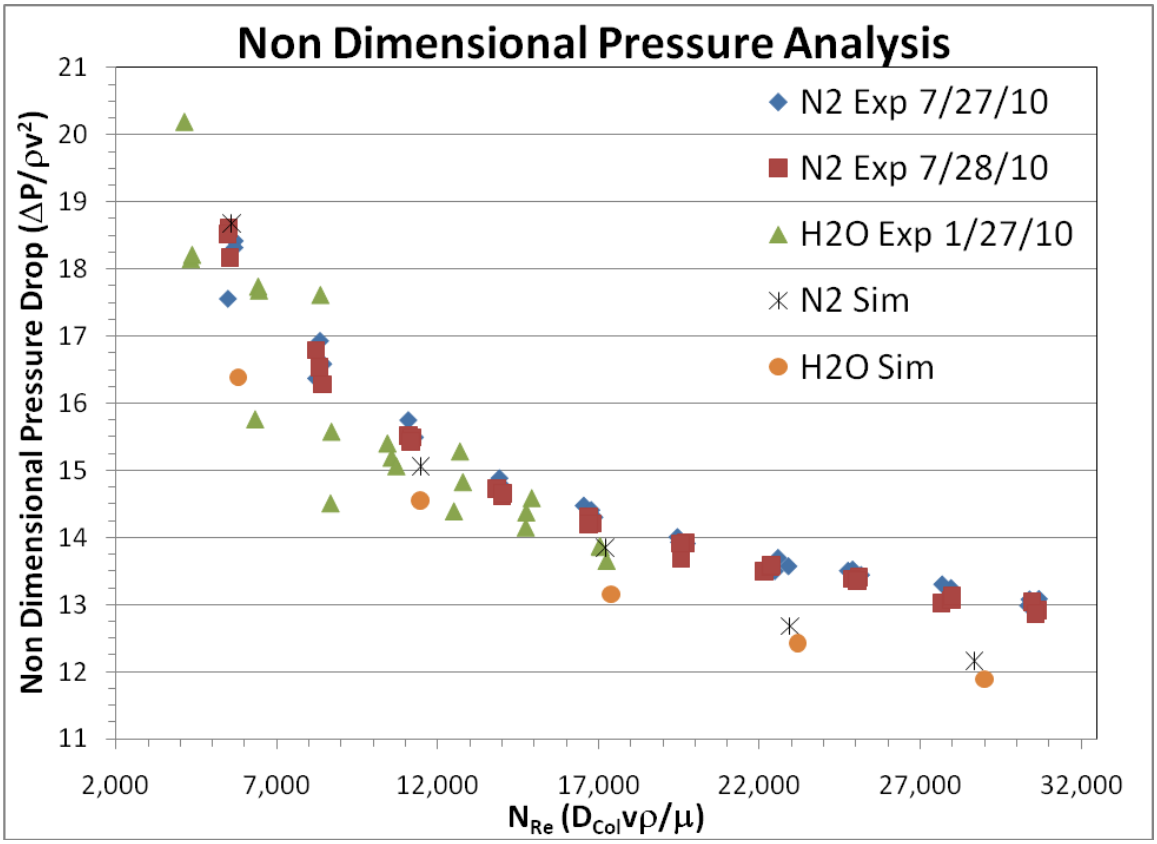


Figure 42: Non-dimensional analysis of all the data.

# Chapter 6: Conclusions

A unique confluence of resources and expertise permitted an innovative and expansive analysis of structured packing. With the help of the UTCT lab, X-ray CT scanning was shown to be superior to traditional CAD as a means to initialize packing geometries for CFD analysis. The TACC clusters enabled the creation of grid files with a resolution finer than what has been employed in the literature thus far. The significant computational resources available through TACC permitted the direct simulation of a larger and more complicated geometry than has been presented in the literature. The relatively short simulation obtained with massively parallel computing permitted a more expansive study as well.

## SUMMARY

Simulation with a k-ε turbulence model is capable of predicting nitrogen dry pressure loss with less than 10 percent error throughout the range of common distillation vapor rates through 250Y series packings. CFD simulations provide a wealth of data not readily accessible via traditional experimental methods. The computation and display of streamlines enables researchers to quickly determine the regions of packing which exhibit poor flow performance. The use of contour plots enables an analysis of local variation in packing performance. Identifying the cause of such variation is critical to the improvement of distillation design, operation, and control.

These capabilities open the door to focused improvement of structured packing design. The unique data obtained from CFD simulations will enhance current understanding of distillation flow physics and provide a powerful diagnostic tool. Identifying specific causes of performance deficiencies will eliminate the need for extensive and expensive prototyping. Instead, potential improvements can be

implemented to the CFD geometry and the resulting effect evaluated via flow simulations. This procedure will increase the gains made in each new model design and decrease the cycle time required to bring new designs to market.

## GEOMETRY GENERATION

CT scanning was shown to be a powerful and expeditious alternative to the traditional computer aided drafting (CAD) method of geometry generation. The use of CT scans permitted generation of the base geometry in just over seven hours; far less than the multiple weeks quoted for creation of a comparable CAD based geometry. This time could be reduced to mere minutes if a cone-beam and area detector were employed for the scan. The expense incurred in obtaining the CT scan was also much less than would have been required to contract for the work of a CAD technician.

Scan based geometry generation exceeds CAD in its ability to quantify resolution. The CT based geometry provides fidelity equal to the minimum resolution of the scanner used. This is in sharp contrast to CAD which relies on assumptions as to "relevant features" of the geometry or on the ability of the technician to accurately represent fine or complicated details. Therefore, CT based geometry generation is preferable to CAD for complicated and irregular geometries.

This work did encounter an inaccuracy in the final geometry. However, this was due to improper pre-scan preparation and was not attributable to the scanning procedure itself. The error did serve to highlight the ability to modify attributes of the CFD geometry to improve the accuracy of simulations. CT geometry generation can be used to compensate for some of the inherent inaccuracies in studies employing lab scale equipment.

Stereo Lithography (STL) files proved to be an excellent choice for conveying intermediary data between programs or protocols. The non-proprietary format allows any

vendor to include read/write support and the triangulated nature of the data makes it a natural choice to described surfaces prior to the final polyhedral meshing. A file size of less than 500 MB was required to store and transport high fidelity, unsimplified scan data. This is a very manageable size and was transferred across multiple networks between the various computer systems with ease.

**MESHING**

The convoluted and overlapping nature of structured packing represents a significant hurdle to the application of CFD scans. However, the use of adaptive meshing resulted in extremely high quality mesh files for a variety of mesh growth rates and densities. The meshing algorithm employed here was very efficient; requiring less than thirty hours to generate highly refined surface and tetrahedral meshes as well as convert them to the polyhedral equivalent. The prodigious meshes did require a large amount of physical memory (128 GB < memory < 256 GB) for generation and conversion.

Adaptive meshing is extremely well suited to and beneficial in the simulation of structured packing. The complexity of packing geometry almost precludes the manual generation of a high quality volume mesh. However, the decreased turn-around time required with adaptive meshing and permits a more exhaustive study of various mesh parameters than can be achieved through manually specifying and improving a mesh. The ability to customize iterative mesh improvement algorithms makes full use of the power of high performance computing and results in drastically improved mesh quality without requiring constant interaction by the researcher.

The use of polyhedral meshing resulted in mesh files with 80 percent less cells than a comparable tetrahedral volume mesh. This in turn yielded mesh files between 18 and 27 GB in size as opposed to the expected tetrahedral mesh size of 300+ GB. The polyhedral meshes displayed exceedingly high mesh quality as judged by both volume

change and face quality metrics. This suggests the polyhedral elements are able to efficiently conform to the complicated channels and surface intersections which make up structured packing. Polyhedral meshing is ideal for the study of structured packing due to the combination of reduced file size when studying expansive geometries and their ability to conform to packing surfaces without reducing mesh quality or computational stability.

CFD predictions of single phase pressure drop were shown to be independent of the mesh densities and cell growth rates employed in this study. This was confirmed with multiple fluids and at multiple flow rates. From this it can be confirmed that relatively coarse grids and high mesh growth rates are sufficient to model single-phase regions of the bulk-flow through structured packing. This will be especially important for two-phase simulations which will require highly refined near wall meshes to resolve the thin film liquid flow along the surface. The increased computational complexity of the near wall region can be offset somewhat through the utilization of relatively large cell growth rates and coarse meshes in the vapor filled channels.

**SIMULATION**

A scaling analysis found 448 processors to be the most efficient use of resources to simulate a polyhedral mesh with 57 million volume elements. The use of more than 448 processors resulted in decreased computational speed relative to the increase in processor usage. 160 and 320 were also found to be relatively efficient choices though not equal to the optimum at 448 processors.

The k-ε turbulence model outperformed both the RSM and an analogous k-ω model when computing a constant density, coupled flow, and coupled energy simulation with gravity effects. The k-ω model predicted a pressure loss more than 4 percent lower than the k-ε model. The RSM did not converge when run with the same simulation

settings. Running the RSM simulation without the gravitational force and energy equation was also unstable. This sensitivity and long computation times makes the RSM ill-suited for extensive use in modeling structured packing. Moreover, the high accuracy and available customization of the two equation models largely negates the need for and any potential benefit from more complicated models. The k-ε model is more accurate than the k-ω model.

**MODELING**

The two-layer, Realizable k-ε turbulence model predicted pressure losses 3.7 – 10.3 percent lower than experimental measurements for flow rates ranging from 0.61 to 3.66 m/s*$(Kg/m^3)^{1/2}$. 3.66 m/s*$(Kg/m^3)^{1/2}$ is well most plausible industrial vapor flow rates. Therefore, the turbulence model used is capable of simulating single phase flow across the range of distillation vapor rates to within 10 percent error.

Pressure loss was calculated using the Stichlmair model in order to compare simulation accuracy against a model commonly used in industry. Several different calculations were employed using both default packing specific parameters as well as those calculated specifically for the experimental and simulation geometry. The simulation outperformed all adaptations of the Stichlmair model in both accuracy and the nature of the response to increasing flow rate. This clearly demonstrates the power of CFD simulations. Even with a nearly 13 mm discrepancy in column diameter, the CFD simulations outperform what is considered to be a robust model for predicting pressure loss. Moreover, CFD simulations not only predict performance but also allow the researcher to assess the limiting factors which contribute to decreased performance.

**DIAGNOSTICS**

The extents of the velocity distribution were analyzed as an example of such an assessment. Negative flow was present along the entire length of the packing. Additional flow disruptions were observed at both the wiper band and the packing joints. The wiper bands induced a jump in the maximum velocity which corresponds to the decrease in cross-sectional area. The packing joints caused a notable increase in negative flow rate. This corresponds to previous work which observed multiple flow disruptions at the packing joint.[21] This negative flow would result in back mixing and increased pressure dissipation. For these reasons, it is apparent that the joint region introduces phenomena which act at cross purposes to efficient mass transfer.

A similar analysis conducted with area-weighted-average pressure proved similarly enlightening. Pressure loss was essentially linear with respect to progression through the structured packing. This relationship did not hold true at the packing joint. The joint imposed additional pressure loss similar in nature to that which is observed in flow through an orifice. In this way each joint imposes a finite loss which cascades through the column.

This effect was confirmed empirically by measuring the pressure loss through equivalent heights of half and whole packing elements. The greater number of joints in the half-element packing resulted in a greater overall pressure drop at all studied flow rates. From this it can be concluded that the requisite reboiler pressure is proportional to the number of joints installed in a column.

Streamline visualizations were used to analyze the bulk flow through and between the packing elements. A wide distribution of flow rates and many chaotic flow disruptions were observed in the packing stack. This ability to quickly and easily locate

and analyze dissipative flow phenomena is unique to CFD analyses and demonstrates another powerful aspect of this type of study.

Contour plots were used to study the variation of pressure and velocity distributions in horizontal planes. The nature of the distribution was found to vary as a function of height. The velocity plots showed the velocity peaked in the channel centers and between the packing and the wall. Negative flows and stagnation were common near the packing surface. Combining the results of the streamline and contour plot analyses leads to the conclusion that many different flow paths exist in the vapor phase of distillation. This would lead to a distribution of residence times and, consequently, concentrations in the vapor exiting the packing. If this distribution could be narrowed or eliminated it would simplify distillation control schemes and improve the energy efficiency.

**SIMILARITY**

Simulations of water flow proved to be inaccurate. Simulation predictions of pressure loss were approximately 40 percent lower than experimental measurements. All pressure loss measurements and simulations were compared in non-dimensional form. The results collapsed to a single trend regardless of fluid or data source (experiment vs. simulation). This suggests the error is likely a result of inaccuracies in the CFD geometry relative to the experimental setup or variation in fluid properties due to temperature variation in the experiment as opposed to an inability to capture the flow physics.

# Chapter 7: Future Work

This project is meant as a first step along the path toward direct simulation of the physics occurring in two-phase flow through structured packing. Important gains were made in documenting the mesh and simulation parameters necessary to accurately capture single phase nitrogen flow. Of course, the procedures employed here must undergo repetitive trials, expanded coverage, and be upgraded along the way before they can be viewed as a comprehensive guide. Analogous investigations must be also made into factors dictating liquid film flow along the packing surface absent any induced vapor. Only when each half of the puzzle is independently and thoroughly characterized can two-phase simulations be attempted with any credibility.

### VAPOR PHASE

Some uncertainty was encountered in this study due to errors present in the scanned geometry. This could be corrected by modifying the sample preparation prior to scanning. A piece of plastic packing could be scanned while inside a metal tube with a 146 mm ID. The metal tube would force the wiper bands to conform to a regular diameter equal to the ID employed in the experimental geometry. The CT scan data could be high-pass filtered to remove the metal tube. The resulting STL file would contain a digital geometry comprised only of a piece of plastic packing with the correct OD. The remaining geometry generation procedure could be repeated as described above.

Alternately, scans could be performed on packing without wiper bands installed. A digital representation of a wiper band could be generated in ICEM. This would permit modification of the shape and size of the wiper band. The wiper band and wall gap could be made to enforce an annular-to-packing area ratio similar to that found in industrial

distillation columns. This would permit comparison of the simulation results to a large catalog of industrial data available in the literature. This could also negate the need for empirical fitting parameters when model results are scaled up to predict industrial performance.

The simulated nitrogen pressure loss predictions displayed an increasing error with increasing flow rate. One possible explanation for this is that the mesh was not sufficiently refined to capture the decreasing boundary layer thickness which accompanies higher flow rates. A minimum cell edge size of 0.45 mm was employed throughout this study due to memory restrictions. However, the results were shown to be independent of mesh density. Therefore, the procedure could be repeated with the existing geometry using a much smaller minimum edge length (< 0.35). The file size could be reduced by employing a lower tet/poly density (< 1.0) and a higher mesh growth rate (1.3 – 1.5). This would help decouple the effects of geometry inaccuracy versus mesh resolution.

**LIQUID PHASE**

The physics at play in the liquid film flowing along the packing surface differ greatly from those which dictate bulk phase flow. Therefore, a distinctly different approach will need to be developed to properly simulate these flows. Specifically, simulation of liquid film flows will require changes in the boundary conditions and meshing procedure.

Unlike the continuous vapor phase, the liquid is introduced at discrete points above the packing and allowed to drain down the packing surface. Therefore, a number of planes must be generated above the top section of packing and designated as mass flow inlets. Continuing to conform the simulation geometry to an experimental analog promises to enable validation against empirical results. The work of Green *et al*. would

provide a good reference for liquid hold ups as a function of liquid rate.[19] That work employed four drip points with diameters of approximately 38 mm spaced 21 mm from the column axis and placed at 90 degree angles. The drip points were approximately 25 mm above the top of the packing. Making the disconnect surfaces belong to a single part name would allow the researcher to specify the total mass flow rate into the column as opposed to calculating the flow through each drip point. Unfortunately, this would also prevent an analysis of mal-distributed flow. The lowest plane could be set to a pressure outlet to remove the liquid once it fell off the packing surface. The geometry could also be made much smaller as there would be no need of a large open region before or after the packing. These regions allow the vapor to distribute itself prior to entering the packing and then for the dissipation of any recirculation after the fluid leaves the packing.

Liquid films on structured packing are believed to be less than 2 mm in thickness and predominately laminar. This would require a highly refined mesh in order to accurately resolve the liquid film and fluid-fluid interface. A coarse mesh would be needed away from the interface to reduce file size and computation time. This could be accomplished through the use of a prism layer in addition to the core mesh.

A prism layer mesh is composed of orthogonal prismatic cells that usually reside next to wall boundaries in the volume mesh.[12] The prism layer is typically relatively thin and highly refined. They are used to accurately capture heat transfer or low Reynolds number flows. Prism layers are typically combined with a core mesh which occupies the majority of the volume. An example is given in figure 43.

A prismatic layer with constant edge lengths could be created to extend up to 3 mm beyond the packing surface. The edge length would likely need to be below 0.25 mm to accurately study the two-phase interface and test for the effect of surface treatments on liquid flow behavior. Since the primary focus would be on the liquid phase,

the core mesh could utilized very large minimum edge lengths (>1.0 mm) and large growth rates (>1.5) to minimize file size.

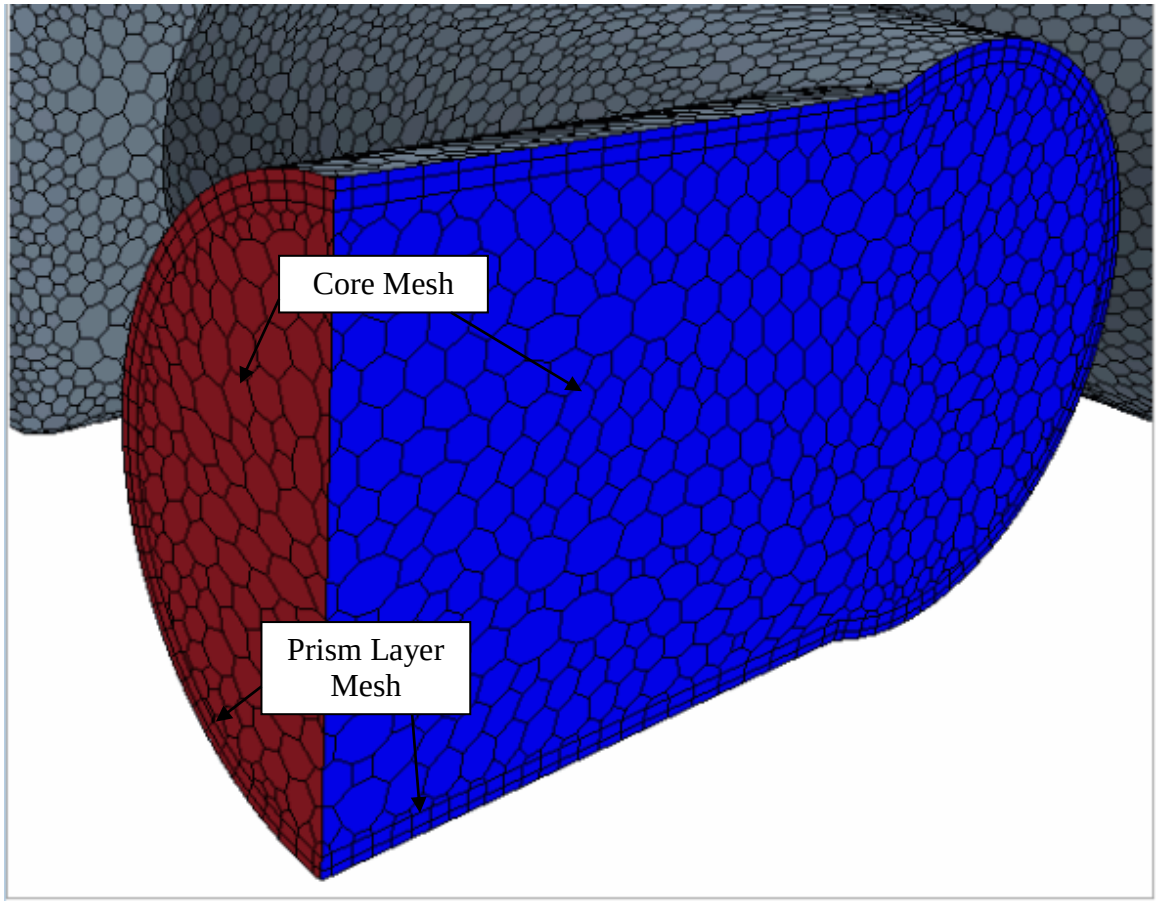


Figure 43: A prism layer mesh combined with a polyhedral core mesh.[12]

**TWO PHASE**

A two phase study would need to incorporate the attributes of the geometries used in each of the single phase studies. This would entail the use of four boundary conditions and a hybrid mesh scheme. The liquid could be introduced as in the single-phase film-flow study. However, a pressure outlet cannot be used as the bottom plane in this case. This would allow the vapor to flow out the bottom of the geometry without passing

through the packing. A possible alternative would be to use a hole in the column wall near the base. This could be specified as a pressure outlet boundary with a pressure of 13 mm of water. The back pressure would ensure this outlet boundary is always covered with water.

A vapor inlet plane would need to be created to mimic a vapor distributor. This could be modeled as a multiple planes evenly spaced below the bottom of the packing stack. The vapor could be introduced in a downward direction to optimize vapor distribution and avoid fluidization of the falling liquid. The plane at the top of the geometry could be set as a pressure outlet to allow the vapor to escape. This arrangement is depicted in figure 44.

The hybrid mesh would need employ a prism layer resolved enough to capture the liquid phenomena like surface renewal and wave formation and a polyhedral as well as the two-phase interface and a core mesh capable of accurately predicting the pressure loss associated with the vapor phase negotiating the packing channels.

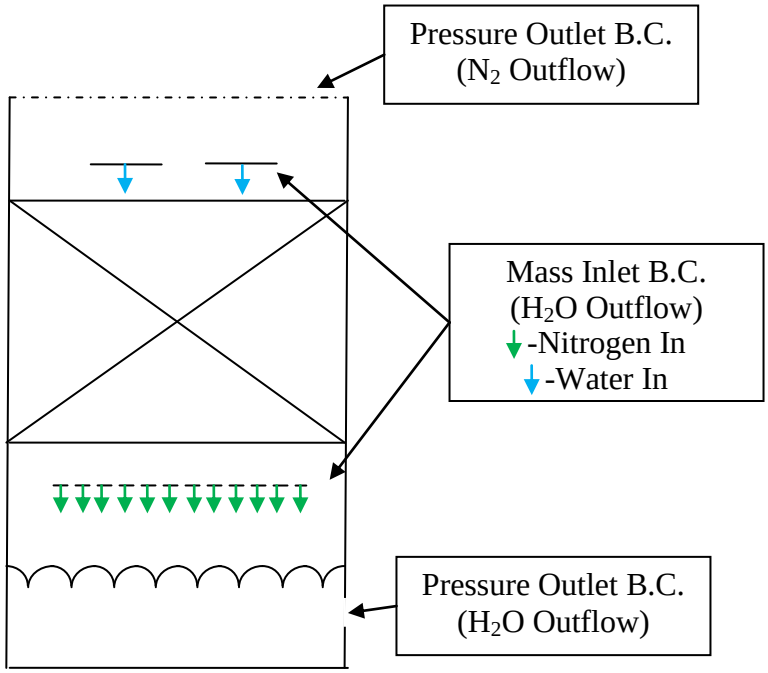


Figure 44: A possible arrangement for boundary conditions (B.C.) for two phase flow.

# Appendices

## MESH SETTINGS

### Coarse Mesh

| | Properties | Mesh 1 |
|---|---|---|
| Mesh 1 | Per-Region Meshing | ☐ |
| | Interfaces | [] |
| | Regions | [Region 1] |
| | OOC translation | ☐ |
| | Verbose Output | ☐ |
| Models | | |
| Polyhedral Mesher | Run Optimizer | ☑ |
| Surface Remesher | Do curvature refinement | ☑ |
| | Do proximity refinement | ☑ |
| | Minimum face quality | 0.05 |
| | Enable automatic surface repair | ☑ |
| Surface Wrapper | Do curvature refinement | ☑ |
| | Do proximity refinement | ☑ |
| | Do gap closure | ☐ |
| | Do wrapper mesh alignment | ☐ |
| Reference Values | | |
| Base Size | Value | 30.0 mm |
| Automatic Surface Repair | Fix pierced faces | ☑ |
| | Fix close proximity faces | ☑ |
| | Fix poor quality faces | ☑ |
| | Connected surface count limit | None |
| | Connected surface size limits | None |
| Minimum Proximity | Minimum Proximity | 0.05 |
| Minimum Quality | Minimum Quality | 0.01 |
| CAD Projection | Project to CAD | ☑ |
| Surface Curvature | # Pts/circle | 36.0 |
| Surface Growth Rate | Surface Growth Rate | 1.3 |
| Surface Proximity | # Points in gap | 1.0 |
| | Search Floor | 0.0 mm |
| Surface Size | Relative/Absolute | Relative to base |
| | Size Method | Min and Target |
| Relative Minimum Size | Percentage of Base | 1.5 |
| | Absolute Size | 0.45 mm |
| Relative Target Size | Percentage of Base | 100.0 |
| | Absolute Size | 30.0 mm |
| Tet/Poly Density | Density | 1.0 |
| | Growth Factor | 1.0 |
| Tet/Poly Volume Blending | Blending Factor | 1.0 |
| Wrapper Feature Angle | Angle | 30.0 |
| Wrapper Scale Factor | Percentage | 50.0 |
| Volumetric Controls | | |

## Medium Mesh

| | Properties | Mesh 1 |
|---|---|---|
| Mesh 1 | Per-Region Meshing | ☐ |
| | Interfaces | [] |
| | Regions | [Region 1] |
| | OOC translation | ☐ |
| | Verbose Output | ☐ |
| Models | | |
| Polyhedral Mesher | Run Optimizer | ☑ |
| Surface Remesher | Do curvature refinement | ☑ |
| | Do proximity refinement | ☑ |
| | Minimum face quality | 0.05 |
| | Enable automatic surface repair | ☑ |
| Surface Wrapper | Do curvature refinement | ☑ |
| | Do proximity refinement | ☑ |
| | Do gap closure | ☐ |
| | Do wrapper mesh alignment | ☐ |
| Reference Values | | |
| Base Size | Value | 10.0 mm |
| Automatic Surface Repair | Fix pierced faces | ☑ |
| | Fix close proximity faces | ☑ |
| | Fix poor quality faces | ☑ |
| | Connected surface count limit | None |
| | Connected surface size limits | None |
| Minimum Proximity | Minimum Proximity | 0.05 |
| Minimum Quality | Minimum Quality | 0.01 |
| CAD Projection | Project to CAD | ☑ |
| Surface Curvature | # Pts/circle | 48.0 |
| Surface Growth Rate | Surface Growth Rate | 1.2 |
| Surface Proximity | # Points in gap | 1.0 |
| | Search Floor | 0.0 mm |
| Surface Size | Relative/Absolute | Relative to base |
| | Size Method | Min and Target |
| Relative Minimum Size | Percentage of Base | 4.5 |
| | Absolute Size | 0.45 mm |
| Relative Target Size | Percentage of Base | 150.0 |
| | Absolute Size | 15.0 mm |
| Tet/Poly Density | Density | 1.0 |
| | Growth Factor | 0.98 |
| Tet/Poly Volume Blending | Blending Factor | 1.0 |
| Wrapper Feature Angle | Angle | 30.0 |
| Wrapper Scale Factor | Percentage | 50.0 |
| Volumetric Controls | | |

## Fine Mesh

| | Properties | Mesh 1 |
|---|---|---|
| Mesh 1 | Per-Region Meshing | ☐ |
| | Interfaces | [] |
| | Regions | [Region 1] |
| | OOC translation | ☐ |
| | Verbose Output | ☐ |
| Models | | |
| Polyhedral Mesher | Run Optimizer | ☑ |
| Surface Remesher | Do curvature refinement | ☑ |
| | Do proximity refinement | ☑ |
| | Minimum face quality | 0.05 |
| | Enable automatic surface repair | ☑ |
| Surface Wrapper | Do curvature refinement | ☑ |
| | Do proximity refinement | ☑ |
| | Do gap closure | ☐ |
| | Do wrapper mesh alignment | ☐ |
| Reference Values | | |
| Base Size | Value | 1.0 mm |
| Automatic Surface Repair | Fix pierced faces | ☑ |
| | Fix close proximity faces | ☑ |
| | Fix poor quality faces | ☑ |
| | Connected surface count limit | None |
| | Connected surface size limits | None |
| Minimum Proximity | Minimum Proximity | 0.05 |
| Minimum Quality | Minimum Quality | 0.01 |
| CAD Projection | Project to CAD | ☑ |
| Surface Curvature | # Pts/circle | 48.0 |
| Surface Growth Rate | Surface Growth Rate | 1.1 |
| Surface Proximity | # Points in gap | 1.0 |
| | Search Floor | 0.0 mm |
| Surface Size | Relative/Absolute | Relative to base |
| | Size Method | Min and Target |
| Relative Minimum Size | Percentage of Base | 45.0 |
| | Absolute Size | 0.45 mm |
| Relative Target Size | Percentage of Base | 450.0 |
| | Absolute Size | 4.5 mm |
| Tet/Poly Density | Density | 1.05 |
| | Growth Factor | 0.97 |
| Tet/Poly Volume Blending | Blending Factor | 1.0 |
| Wrapper Feature Angle | Angle | 30.0 |
| Wrapper Scale Factor | Percentage | 50.0 |
| Volumetric Controls | | |

## NITROGEN SIMULATION SETTINGS

Physics Models

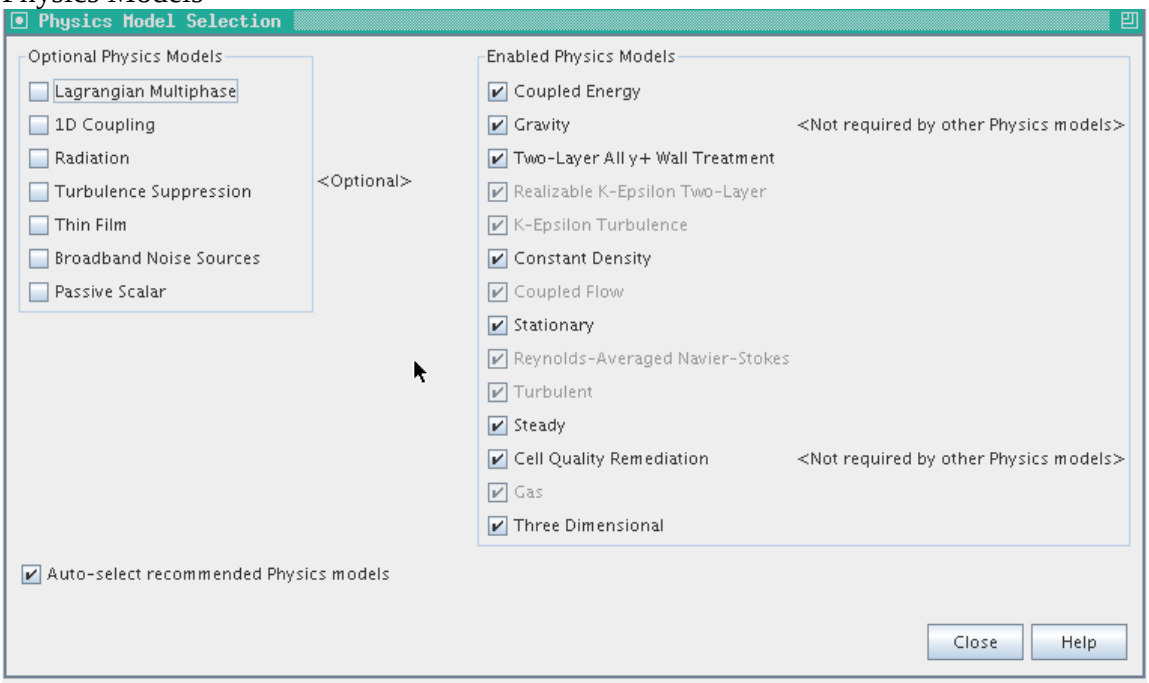

Physical Properties

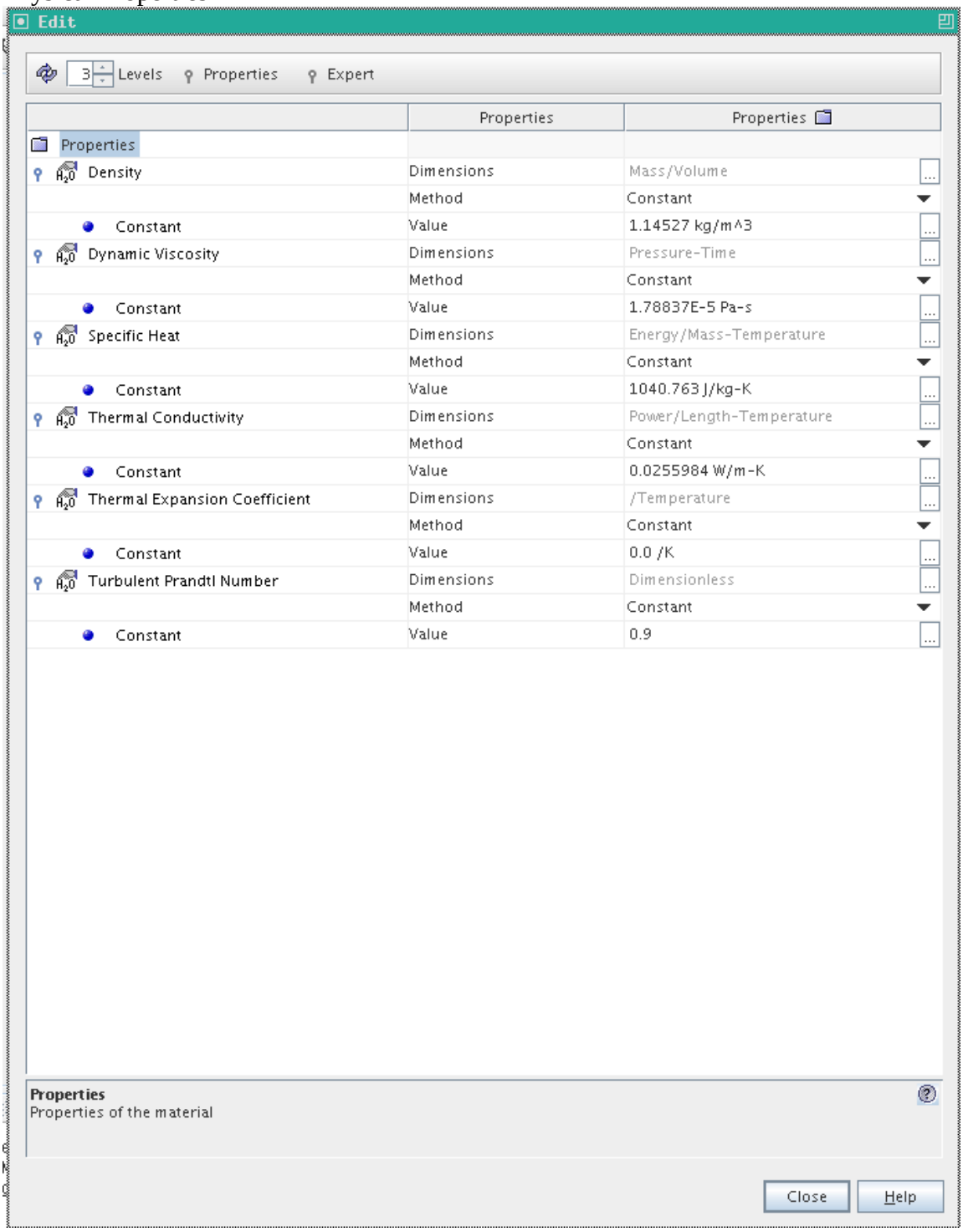

Nitrogen Reference Values

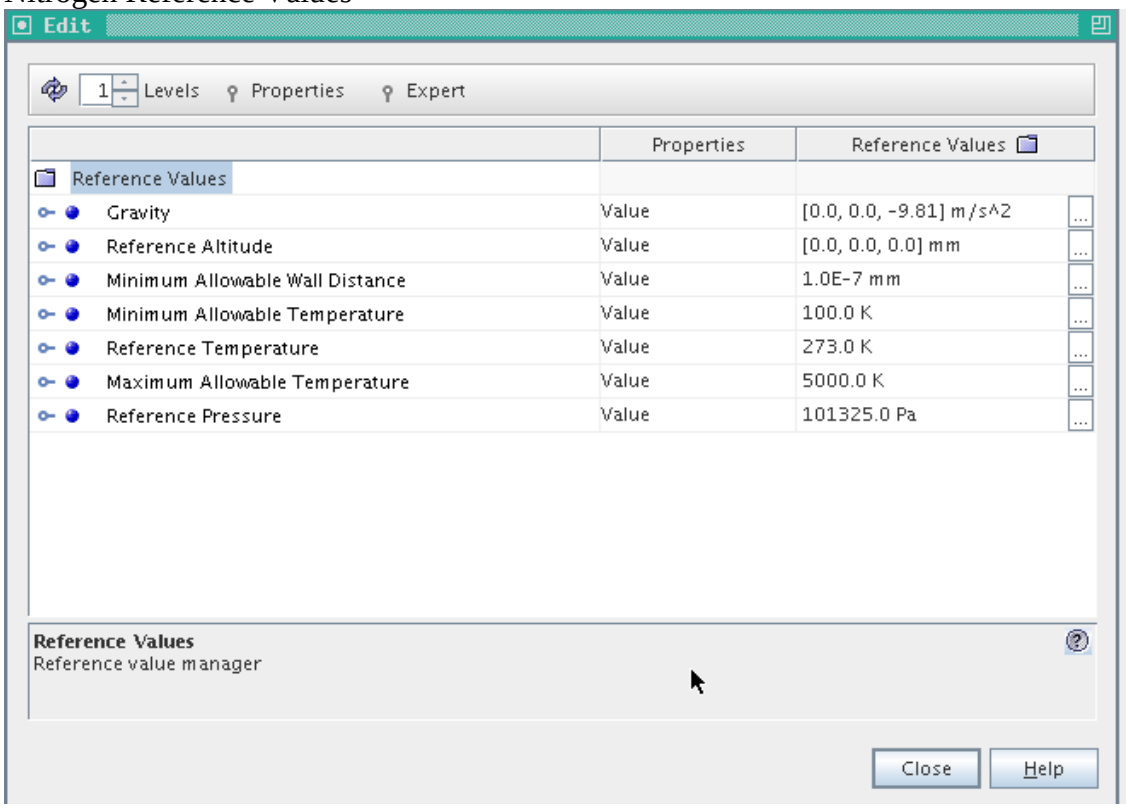

Nitrogen Simulation Solver Settings

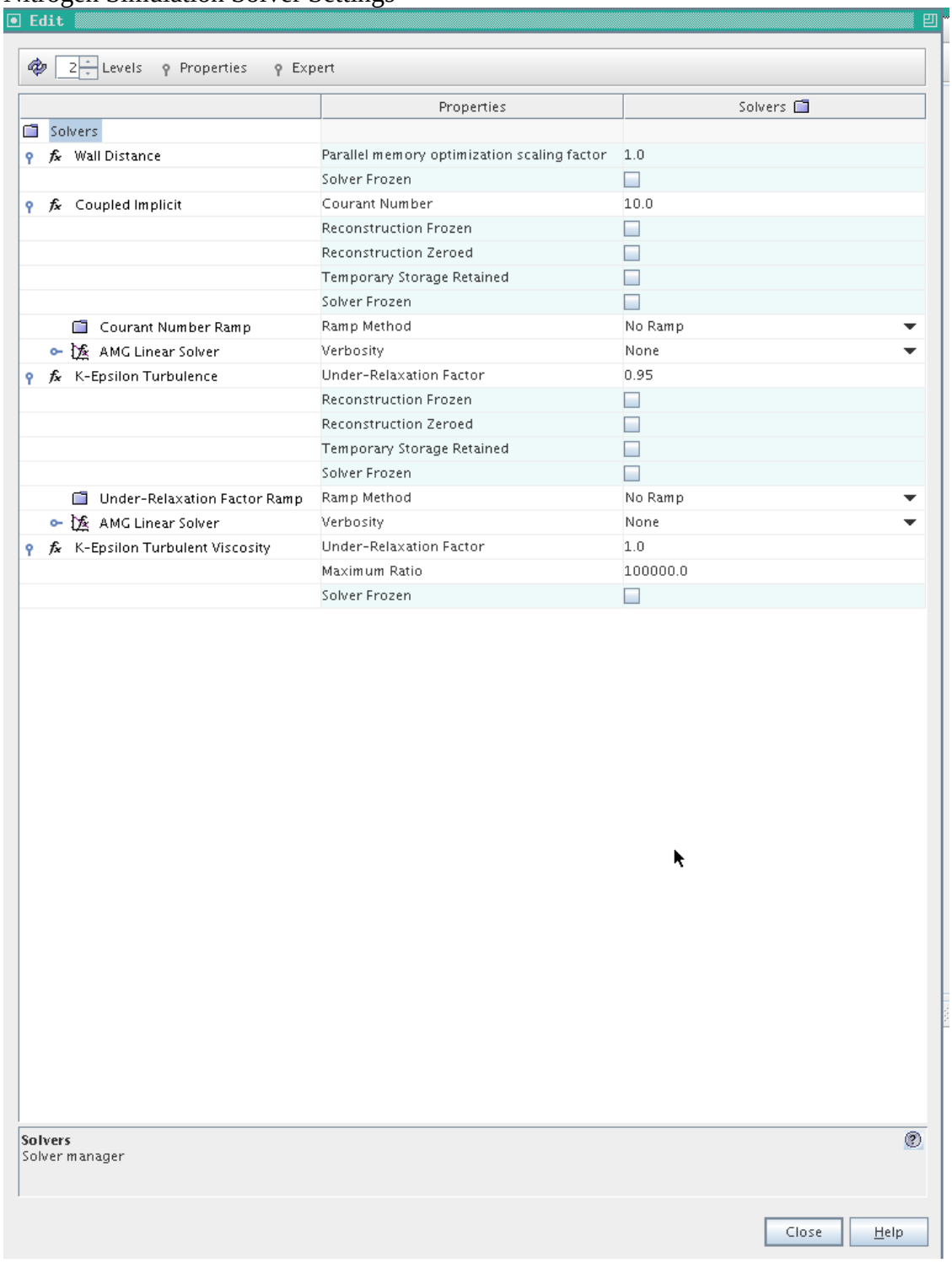

Nitrogen Simulation Initial Conditions

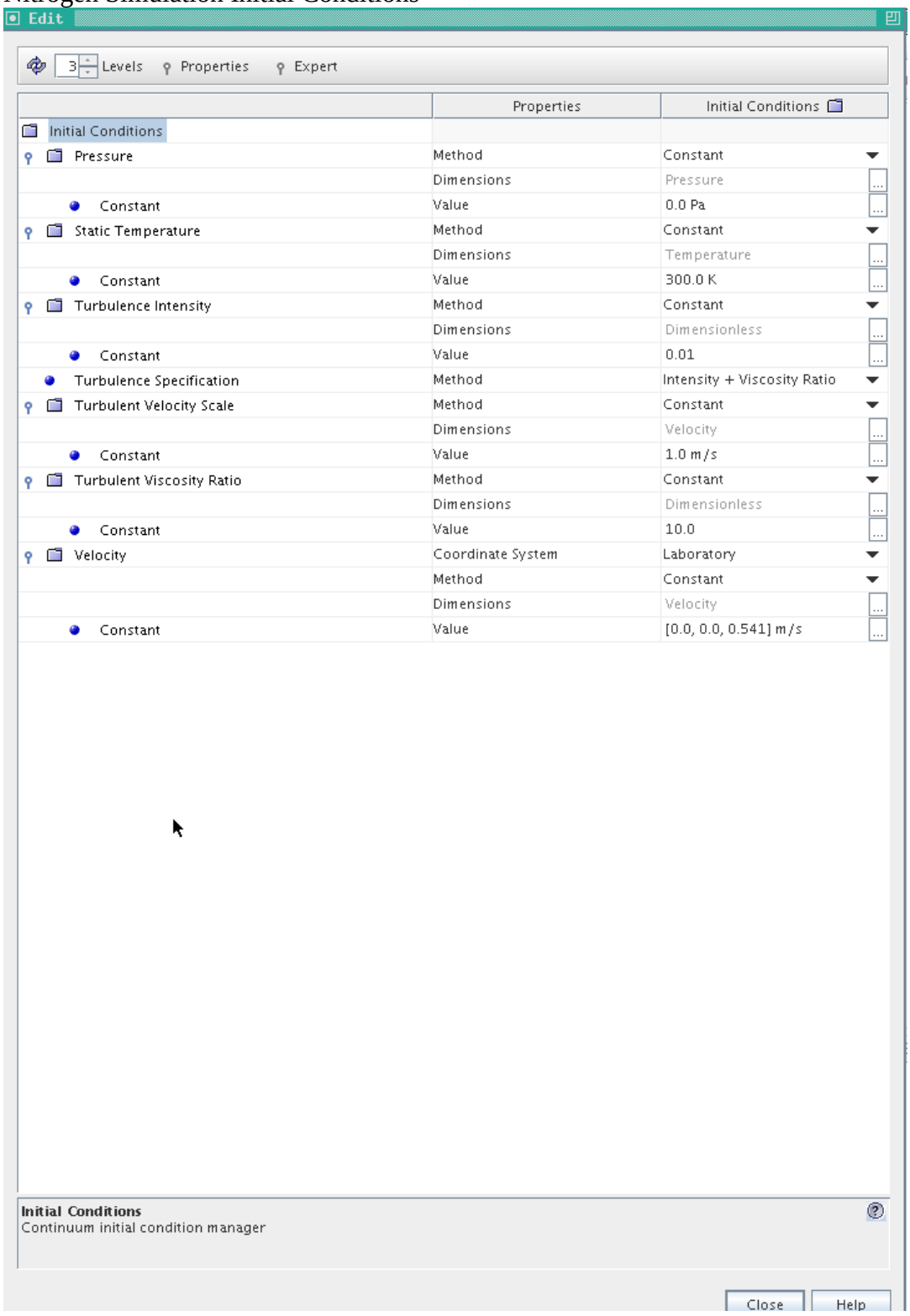

## WATER SIMULATION SETTINGS

Physics Models

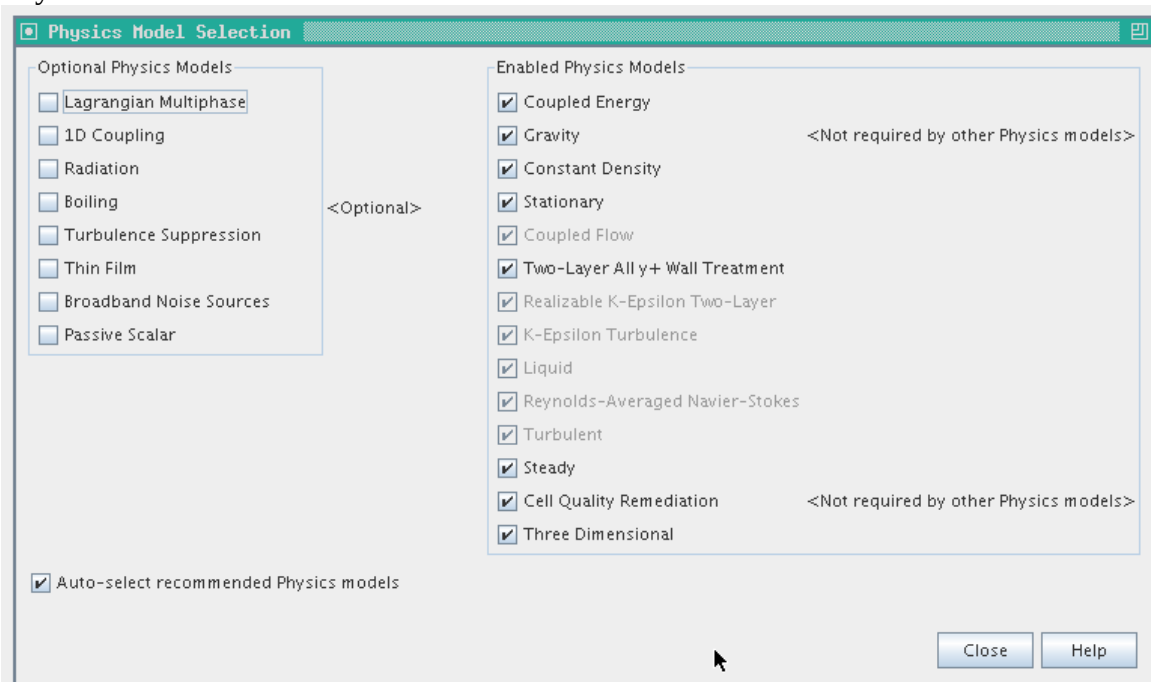

Physical Properties

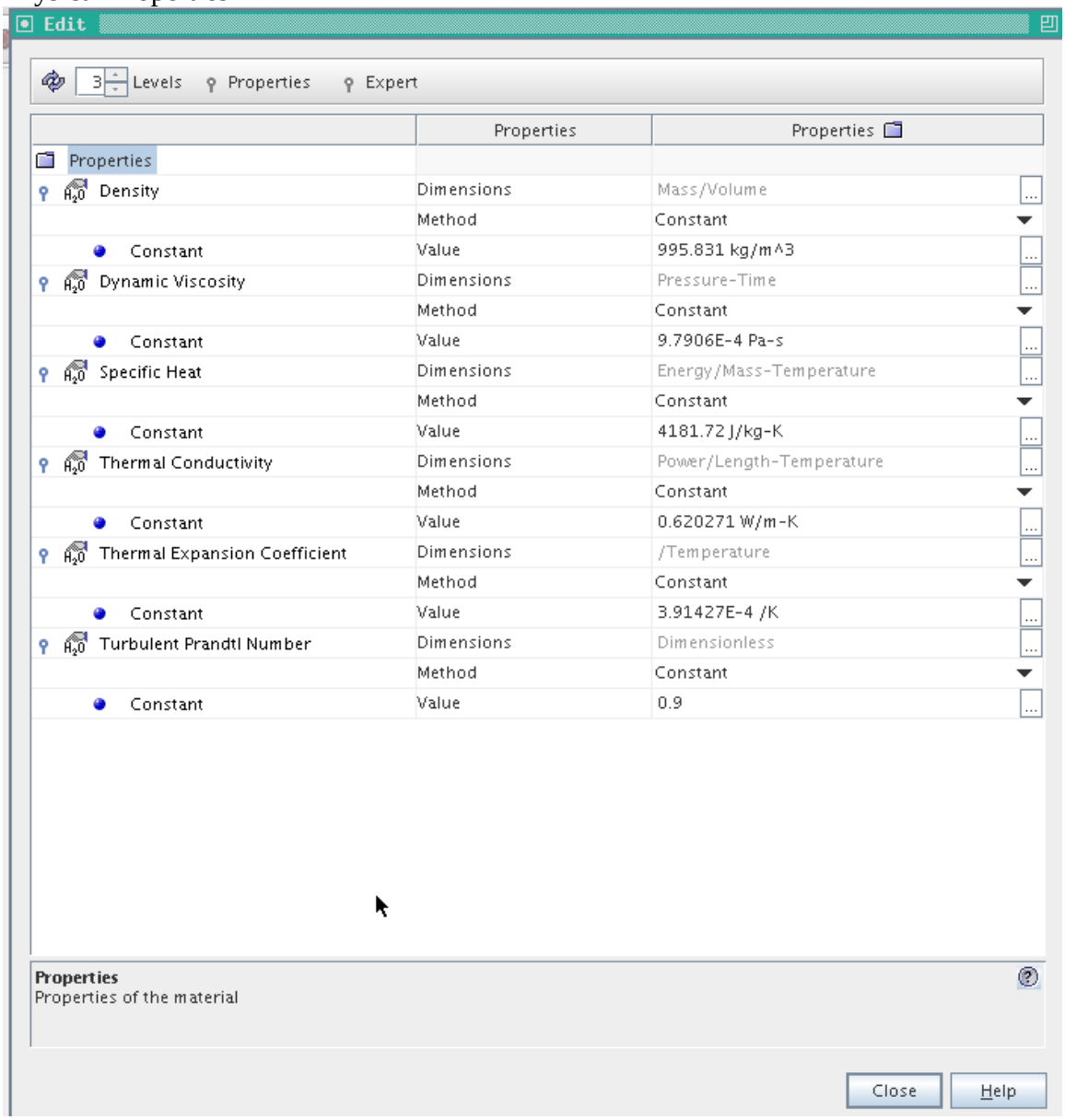

Reference Values

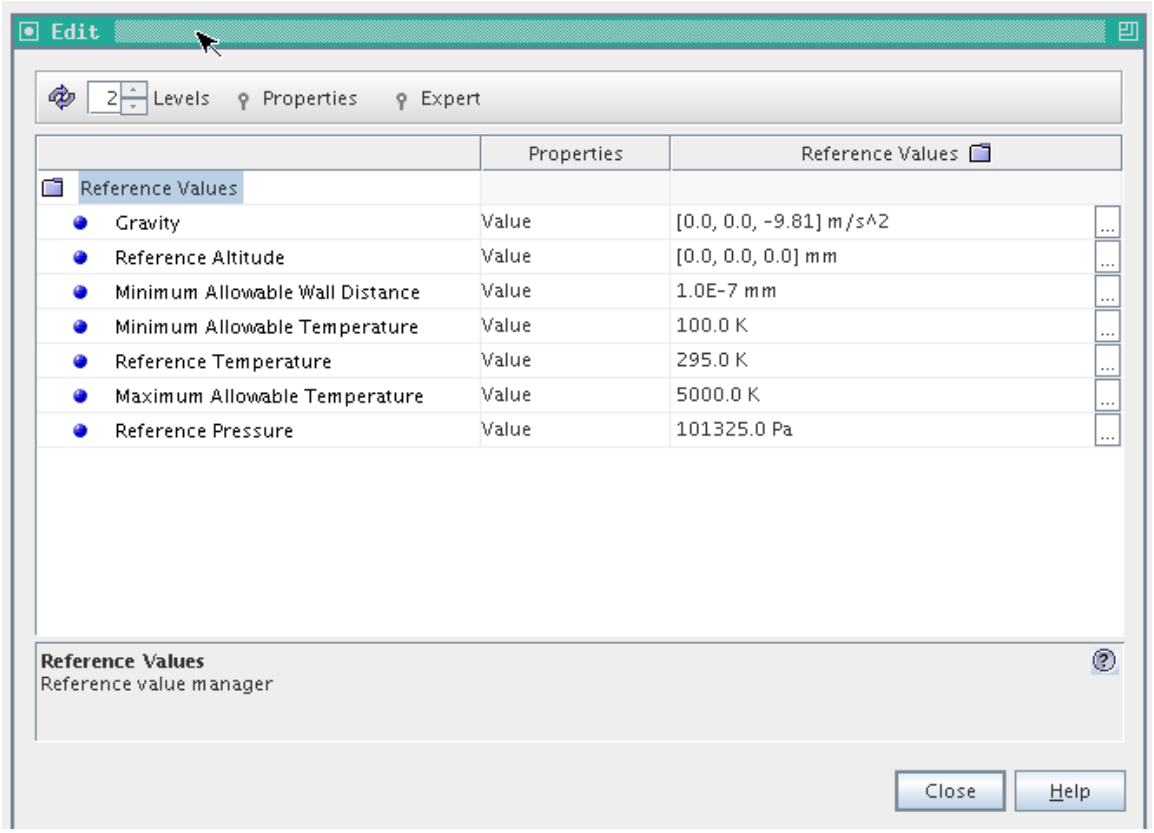

Simulation Solver Settings

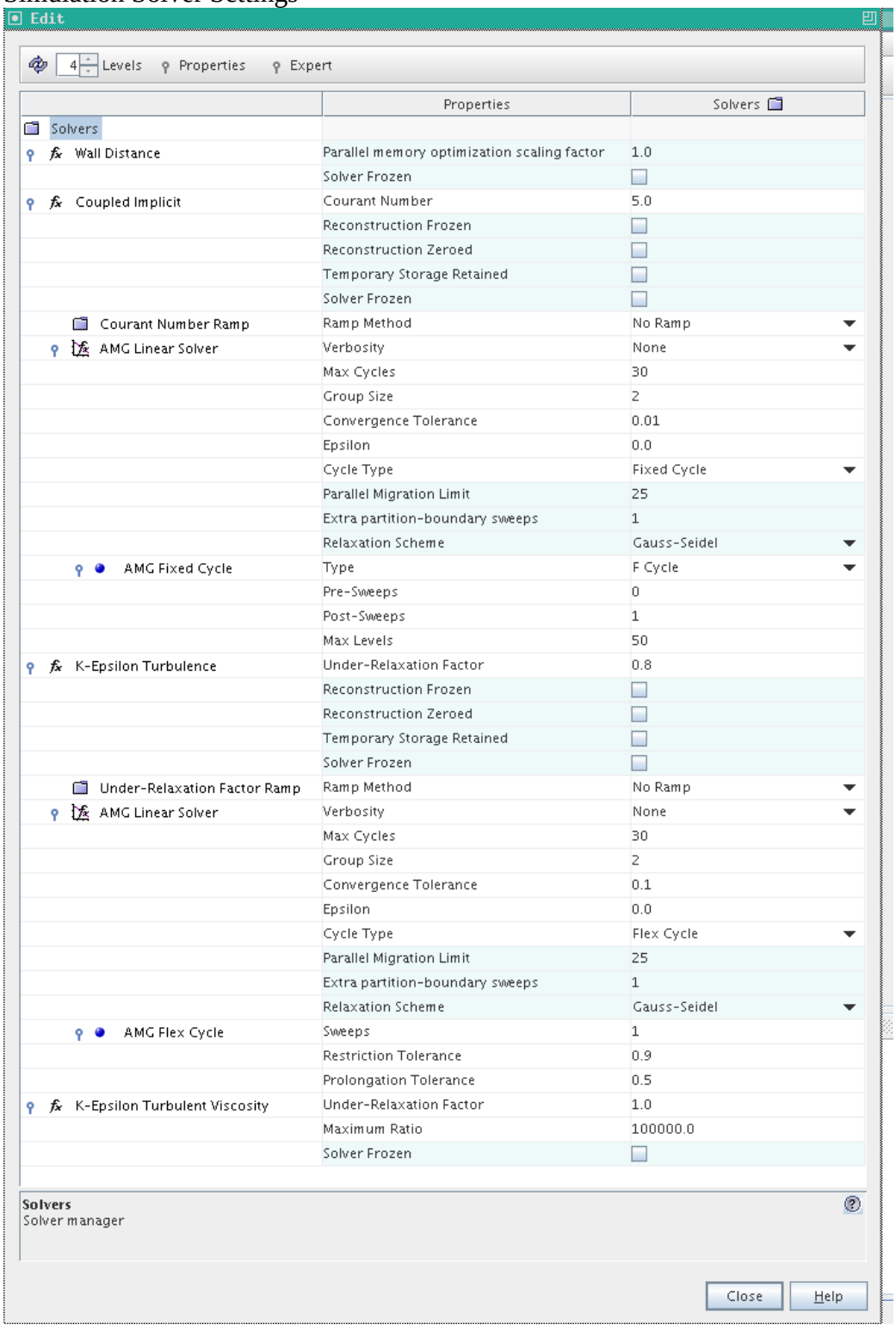

Simulation Initial Conditions

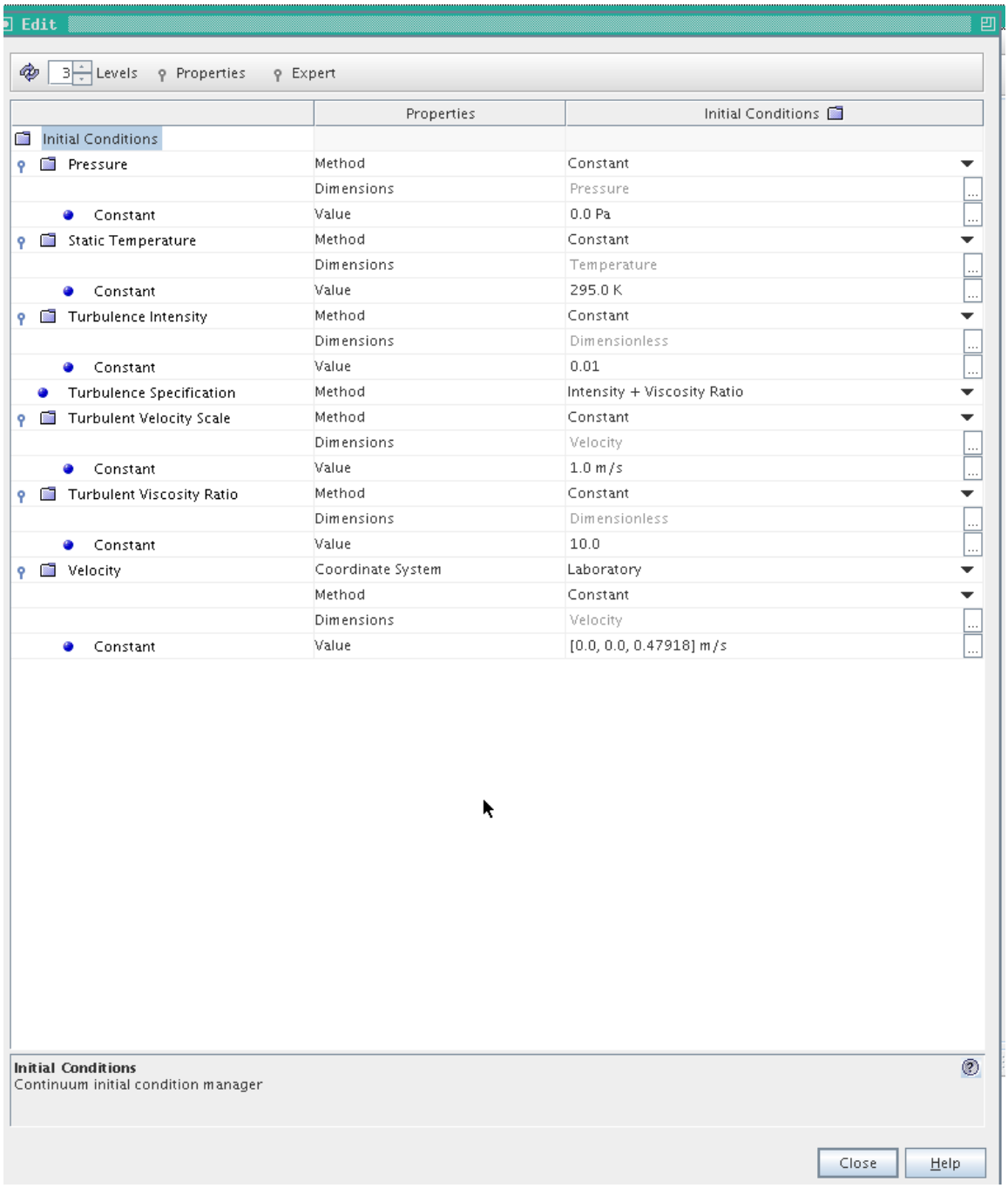

Simulation Options

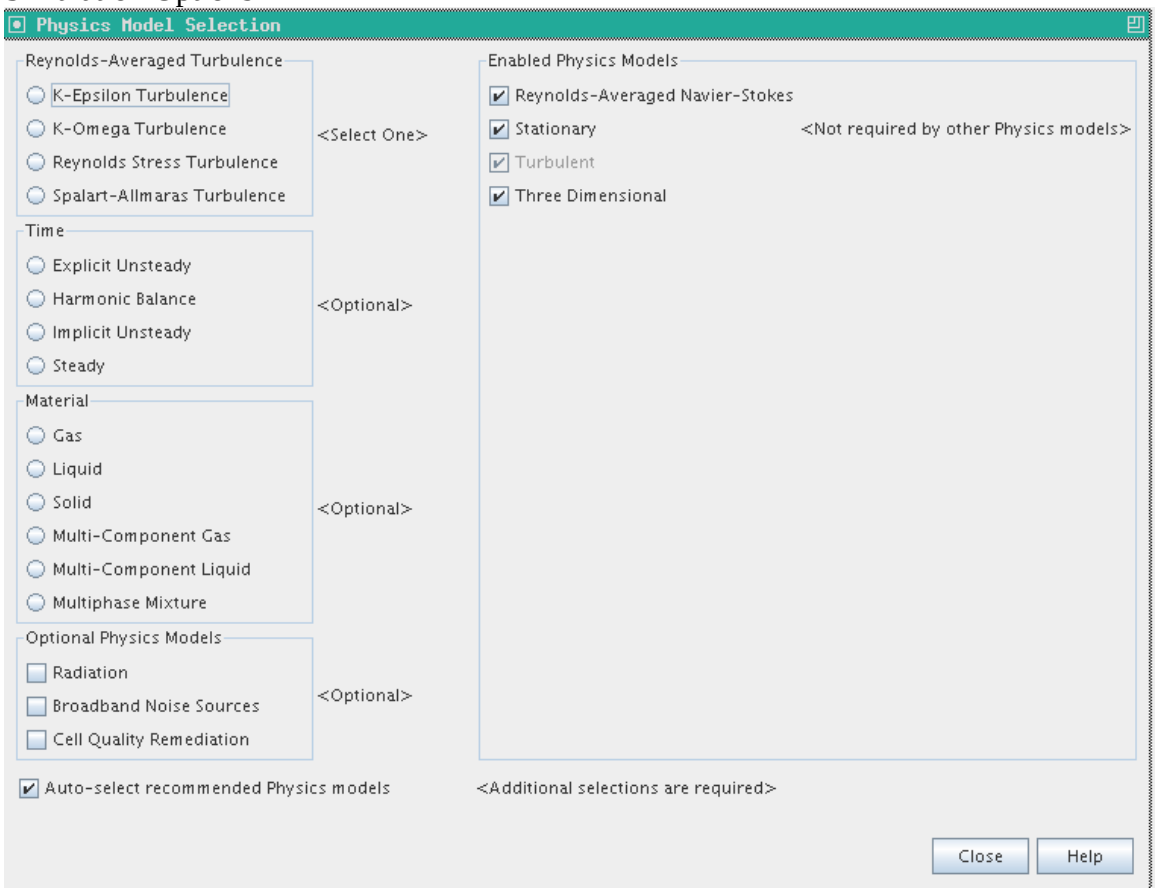

Available Turbulence Models

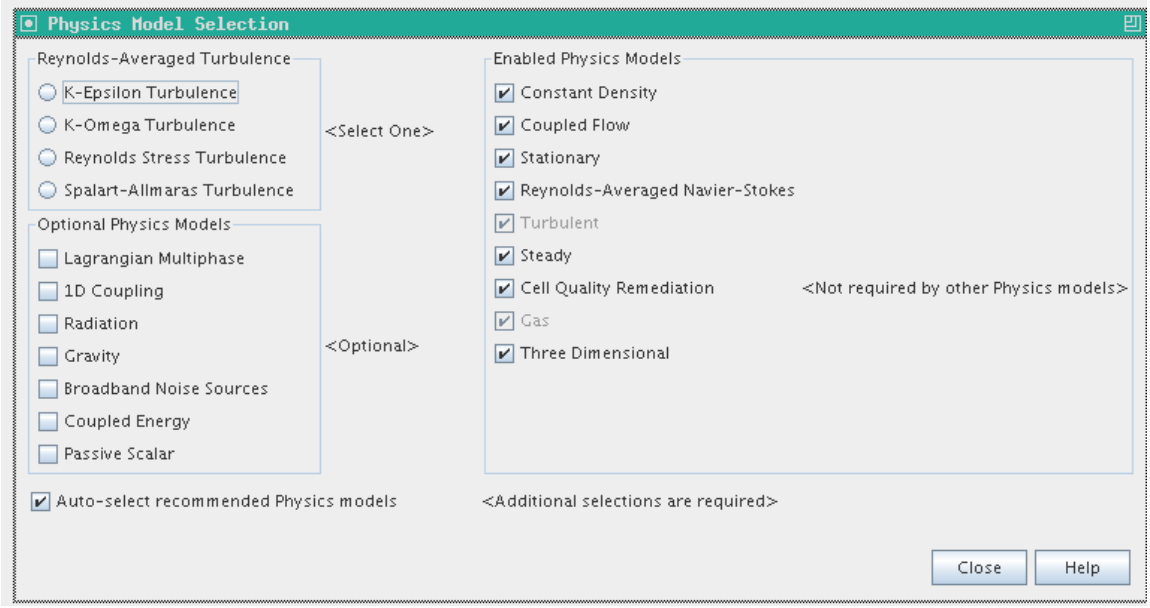

## LABVIEW VI DETAILS

GUI

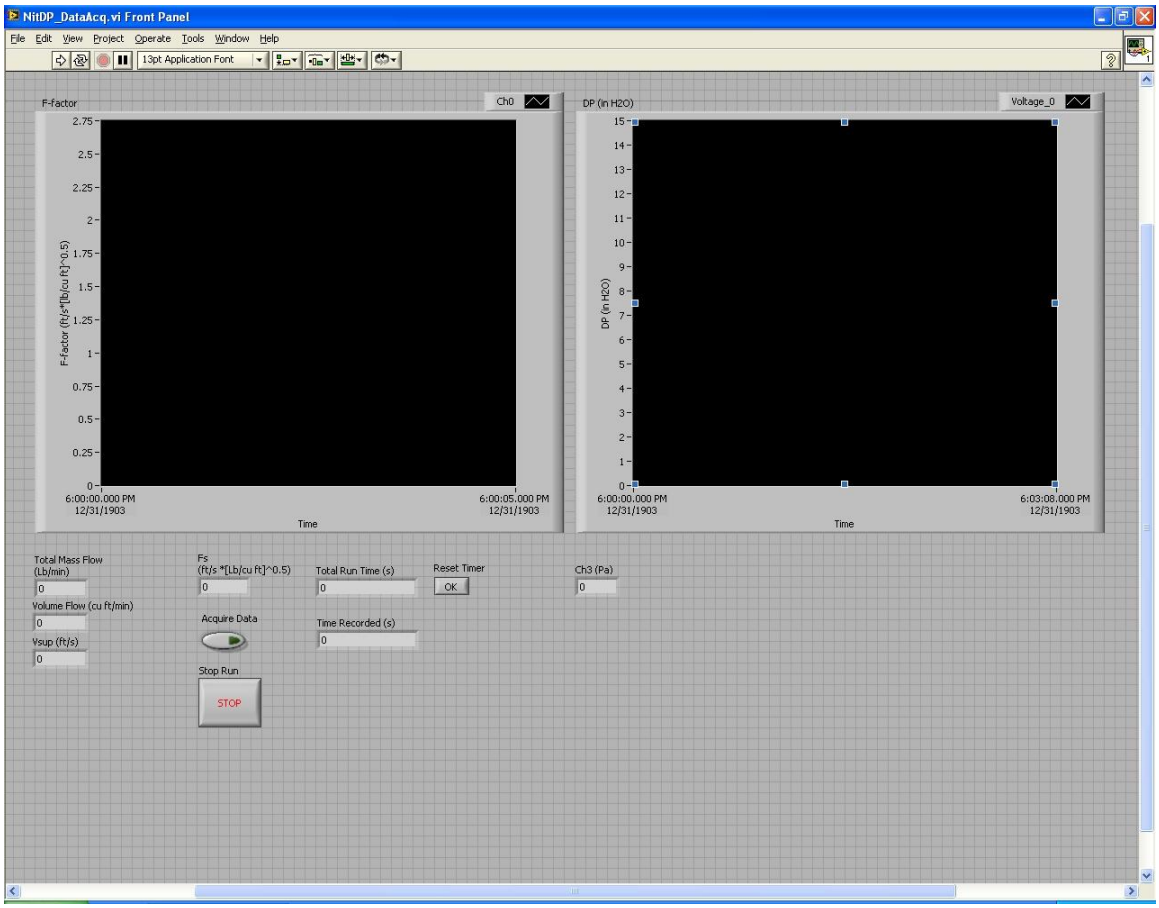

Wire Diagram

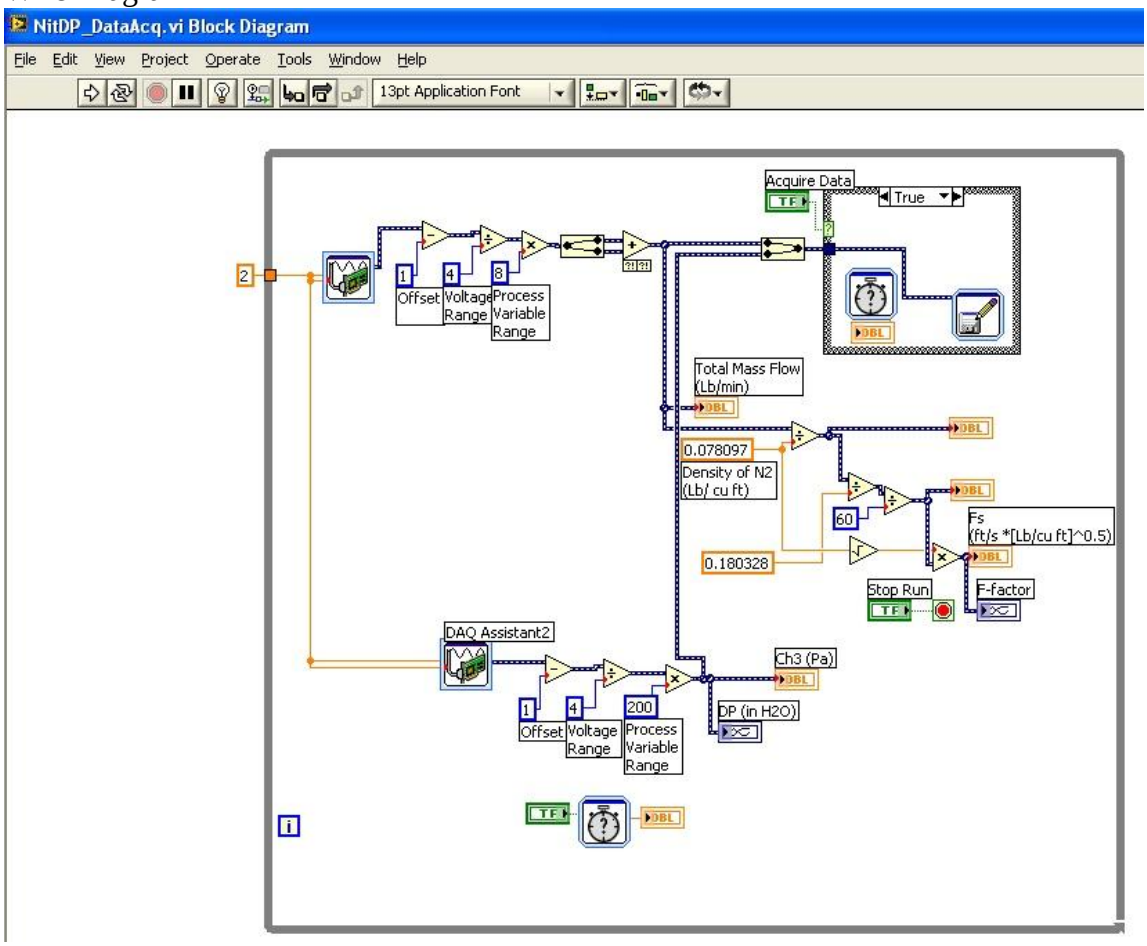

# References


1. Distillation Column Modeling Tools. *U.S. Department of Energy* **2001,** Office of Industrial Technologies; Energy Efficiency and Renewable Energy, 2.
2. Nalven, G. F., *Distillation and Other Industrial Separations*. American Instituge of Chemical Engineers: New York, NY, 1997; Vol. Q-4.
3. Doherty, M. F.; Fidkowski, Z. T.; Malone, M. F.; Raylor, R., Distillation. In *Perry's Chemical Engineers' Handbook*, Green, D. W.; Perry, R. H., Eds. McGraw-Hill: 2008.
4. Seader, J. D.; Henley, E. J., *Separation Process Principles*. 2nd ed.; John Wiley & Sons: 2006; p 756.
5. Tsai, R. Mass Transfer Area of Structured Packing. The University of Texas, Austin, 2010.
6. Tsai, R. E.; Schultheiss, P.; Kettner, A.; Lewis, J. C.; Seibert, A. F.; Eldridge, R. B.; Rochelle, G. T., Influence of Surface Tension on Effective Packing Area. *Industrial & Engineering Chemistry Research* **2008,** 47, (4), 1253-1260.
7. Wang, G. Q.; Yuan, X. G.; Yu, K. T., Review of Mass-Transfer Correlations for Packed Columns. *Industrial & Engineering Chemistry Research* **2005,** 44, (23), 8715-8729.
8. Byrd, R. B.; Steward, W. E.; Lightfoot, E. N., *Transport Phenomena*. Second ed.; John WIley & Sons, Inc: New York, 2002; p 895.
9. Speziale, C. G., Analytical Methods for the Development of Reynolds-Stress Closures in Turbulence. *Annual Review of Fluid Mechanics* **1991,** 23, 107-57.
10. McCabe, W. L.; Smith, J. C.; Harriot, P., *Unit Operations of Chemical Engineering*. Seventh ed.; McGraw-Hill: Boston, 2005; p 1140.
11. Casey, M.; Wintergerste, T., *Best Practice Guidelines*. 1.0 ed.; European Research Community On Flow, Turbulence and Combustion: 2000; p 94.
12. STAR-CCM+ User Manual. In CD-Adapco.
13. Launder, B. E.; Spalding, D. B., The numerical computation of turbulent flows. *Computer Methods in Applied Mechanics and Engineering* **1974,** 3, (2), 269-289.
14. Wilcox, D. C., *Turbulence Modeling for CFD*. 3rd ed.; DCW Industries: La Cãnada, CA, 2006; p 522.
15. Harman, T. L.; Dabney, J.; Richert, N., *Advanced Engineering Mathematics with Matlab*. Second ed.; Brooks/Cole: United States, 2000; p 750.
16. Thompson, J. F.; Bharat, S.; Weatherrill, N. P., *Handbook of Grid Generation*. 1st ed.; CRC Press: 1998; p 1200.
17. Durran, D., *Numerical Methods for Wave Equations in Geophysical Fluid Dynamics*. 1st ed.; Springer-Verlag: 1999; p 465.
18. Fair, J. R.; Seibert, A. F.; Behrens, M.; Saraber, P. P.; Olujic, Z., Structured Packing Performance-Expermental Evaluation of Two Predictive Models. *Industrial and Engineering Chemistry Research* **2000,** 39, 1788-1796.
19. Green, C. W.; Farone, J.; Briley, J. K.; Eldridge, R. B.; Ketcham, R. A.; Nightingale, B., Novel Application of X-ray Computed Tomography: Determination of Gas/Liquid Contact Area and Liquid Holdup in Structured

Packing. *Industrial & Engineering Chemistry Research* **2007,** 46, (17), 5734-5753.
20. Bravo, J. L.; Fair, J. R., Generalized Correlations for Mass Transfer in Packed Distillation. *Industrial and Engineering Chemistry Research* **1982,** 21, (1), 162-170.
21. Owens, S. A.; Kossmann, A.; Farone, J.; Eldridge, R. B.; Ketcham, R. A., Flow Field Visualization in Structured Packing Using Real Time X-ray Radiography. *Industrial & Engineering Chemistry Research* **2009,** 48, (7), 3606-3618.
22. Petre, C. F.; Larachi, F.; Iliuta, I.; Grandjean, B. P. A., Pressure drop through structured packings: Breakdown into the contributing mechanisms by CFD modeling. *Chemical Engineering Science* **2003,** 58, (1), 163-177.
23. Larachi, F. V.; Petre, C. F.; Iliuta, I.; Grandjean, B., Tailoring the pressure drop of structured packings through CFD simulations. *Chemical Engineering and Processing* **2003,** 42, (7), 535-541.
24. Ataki, A.; Bart, H. J., Experimental and CFD Simulation Study for the Wetting of a Structured Packing Element with Liquids. *Chemical Engineering & Technology* **2006,** 29, (3), 336-347.
25. Raynal, L.; Boyer, C.; Ballaguet, J. P., Liquid holdup and pressure drop determination in structured packing with CFD simulations. *Canadian Journal of Chemical Engineering* **2004,** 82, (5), 871-879.
26. Szulczewska, B.; Zbicinski, I.; Gorak, A., Liquid flow on structured packing: CFD simulation and experimental study. *Chemical Engineering & Technology* **2003,** 26, (5), 580-584.
27. Raynal, L.; Royon-Lebeaud, A., A multi-scale approach for CFD calculations of gas-liquid flow within large size column equipped with structured packing. *Chemical Engineering Science* **2007,** 62, (24), 7196-7204.
28. Brunazzi, E.; Paglianti, A., Mechanistic pressure drop model for columns containing structured packings. *AIChE Journal* **1997,** 43, (2), 317-327.
29. Meier, W.; Hunkeler, R.; Stocker, W. D., Sulzer Mellapack-Eine nue Geordnete Packing fur Stoffaustausch-Apparete. *Chemie Ingenieur Technik* **1979,** 51, 119.
30. Olujic, Z., Effect of column diameter on pressure drop of a corrugated sheet structured packing. *Transactions of the Institution of Chemical Engineers* **1999,** 77, 505.
31. Rocha, J. A.; Bravo, J. L.; Fair, J. R., Distillation columns containing structured packings: A comprehensive model for their Performance. 1. Hydraulic Models. *Industrial and Engineering Chemistry Research* **1993,** 32, 641.
32. Rocha, J. A.; Bravo, J. L.; Fair, J. R., Distillation columns containing structured packings: A comprehensive model for their performance. 2. Mass transfer model. *Industrial and Engineering Chemistry Research* **1996,** 35, 1660.
33. Mahr, B.; Mewes, D., CFD Modelling and Calculation of Dynamic Two-Phase Flow in Columns Equipped with Structured Packing. *Chemical Engineering Research and Design* **2007,** 85, (8), 1112-1122.
34. Mahr, B.; Mewes, D., Two-phase flow in structured packings: Modeling and calculation on a macroscopic scale. *AIChE Journal* **2008,** 54, (3), 614-626.

35. Ferrua, M. J.; Singh, R. P., A nonintrusive flow measurement technique to validate the simulated laminar fluid flow in a packed container with vented walls. *International Journal of Refrigeration* **2008,** 31, 242-255.
36. Jafari, A.; Zamankhan, P.; Mousavi, S. M.; Pietarinen, K., Modeling and CFD simulation of flow behavior and dispersivity through randomly packed bed reactors. *Chemical Engineering Journal* **2008,** 144, 476-482.
37. Bai, H.; Theuerkauf, J.; Gillis, P. A., A Coulped DEM and CFD Simulation of Flow Field and Pressure Drop in Fixed Bed Reactor with Randomly Packed Catalyst Particles. *Industrial and Engineering Chemistry Research* **2009,** 48, 4060-74.
38. Fernandes, J.; Simoes, P. C.; Mota, J. P. B.; Saatdjian, E., Application of CFD in the study of supercritical fluid extraction with structured packing: Dry pressure drop... *The Journal of Supercritical Fluids* **2008,** 47, (1), 17-24.
39. Fernandes, J.; Lisboa, P. F.; Simoes, P. C.; Mota, J. P. B.; Saatdjian, E., Application of CFD in the study of supercritical fluid extraction with structured packing: Wet pressure drop calculations. *The Journal of Supercritical Fluids* **2009,** 50, 61-68.
40. Green, C. W. Hydraulic Characterization of Structured Packing via X-Ray Computed Tomography. The University of Texas, Austin, 2006.

# Vita

Scott Allen Owens was born in Oak Ridge, TN to Compton Cleophaus and Virgina Gail Owens. He grew up in the hills of east Tennessee and graduated from Karns High School. He graduated Summa Cum Laude from The University of Tennessee with a B.S. in Chemical Engineering; Honors Concentration and a Minor in Chemistry in May 2006. He worked for Sea Ray Boats, The Dow Chemical Company, and The University during his tenure. He began graduate school at The University of Texas at Austin; earning a Master's of Science in Engineering in 2008. He has accepted full-time employment with The Eastman Chemical Company.

Permanent or email: ScottAllenOwens@gmail.com

This dissertation was typed by Scott Allen Owens.